

The Experimental Characterization  
of an Electron Optical Lens

Mark M. Meininger

A thesis submitted to the faculty  
of the Oregon Graduate Center  
in partial fulfillment of the  
requirements for the degree  
Master of Science  
in  
Applied Physics

May 14, 1985

The thesis "The Experimental Characterization of an Electron Optical Lens" by Mark M. Meininger has been examined and approved by the following Examination Committee:

---

Jon H. Orloff  
Professor  
Thesis Research Advisor

---

Russell Kremer  
Assistant Professor

---

Gertrude F. Rempfer  
Professor, Portland State University

---

Hirschel Snodgrass  
Visiting Associate Professor,  
Reed College

## Acknowledgments

I would like to thank my thesis advisor, Dr. Jon H. Orloff, for giving me the benefit of his knowledge and experience in the field of electron optics, and for patiently accepting the detours and wrong turns inherent in experimental work. I would also like to thank Dr. Jean Delord of Reed College who, as my thesis advisor from Reed College, helped me through my early days at OGC. I owe a great deal of gratitude and respect to Dr. Gertrude Rempfer of Portland State University for sharing her expertise and time in the final days of this project.

Kevin McKinstry and Stuart Palmiter were two invaluable resources for help with the technical problems and the technical drudgery along the way. Nancy Christie would always have a new joke when I needed one. Finally, I would like to express my gratitude to my family for their support and love, especially to Jane, who was always there.

## Table of Contents

	Page
Acknowledgments	iii
List of Tables	v
List of Figures	vi
Abstract	x
Chapter	
I. Introduction	1
II. Theoretical Basis for the Experimental Technique	20
III. Experimental Arrangement	36
IV. Results	46
V. Conclusions	75
Appendix	
A. Electron Emission	77
B. Vacuum Technology	90
Bibliography	104
Vita	106

## List of Tables

Table		Page
1-1	Primary Lens Aberrations	18
4-1	Paraxial Grid Magnifications and Magnification Distortion Coefficients	53
4-2	Spherical Aberration Results for the Modulator Lens	54
4-3	Results of the Beam Cut-off Experiments	57
4-4	Shadow Measurement Data	71
4-5	Summary of Spherical Aberration Results	72
B-1	The Theoretical Time to Reach an Outgassing Rate of $10^{-13}$ W/m <sup>2</sup> in Stainless Steel	92
B-2	Approximate Relative Sensitivity of Bayard-Alpert Gauge Tubes to Different Gases	95
B-3	Basic Notes on the Operation Four Vacuum Pumps	96
B-4	Initial Sticking Coefficient and Quantity Sorbed for Various Gases on Titanium	98
B-5	Pumping Speeds of Ion Pumps Relative to Nitrogen	101

## List of Figures

Figure		Page
1-1	Cardinal Points	9
1-2	Spherical Aberration	13
1-3	Coma	14
1-4	Astigmatism	15
1-5	Curvature of Field	16
1-6	Distortion	17
2-1	Beam Modulator Lens	20
2-2	Simpson's Filter Lens	21
2-3	Spangenberg's and Field's Experimental Technique	23
2-4	Calculation of the Distance between the Fluorescent Screen and the Image Plane	27
2-5	Cross-Over Method	28
2-6	Basic Optical Relations	30
2-7	Nomenclature for the Calculation of the Spherical Aberration	31
3-1	Experimental Arrangement	38

Figure	Page
3-2 Diagram of the Electronics Used for I-V Plot of Beam Current Versus Faraday Cup Current	43
4-1 Grid Arrangements on the Modulator Lens	46
4-2 Screen Image Sample	47
4-3(a) Shadow Radii versus Grid Radii for Photographs 11I and 15I	48
4-3(b) Shadow Radii versus Grid Radii for Photographs 16I and 17I	49
4-3(c) Front Grid Magnifications versus Grid Radii Squared	51
4-3(d) Rear Grid Magnifications versus Grid Radii Squared	52
4-4 Faraday Cup Current versus Central Electrode Voltage $V_{\text{emitter}} = 1400$ volts, $V_{\text{focus}} = 1300, 1320$ volts	60
4-5 Faraday Cup Current versus Central Electrode Voltage $V_{\text{emitter}} = 1400$ volts, $V_{\text{focus}} = 1350, 1330$ volts	61
4-6 Faraday Cup Current versus Central Electrode Voltage $V_{\text{emitter}} = 1600$ volts, $V_{\text{focus}} = 1500, 1530$ volts	62
4-7 Faraday Cup Current versus Central Electrode Voltage $V_{\text{emitter}} = 1600$ volts, $V_{\text{focus}} = 1560$ volts	63
4-8 Faraday Cup Current versus Central Electrode Voltage $V_{\text{emitter}} = 1600$ volts, $V_{\text{focus}} = 1500, 1510, 1520$ volts	64
4-9 Faraday Cup Current versus Central Electrode Voltage $V_{\text{emitter}} = 1600$ volts, $V_{\text{focus}} = 1530, 1540$ volts	65

Figure	Page
4-10 Faraday Cup Current versus Central Electrode Voltage $V_{\text{emitter}} = 1600$ volts, $V_{\text{focus}} = 1520, 1500$ volts	66
4-11 Faraday Cup Current versus Central Electrode Voltage $V_{\text{emitter}} = 1600$ volts, $V_{\text{focus}} = 1560, 1540$ volts	67
4-12 Blanked Voltage versus Focus Voltage $V_{\text{emitter}} = 1400$ volts, Aperture Diameter = $1000\mu\text{m}$	68
4-13 Blanked Voltage versus Focus Voltage $V_{\text{emitter}} = 1600$ volts, Aperture Diameter = $1000\mu\text{m}$	68
4-14 Blanked Voltage versus Focus Voltage $V_{\text{emitter}} = 1600$ volts, Aperture Diameter = $150\mu\text{m}$	69
4-15 Maximum Current versus Focus Voltage $V_{\text{emitter}} = 1400$ volts, Aperture Diameter = $1000\mu\text{m}$	69
4-16 Maximum Current versus Focus Voltage $V_{\text{emitter}} = 1600$ volts, Aperture Diameter = $1000\mu\text{m}$	70
4-17 Maximum Current versus Focus Voltage $V_{\text{emitter}} = 1600$ volts, Aperture Diameter = $150\mu\text{m}$	70
4-18 Data Enlargements of Photographs 11I and 15I	73
4-19 Data Enlargements of Photographs 16I and 17I	74
A-1 Thermionic Emission and Photoemission	78

Figure		Page
A-2	Energy Diagrams of Insulators, Conductors, and Semiconductors	81
A-3	Surface Potential Barrier in Presence of Electric Field	83
A-4	Field Emission Energy Diagram	85
A-5	Theoretical Normal Energy Distribution of Field Emitted Electrons	87
B-1	Pumping Times for Systems of One or Two Sorption Pumps	97
B-2	Schematic Diagram of a Penning Cell	100
B-3	Schematic Diagrams of Diode and Triode Ion Pumps	101

## Abstract

Filter lenses have long been available which are able to resolve beam energies down to tenths of a volt. However, these lenses suffered a high degree of spherical aberration. A modulator lens was designed to reduce the spherical aberration without sacrificing the resolution of the filter lens.

Since preliminary computer calculations were unable to adequately determine the spherical aberration of the modulator lens, an experimental evaluation of this characteristic was undertaken. The technique used was based on the arrangement suggested by Spangenberg and Field in which grids placed before and after the lens are imaged onto a fluorescent screen. The resulting images are then used to measure the spherical aberration.

Although the resolution of the modulator lens was expected to be lower than that for a traditional filter lens, there was an intended lower limit of this resolution. The second phase in the characterization of the modulator lens was therefore to measure the energy resolution of the lens to determine whether or not it satisfied these predetermined conditions.

## Chapter I

### Introduction

A perusal of a portion of the literature<sup>1,2,3</sup> on electron optics shows that the terminology and concepts in the field are very similar to those in light optics. The duality of light and matter aside, one would expect the mechanisms and forces in light optics to be quite different from those in charged particle optics. For instance, light optics is based on the fact that light travels at different velocities in different materials, and it is through this property that lenses and mirrors interact with light. Electron optics on the other hand is driven by electric and magnetic fields which interact in vastly different ways, both from each other and from the way light interacts with transparent media. In order to utilize the tools of light optics in discussions of electron optics, it is necessary to prove the equivalence of the two fields. The derivations which follow will justify, through quantum mechanical and electrodynamical arguments, this equivalence.

The first consideration will be from a quantum mechanical point of view. Schrodinger's equation<sup>4</sup> for a particle in a potential  $V(r)$  is

$$[-\hbar^2/2m \nabla^2 + V(r)] \psi(r,t) = i\hbar \partial/\partial t \psi(r,t). \quad (1-1)$$

Consider a wave function solution of the form

$$\Psi(\mathbf{r},t) = A(\mathbf{r},t) \exp[i/\hbar S(\mathbf{r},t)], \quad (1-2)$$

where  $A(\mathbf{r},t)$  and  $S(\mathbf{r},t)$  are real functions. Substituting this expression into Schrodinger's equation and separating the real and imaginary parts one obtains

$$\partial S/\partial t + (\nabla S)^2/2m + V = \hbar^2/2m \nabla^2 A/A \quad (1-3)$$

$$m \partial A/\partial t + (\nabla A \cdot \nabla S) + A/2 \nabla^2 S = 0. \quad (1-4)$$

Multiplying equation (1-4) by  $2A$  and simplifying gives

$$\partial A^2/\partial t + \nabla \cdot (A^2 \nabla S)/m = 0, \quad (1-5)$$

which is simply the continuity equation in which the probability density is given by  $A^2$ , the mass density  $\rho$  by  $A^2 m$ , and the current density  $\mathbf{J}$  by  $A^2 \text{grad} S$ . The velocity may be written

$$\mathbf{v} = \mathbf{J}/\rho = A^2 \nabla S / A^2 m = \nabla S / m, \quad (1-6)$$

which shows that the trajectories of a set of electrons are normal to the surfaces of constant phase  $S$ . In terms of light optics these constant surfaces would be called wave fronts and the trajectories would be called the light rays.

The quantum mechanical derivation may be taken a step further if the wave function  $\Psi$  is taken to be a stationary state of energy  $E$ , in which case

$$\partial S/\partial t = -E \quad \partial A/\partial t = 0, \quad (1-7)$$

which reduces equations (1-3) and (1-4) respectively to

$$(\nabla S)^2 - 2m(E-V) = \hbar^2 \nabla^2 A/A \quad (1-8)$$

$$\nabla \cdot (A^2 \nabla S) = 0. \quad (1-9)$$

Taking the reduced wavelength to be given by

$$\lambda = \hbar/[2m(E-V)]^{1/2}, \quad (1-10)$$

and substituting into equation (1-8) one obtains

$$(\nabla S)^2 = \hbar^2/\lambda^2 (1 + \lambda^2 \nabla^2 A/A), \quad (1-11)$$

which in the short wavelength approximation is reduced to

$$(\nabla S)^2 = \hbar^2/\lambda^2. \quad (1-12)$$

Equation (1-12) is the electron optical equivalent of the eikonal equation for a geometrical wave front in light optics.<sup>5</sup>

It should now be clear that the quantum mechanical consideration of an electron in a potential results in several theoretical relations which are similar to those in light optics. The next step will be to show that electron optics may in fact be considered a subset of the electrodynamical development of light optics.

Any electrodynamical derivation must begin with Maxwell's equations<sup>6</sup>

$$\nabla \cdot \mathbf{D} = 4\pi\rho \quad (1-13)$$

$$\nabla \cdot \mathbf{B} = 0 \quad (1-14)$$

$$\nabla \times \mathbf{E} = -1/c \partial \mathbf{B} / \partial t \quad (1-15)$$

$$\nabla \times \mathbf{H} = 4\pi/c \mathbf{J} + 1/c \partial \mathbf{D} / \partial t \quad (1-16)$$

which are here given in gaussian units. Consider the harmonic solution to Maxwell's equations

$$\mathbf{E} = \mathbf{E}'(\mathbf{r}) e^{-i\omega t} \quad \mathbf{H} = \mathbf{H}'(\mathbf{r}) e^{-i\omega t}, \quad (1-17)$$

with fields of the form

$$\mathbf{E}'(\mathbf{r}) = \mathbf{e}(\mathbf{r}) e^{ikL(\mathbf{r})} \quad (1-18)$$

$$\mathbf{H}'(\mathbf{r}) = \mathbf{h}(\mathbf{r}) e^{ikL(\mathbf{r})} \quad (1-19)$$

These expressions, taken with the vector identity

$$\nabla \times (\mu \mathbf{A}) = \nabla \mu \times \mathbf{A} + \mu (\nabla \times \mathbf{A}) \quad (1-20)$$

and the assumption that the current and charge densities are zero, reduce Maxwell's equations to

$$\mathbf{e} \cdot \nabla L = -1/ik [\mathbf{e} \cdot \nabla(\log \epsilon) + \nabla \cdot \mathbf{e}] \quad (1-21)$$

$$\mathbf{h} \cdot \nabla L = -1/ik [\mathbf{h} \cdot \nabla(\log \mu) + \nabla \cdot \mathbf{h}] \quad (1-22)$$

$$\nabla L \times \mathbf{e} - \mu \mathbf{h} = -1/ik \nabla \times \mathbf{e} \quad (1-23)$$

$$\nabla L \times \mathbf{h} + \epsilon \mathbf{e} = -1/ik \nabla \times \mathbf{h}. \quad (1-24)$$

Studying the electron optical case one needs only to consider wavelengths which are very short. Since  $k = \omega/c = 2\pi/\lambda c$ , it is obvious that  $k \rightarrow \infty$  as  $\lambda \rightarrow 0$ . Therefore in the limit  $\lambda$  approaches zero,  $1/ik$  also approaches zero and terms containing this factor can be ignored. The simplified results from equations (1-21) - (1-24) are

$$\mathbf{e} \cdot \nabla L = 0 \quad (1-25)$$

$$\mathbf{h} \cdot \nabla L = 0 \quad (1-26)$$

$$\nabla L \times \mathbf{e} - \mu \mathbf{h} = 0 \quad (1-27)$$

$$\nabla L \times \mathbf{h} + \epsilon \mathbf{e} = 0. \quad (1-28)$$

To solve this set of equations one first notices that equations (1-25) and (1-26) are the dot product of  $\nabla L$  with equations (1-27) and (1-28)

respectively. Therefore one needs only to solve one pair of the equations.

Rewriting equation (1-27)

$$\mathbf{h} = 1/\mu \nabla L \times \mathbf{e}, \quad (1-29)$$

and substituting into equation (1-28) gives

$$\nabla L \times (1/\mu \nabla L \times \mathbf{e}) + \epsilon \mathbf{e} = 0. \quad (1-30)$$

By the bac-cab vector identity, equation (1-30) becomes

$$1/\mu [\nabla L (\nabla L \cdot \mathbf{e}) - \mathbf{e} (\nabla L \cdot \nabla L)] + \epsilon \mathbf{e} = 0 \quad (1-31)$$

which, by referring back to equation (1-25) finally gives

$$(\nabla L)^2 = \mu \epsilon. \quad (1-32)$$

The term  $(\mu \epsilon)^{1/2}$  is defined to be the light optical index of refraction. This result, in the short wavelength electron optical limit, is equivalent to the light optical eikonal equation<sup>7</sup> which relates the optical path (L) of a light wave to the index of refraction.

It has thus been shown, through quantum mechanical and electro-dynamical arguments, that electron optics is formally similar to light optics. The electro-dynamical derivations even show that electron optics may be considered a subset of light optics. Therefore, the applicability of optical terminology to electron optics is adequately justified.

A lens is defined by a set of values called cardinal points<sup>8</sup>. The following derivations of the cardinal points are taken from Born and Wolf (reference 5), and will make use of projective transformations. Such transformations project lines in the object space into lines in the image space, and to first order can describe any optical system.

Let a point P in the object space with coordinates (x,y,z) correspond

to a point  $P'$  in the image space with coordinates  $(x',y',z')$  through a projective transformation. Let that transformation be expressed as

$$x' = F_1/F_0 \quad (1-33a)$$

$$y' = F_2/F_0 \quad (1-33b)$$

$$z' = F_3/F_0 \quad (1-33c)$$

where

$$F_i = a_i x + b_i y + c_i z + d_i \quad (i = 0,1,2,3). \quad (1-34)$$

One can also solve for  $x$ ,  $y$ , and  $z$  to obtain the relations

$$x = F'_1/F'_0 \quad (1-35a)$$

$$y = F'_2/F'_0 \quad (1-35b)$$

$$z = F'_3/F'_0 \quad (1-35c)$$

$$F'_i = a'_i x' + b'_i y' + c'_i z' + d'_i \quad (i = 0,1,2,3). \quad (1-36)$$

For simplicity consider only cases which are axially symmetric. It follows that the image of any point  $P_0$  lies in the plane defined by  $P_0$  and the lens axis. Consider an object point on the  $y$ -axis so that the image point lies in the  $y$ - $z$  plane (the  $z$ -axis taken to be the axis of symmetry of the lens). The projective transformation then transforms the object point  $(0,y,z)$  to the image point  $(0,y',z')$ . Hence

$$y' = [F_2/F_0]_{x=0} \quad (1-37a)$$

$$z' = [F_3/F_0]_{x=0} \quad (1-37b)$$

may be written

$$y' = [b_2y + c_2z + d_2]/[b_0y + c_0x + d_0] \quad (1-38a)$$

$$z' = [b_3y + c_3z + d_3]/[b_0y + c_0z + d_0]. \quad (1-38b)$$

Due to the stipulation of axial symmetry it follows that changing  $y$  to  $-y$  should also change  $y'$  to  $-y'$ , but that  $z'$  should be unaffected. The second of these results holds true if  $b_3 = b_0 = 0$ , which eliminates the  $y$ -dependence of  $z'$ . The first is satisfied when  $c_2 = d_2 = 0$  which, along with the previous condition, gives  $y'$  a direct dependence on  $y$ . Equations (1-39a) and (1-39b) are then reduced to

$$y' = b_2y/(c_0z + d_0) \quad (1-39a)$$

$$z' = [c_3x + d_3]/[c_0z + d_0]. \quad (1-39b)$$

Solving for  $y$  and  $z$  gives

$$y = y'(c_0z + d_0)/b_2 \quad (1-40a)$$

$$z = [d_3 - d_0z']/[c_0z' - c_3]. \quad (1-40b)$$

which by substituting  $z$  into equation (1-40a) gives

$$y = (y'/b_2) [c_0d_3 - c_3d_0]/[c_0z' - c_3]. \quad (1-41)$$

The focal planes are defined to be

$$F_0 \equiv c_0z + d_0 = 0 \quad (1-42a)$$

$$F'_0 \equiv c_0z' - c_3 = 0. \quad (1-42b)$$

Hence the focal planes intersect the lens ( $z$ ) axis at the points

$$z = -d_0/c_0 \quad (1-43a)$$

$$z' = c_3/c_0. \quad (1-43b)$$

The two points (1-43a) and (1-43b) are taken to be the focal points<sup>9</sup> of the lens, and are the first two of the six cardinal points which define a lens.

One may simplify the derivation of several important optical relations by changing the coordinate system so that the  $z$  and  $z'$  coordinates are measured from their respective focal points. This results in the coordinate transformation

$$y = Y \quad (1-44a)$$

$$c_0 z + d_0 = c_0 Z \quad (1-44b)$$

$$y' = Y' \quad (1-44c)$$

$$c_0 z' - c_3 = c_0 Z' \quad (1-44d)$$

If one now substitutes these new coordinates into equations (1-39) one obtains

$$Y' = (b_2 Y)/(c_0 Z) \quad (1-45a)$$

$$Z' = (c_0 d_3 - c_3 d_0)/(c_0^2 Z) \quad (1-45b)$$

which, with the substitutions

$$f = b_2/c_0 \quad (1-46a)$$

$$f' = (c_0 d_3 - c_3 d_0)/(c_0 b_2) \quad (1-46b)$$

give

$$Y'/Y = f/Z = Z'/f'. \quad (1-47)$$

This relation is Newton's equation which is normally written in the form<sup>10</sup>

$$ZZ' = ff' \quad (1-48)$$

where  $f$  is the focal length of the object space and  $f'$  is the focal length of the image space. The lateral magnification can now be calculated as the derivative of equation (1-47)<sup>11</sup>

$$\left(\frac{dY}{dY'}\right)_Z = b_2 Y/Z = Y'/Y. \quad (1-49)$$

Similarly the derivative of (1-46b) shows the longitudinal magnification to be

$$dZ'/dZ = -(c_0 d_3 - c_3 d_0)/(c_0^2 Z^2) = -Z'/Z. \quad (1-50)$$

The lateral and longitudinal magnifications are then related as

$$dZ'/dZ = -f'/f \left(\frac{dY'}{dY}\right)_Z^2. \quad (1-51)$$

From (1-49) it is clear that the lateral magnification is unitary when  $Z = f$  and  $Z' = f'$ . The planes which satisfy the condition of unitary lateral

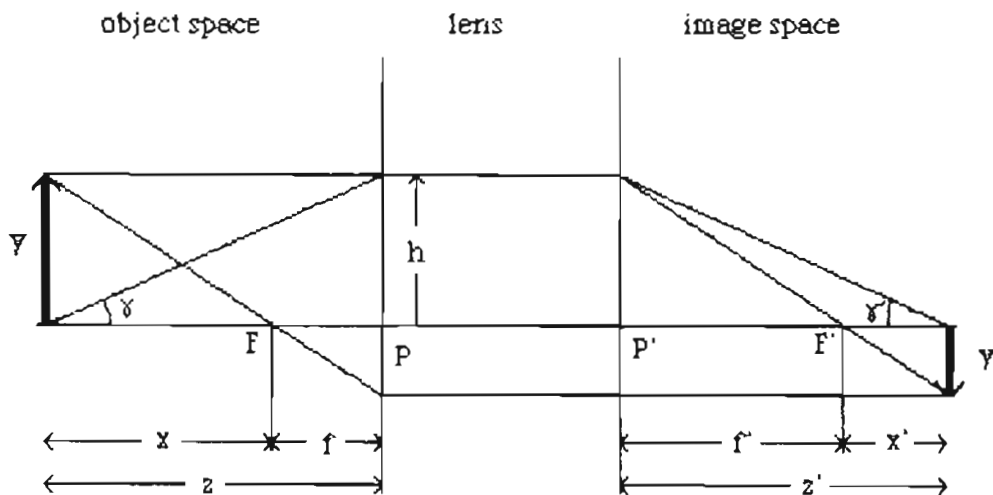


Figure 1-1. Cardinal Points

magnification are called the principle planes, and the points where those planes intersect the lens axis are called the principle points<sup>12</sup> P and P'. The principle points are where lateral magnification equals one (see figure 1-1).

To derive the final pair of cardinal points, let a ray leaving the axis in the object space at an angle  $\gamma$  intersect the principle plane of the object space at a height  $h$ . This ray is imaged into the principle plane of the image space at unit magnification, and then intersects the axis again at an angle  $\gamma'$  in the image space. From figure (1-1) it is clear that  $\tan\gamma = h/(f-x)$  ( $x$  measured in the negative direction) and  $\tan\gamma' = h/(x'-f')$  ( $\gamma'$  a negative angle) The angular magnification<sup>13</sup> is then taken to be the ratio of these terms

$$\tan\gamma'/\tan\gamma = (f-x)/(x'-f') \quad (1-52)$$

which multiplying top and bottom by  $Z$ , and then substituting  $ff'$  for  $xx'$  gives

$$x/f' = f/x' \quad (1-53)$$

When  $x=f'$  and  $f=x'$ , the ratios are unitary, and the two points which satisfy these conditions are the final cardinal points called the nodal points.<sup>14</sup> The nodal points are the two points characterized by the property that conjugate rays (rays which pass from the object/image tip to the corresponding principle plane) which pass through them are parallel to each other.

Now that the cardinal properties of lenses have been defined, it is important to realize that the above idealized lens does not exist, especially

in electron optics. Every real lens has a variety of imperfections called aberrations. To truly define a lens it is necessary to know not only the cardinal points, but also the relative value of each aberration.

Aberration theory uses the Seidel coefficients to describe the relative amounts of the different aberrations present in a lens. The theory in this instance is taken directly from the light optical theory as described by Born and Wolf.

The Seidel coefficients can be derived from the equations<sup>15</sup>

$$\begin{aligned} \Delta x' &= x_0(2C\kappa^2 - E r^2 - F\rho^2) \\ &+ \zeta_1(B\rho^2 + D r^2 - 2F\kappa^2) \end{aligned} \quad (1-54)$$

$$\begin{aligned} \Delta y' &= y_0(2C\kappa^2 - E r^2 - F\rho^2) \\ &+ \eta_1(B\rho^2 + D r^2 - 2F\kappa^2) \end{aligned} \quad (1-55)$$

with the variables given by

$$r^2 = x_0^2 + y_0^2 \quad (1-56)$$

$$\kappa^2 = x_0\zeta_1 + y_0\eta_1 \quad (1-57)$$

$$\zeta_1 = \rho\sin\theta \quad (1-58)$$

$$\eta_1 = \rho\cos\theta. \quad (1-59)$$

Substituting these expressions into equations (1-54) and (1-55) one obtains

$$\begin{aligned} \Delta x' &= B\rho^3\sin\theta - F\rho^2(2x\sin^2\theta + 2y\cos\theta\sin\theta - x) \\ &+ 2C\rho x(x\sin\theta + y\cos\theta) + D\rho\sin\theta(x^2 + y^2) \\ &- E x(x^2 + y^2) \end{aligned} \quad (1-60)$$

$$\begin{aligned} \Delta y' = & B\rho^3 \cos\theta - F\rho^2(2y \cos^2\theta + 2x \cos\theta \sin\theta - x) \\ & + 2C\rho y(x \sin\theta + y \cos\theta) + D\rho \cos\theta(x^2 + y^2) \\ & - Ey(x^2 + y^2). \end{aligned} \quad (1-61)$$

Within this format the Seidel coefficients are represented by the variables B,C,D,E and F.

Even in the "clarified" form of equations (1-60) and (1-61), the mathematical and conceptual meanings of the Seidel coefficients are very complicated. Therefore, to best describe and explain these coefficients each one will be considered individually with all other coefficients set to zero during that explanation.

## B: SPHERICAL ABERRATION

$$\Delta x' = B\rho^3 \sin\theta \quad (1-62)$$

$$\Delta y' = B\rho^3 \cos\theta \quad (1-63)$$

Consider a pencil of electrons (that is to say a bundle of electron rays) emerging from a point on the axis of the object plane  $z_0$ . The electrons which leave at very small angles to the axis (paraxial rays) intercept the axis further away from the object plane than those which emerge with larger angles (called zonal rays). The aberration curves are therefore concentric circles whose centers are on axis, but whose radii increase as the cube of the zonal radius as stated in equations (1-62) and (1-63).

This aberration is clearly minimized, that is to say the spot size is minimized, at some point along the axis. This minimum beam diameter is called the "circle of least confusion"<sup>16</sup>.

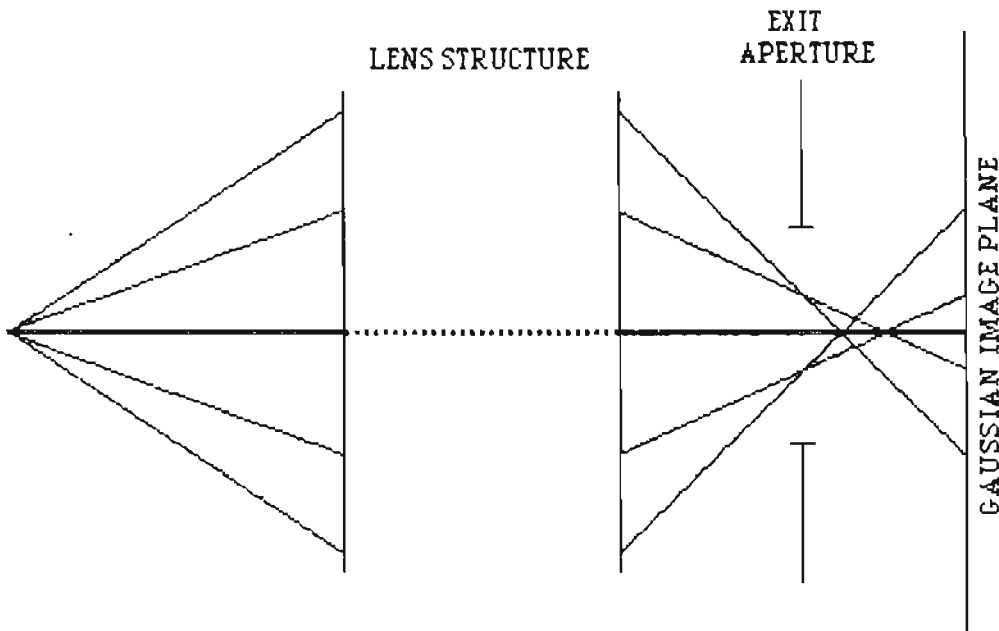


Figure 1-2. Spherical Aberration

#### F: COMA

Coma aberration terms can be written

$$\Delta x' = -F_p^2(2x \sin^2 \theta + 2y \cos \theta \sin \theta - x) \quad (1-64)$$

$$\Delta y' = -F_p^2(2y \cos^2 \theta + 2x \cos \theta \sin \theta + y) \quad (1-65)$$

which in the simplified case of  $x=0$  reduce to

$$\Delta x' = -2F_p^2 \cos \theta \sin \theta = -F_p^2 \sin 2\theta \quad (1-66)$$

$$\Delta y' = -F_p^2(2 \cos^2 \theta + 1) = -F_p^2(\cos 2\theta + 2). \quad (1-67)$$

Consider points off the axis from which parallel rays begin (see figure 1-3). Coma causes an asymmetrical deformation of the image points resulting in a comet-like appearance. If the lens were perfect, all the beams would be focused to the point A.

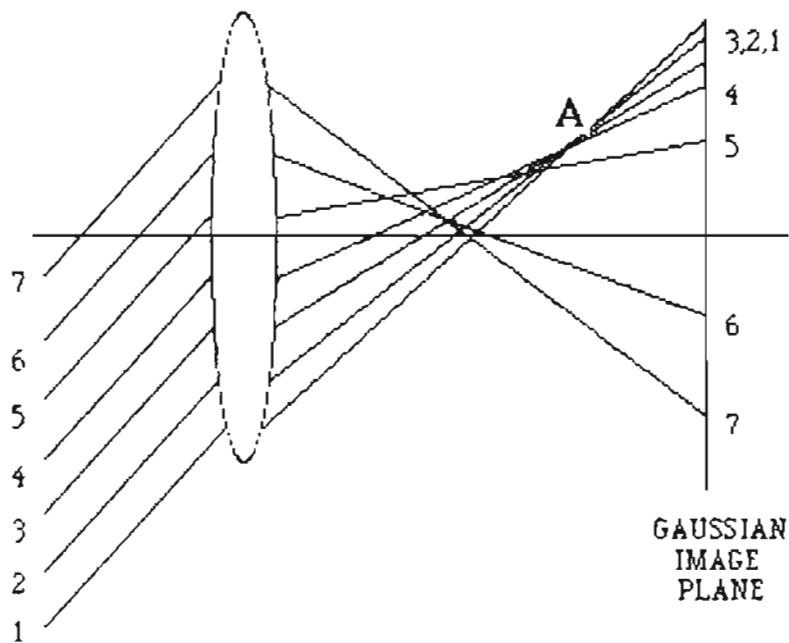


Figure 1-3. Coma

Coma causes rays with small angles of incidence (rays 1,2,3) with the lens to be focused close to A, while those rays with larger angles of incidence (rays 4,5,6) will be focused elsewhere.

### C: ASTIGMATISM

The aberration components for astigmatism are

$$\Delta x' = 2C_{\rho x}(x \sin \theta + y \cos \theta) \quad (1-68)$$

$$\Delta y' = 2C_{\rho y}(x \sin \theta + y \cos \theta). \quad (1-69)$$

Once again considering the special case of  $x = 0$ , equation (1-68) reduces to zero and equation (1-69) reduces to

$$\Delta y' = 2C_{\rho} y^2 \cos \Theta. \quad (1-70)$$

This may be best understood by consideration of the following figure. Here the central ray intersects the  $z$ -axis at  $O$ , and the sagittal and tangential rays behave as shown. The point (circle) in the object plane is imaged into an ovoid. From the  $x=0$  case of the aberration components it is clear that there is no  $x'$  deviation in the image, and that the  $y'$  deviation goes as

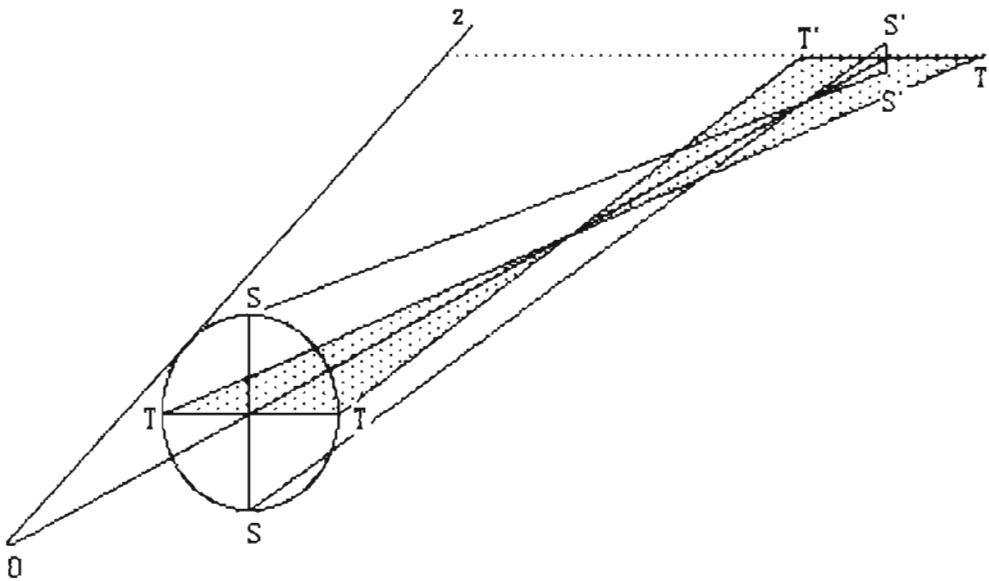


Figure 1-4. Astigmatism

the square of  $y$ . One can also see that with the different foci for the sagittal and tangential rays, the best image possible is again at a "circle of

least confusion".

#### D. CURVATURE OF FIELD

This aberration has the components

$$\Delta x' = Dp \sin \theta (x^2 + y^2) \quad (1-71)$$

$$\Delta y' = Dp \cos \theta (x^2 + y^2) \quad (1-72)$$

which at  $x=0$  reduce to

$$\Delta x' = Dp y^2 \sin \theta \quad (1-73)$$

$$\Delta y' = Dp y^2 \cos \theta. \quad (1-74)$$

These components are very similar to those describing astigmatism (see equation (1-70)). Curvature of field is the instance when the gaussian image plane becomes a curved surface. The image is focused onto a curved surface rather than a planar one (see figure).

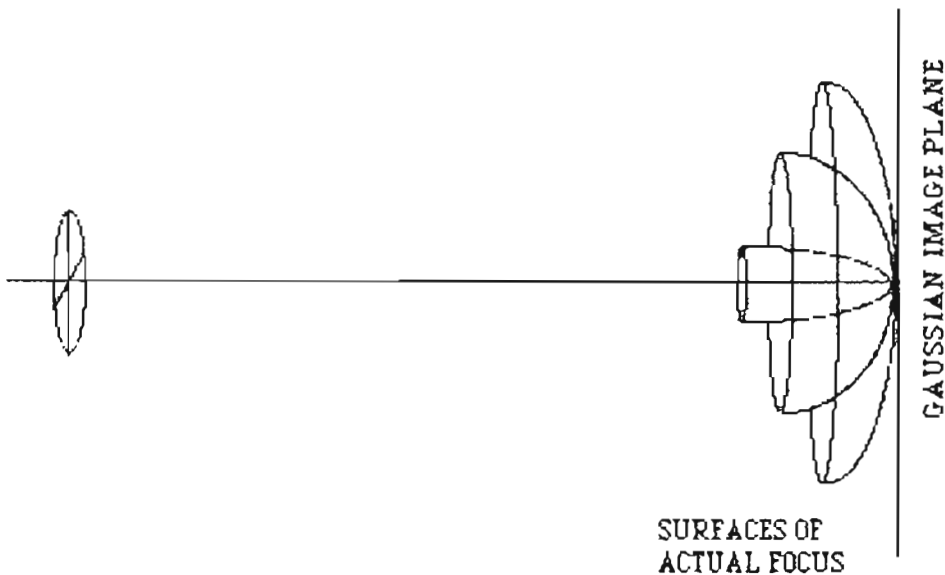


Figure 1-5. Curvature of Field

The primary wave aberrations for an electrostatic lens have been discussed. These characteristics are reviewed in the table below<sup>17</sup>.

Table 1-1

## PRIMARY LENS ABERRATIONS

COEFFICIENT	ERROR	CAUSE	EFFECT
<b>B</b>	spherical aberration	excessive or deficient refraction with increasing aperture	paraxial and zonal rays have different intersection on the axis
<b>F</b>	coma	aberration for slanting parallel rays	comet tails at image points
<b>C</b>	astigmatism	bundles of rays meet different curvatures of equipotentials	off axis image points are not imaged as points
<b>D</b>	curvature of field	same as astigmatism	image of plane object is curved
<b>E</b>	distortion	residual error of spherical aberration and position of aperture stop	straight lines are curved at the margin of image

### References

1. O. Klemperer and M.E. Barnett, Electron Optics, (Cambridge University Press, Cambridge, 1971)
2. P.W. Hawkes, Electron Optics and Electron Microscopy, (Taylor and Francis Ltd., London, 1972)
3. P. Grivet, Electron Optics, (Pergamon Press, New York, 1972)
4. Eugen Merzbacher, Quantum Mechanics, (John Wiley & Sons, New York, 1961) p.426
5. Max Born and Emil Wolf, Principles of Optics, (Pergamon Press, New York, 1959) p.112
6. J.D. Jackson, Classical Electrodynamics, (John Wiley & Sons, New York, 1975) p.217
7. Born and Wolf, p.111
8. Klemperer and Barnett, p.10
9. Born and Wolf, p.151
10. Ibid.
11. Ibid., p.152
12. Ibid.
13. Ibid.
14. Ibid.
15. Ibid., p.210
16. Ibid., p.212
17. Klemperer and Barnett, p.161

## Chapter II

### Theoretical Basis for the Experimental Technique

From the time in 1871 that C. F. Varley first deflected cathode rays with an electrostatic field<sup>1</sup>, electron lenses have taken on a myriad of shapes and designs. From the conceptual simplicity of parallel plate deflectors to the highly complicated "elkhorn" shaped beam spreaders found in modern oscilloscopes, it is evident that many electron optical devices have very little in common. There are however many electron lenses which consist of axially symmetric elements, as does the lens which is the basis for this thesis. It has five axially and longitudinally symmetric plates which are operated in an electrostatic mode. The longitudinal

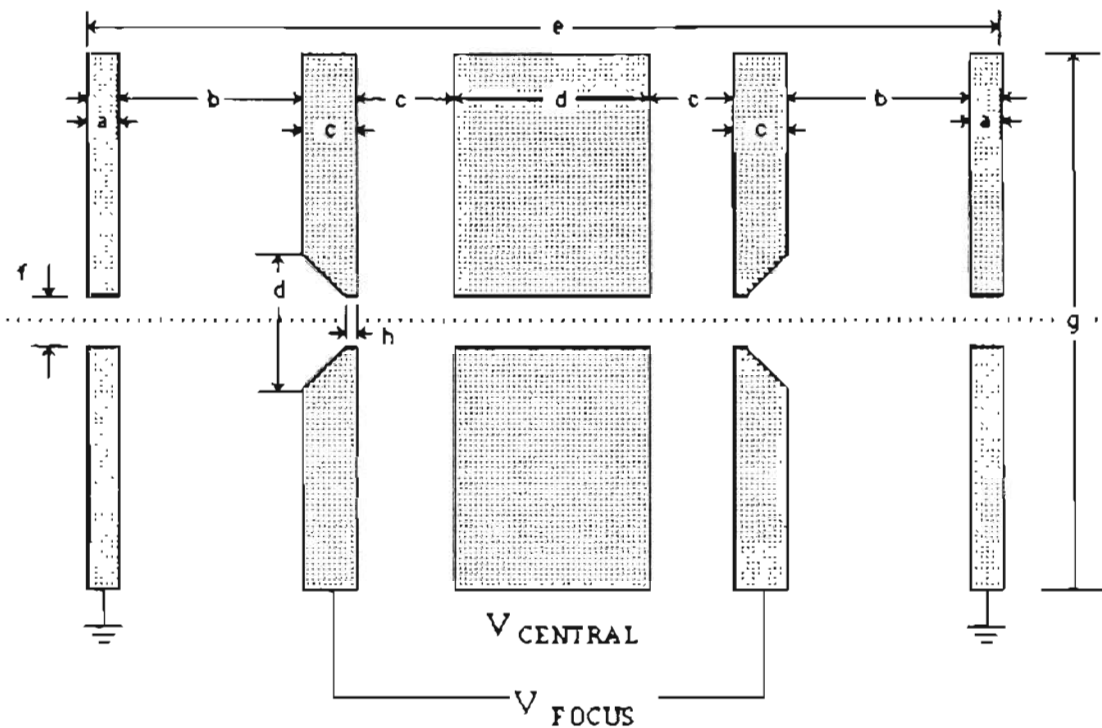


Figure 2-1. Beam Modulator Lens

symmetry is both physical and electrodynamical (see figure 2-1). This type of lens is called a beam modulation lens.

A lens which had the same general properties as the beam modulator was first utilized about thirty years ago in a three element form. That lens was used by Boersch<sup>2</sup> to filter out low energy electrons with modest energy resolution. Besides the mediocre energy resolution, the lens performance was also hampered by an inherently short focal length and a strong dependence of the focal length on the degree of filtering. A five element device later designed by Simpson alleviated these problems. This lens was

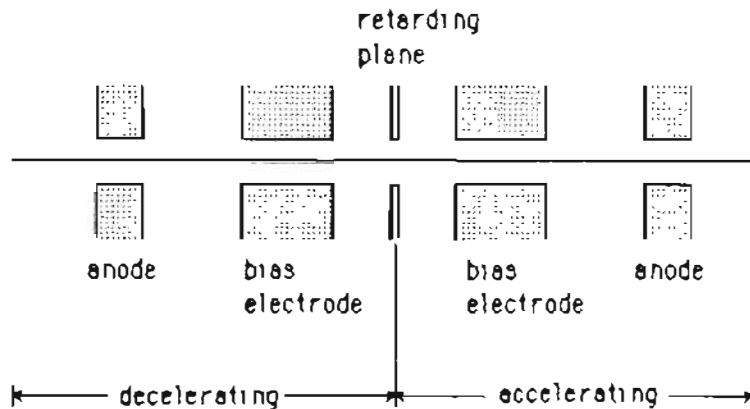


Figure 2-2. Simpson's Filter Lens

essentially two lenses in which the potentials in the object and image space of each are constant and unequal. The five element device is similar to two immersion lenses placed back-to-back in which the first lens retards the beam to a real image at the midplane, and the second accelerates it to

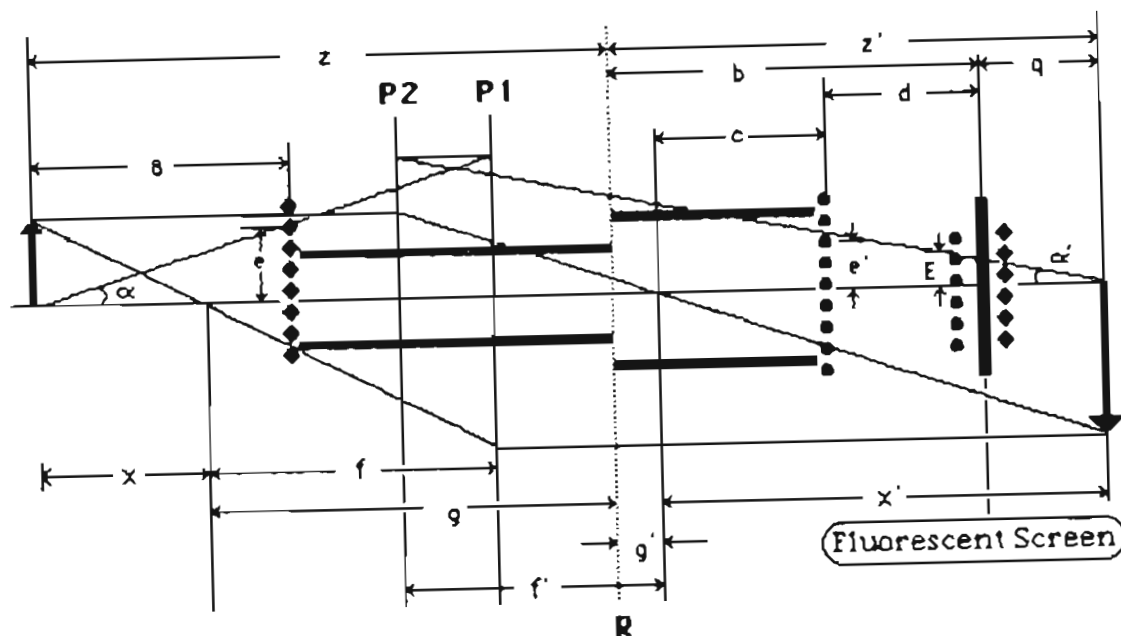
another plane (see figure 2-2).

Simpson's lens worked very well as an energy dependent beam filter. Laboratory results have shown that voltage changes as small as 0.10 volts on the central electrode can block an electron beam<sup>3</sup>. In fact, the cases in which this was measured were limited by the 0.10 volt resolution in the beam energy, so the actual resolution of the lens may be even higher. With such resolution capabilities the utility of this lens as a high-pass filter, energy analyzer, or high frequency beam modulator is quite evident.

Although Simpson's lens transmitted images better than the earlier three element device, it still had an annoyingly large spherical aberration. In an attempt to rectify this problem Dr. Jon Orloff modified Simpson's design so that the central electrode would be substantially thicker than any of the other electrodes (see figure 2-1). The computer simulations which were used in the design process showed that the modifications may have corrected the aberration problem, but the computed results were not conclusive. Therefore experimental means were used to test the lens to clarify the conclusions of the numerical calculations.

The properties to be evaluated were the cardinal lengths, the beam cut-off capabilities, and the spherical aberration of the lens. The basis for the technique used was a paper published by Spangenberg and Field in 1942 (reference 4), which reviewed numerical techniques for the calculation of electron paths, and gave an experimental method for the measurement of focal distances, spherical aberration, and minimum spot size. The essence of their method was to determine the magnifications of measuring grids placed before and after the lens. A grid of parallel wires was placed on the front part of the lens which cast a shadow on a

fluorescent screen following the lens. Another grid of parallel wires, perpendicular to the first, was placed at the rear of the lens in the same fashion. With this arrangement one could observe the magnifications of the two grids as the voltage ratio of the lens electrodes was varied. The experiment was then repeated with the electron source at a different distance from the lens. Thus two complete runs were made at each of two



P1 = first principal plane    P2 = second principal plane    R = reference plane

Figure 2-3. Spangenberg's and Field's Experimental Technique

distances. As will be shown below, this data enabled one to calculate four of the cardinal distances and the spherical aberration of a lens.

Spangenberg's and Field's derivation was used, with an alternate sign convention and added details. The basic point of the derivation was to show that object and image distances could be expressed in terms of lateral magnifications and focal distances, and hence that the spherical aberration could be determined. From figure 2-3 it is clear that

$$z = x + g \quad (2-1)$$

$$z' = x' + g', \quad (2-2)$$

which, taken with the basis for Newton's formula given by

$$m = f/x = x'/f' \quad (2-3)$$

could be reduced to

$$z = f/m + g \quad (2-4)$$

$$z' = f'm + g', \quad (2-5)$$

where the sign convention is that distances are measured positively to both the right and the left of the reference plane. The unknown variables in these two equations are  $f$ ,  $f'$ ,  $g$ , and  $g'$  implying that there are only two equations with four unknowns. To solve for these variables it is necessary to have two more equations, which one obtains from a second set of data at a different value of  $z$  for a given lens voltage ratio. This gives the equations

$$z_1 = f/m_1 + g \quad (2-6)$$

$$z'_1 = f'm_1 + g' \quad (2-7)$$

$$z_2 = f/m_2 + g \quad (2-8)$$

$$z'_2 = f'm_2 + g' \quad (2-9)$$

in which the  $z_i$ ,  $z'_i$ , and  $m_i$  are known. It is then straightforward to solve for the four cardinal lengths.

To solve for the focal length of the object space  $f$ , one first solves equations (2-6) and (2-8) for the object principle length  $g$ . This gives respectively

$$z_1 - f/m_1 = g \quad (2-10)$$

$$z_2 - f/m_2 = g. \quad (2-11)$$

Subtracting equation (2-11) from equation (2-10) gives

$$z_1 - f/m_1 - z_2 + f/m_2 = 0, \quad (2-12)$$

which, upon solving for  $f$  reduces to

$$f = (z_1 - z_2) / (1/m_1 - 1/m_2). \quad (2-13)$$

Although equation (2-13) is the negative of the equation reached by Spangenberg and Field, it follows from the alternate sign convention, and it agrees with their cited reference<sup>5</sup>.

The calculation for the focal length in the image space  $f'$  on the other hand gives the same result as that reached by Spangenberg and Field. Beginning as before, one solves equations (2-7) and (2-9) for the image principle length  $g'$

$$g' = z'_1 - m_1 f' \quad (2-14)$$

$$g' = z'_2 - m_2 f'. \quad (2-15)$$

Subtracting equation (2-15) from equation (2-14) gives

$$z'_1 - z'_2 + f'(m_2 - m_1) = 0. \quad (2-16)$$

Slight rearrangement gives the result

$$f' = (z'_2 - z'_1) / (m_2 - m_1). \quad (2-17)$$

The derivations of  $g$  and  $g'$  utilize the same techniques as are used in the derivations of  $f$  and  $f'$ . One solves the two equations for  $f$  (or  $f'$ ), subtracts them, and then rearranges them to solve for  $g$  (or  $g'$ ). The solutions, this time in agreement with Spangenberg and Field, are

$$g = (z_1 m_1 - z_2 m_2) / (m_1 - m_2) \quad (2-18)$$

$$g' = (z'_1/m_1 - z'_2/m_2) / (1/m_1 - 1/m_2). \quad (2-19)$$

To prove the applicability of this experimental technique, it remains to be shown that the lateral magnifications  $m_x$  could be determined from the data. The angular magnification  $m_\alpha$  is taken to be

$$m_\alpha = \tan \alpha' / \tan \alpha \approx \alpha' / \alpha, \quad (2-20)$$

where  $\alpha$  is the angle between the ray and the axis in the object space and  $\alpha'$  is the angle in the image space. Referring to figure 2-3, one sees that for a ray which passes through the front grid an arbitrary height  $E$  off of the axis, equation (2-20) may be written

$$m_\alpha = [E/q] / [e/a] \quad (2-21)$$

which reduces to

$$m_\alpha = aE/eq. \quad (2-22)$$

Using Lagrange's equation

$$Y'\alpha' = X\alpha \quad (2-23)$$

it is clear that the lateral and angular magnifications are related as

$$X/X' = \alpha'/\alpha \rightarrow m_x = 1/m_\alpha. \quad (2-24)$$

Thus the lateral magnification is given by

$$m_x = eq/aE. \quad (2-25)$$

From figure 2-3 one may note that  $q$ , the distance between the screen and the gaussian image plane, is the only pertinent variable which has not been derived. Although figure 2-3 shows the image plane beyond the fluorescent screen, it is possible that the image plane would be between the screen and the lens. Therefore the variable  $q$  could be related to the other lens dimensions in one of two ways. Figure 2-4 exemplifies the case when the image plane is behind the screen. By simple trigonometric argument

$$\tan \alpha' = E/q = e'/(d+q) \quad (2-26)$$

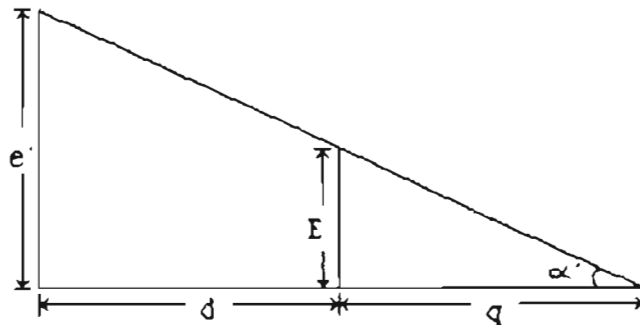


Figure 2-4. Calculation of the Distance between the Fluorescent Screen and the Image Plane

giving

$$Eq + Ed = qe', \quad (2-27)$$

which may be solved for  $q$  to obtain

$$q = d/(e'/E - 1). \quad (2-28)$$

The case of the image plane falling between the screen and the lens may be treated similarly to give

$$q = d/(e'/E + 1). \quad (2-29)$$

One must therefore determine from the photographic data the location of the gaussian image plane to calculate  $q$ , and subsequently to calculate the magnification and spherical aberration.

The justifications for the experimental derivation of the spherical aberration follow. The method suggested by Spangenberg and Field utilizes a graphical measurement. They recommended that a ray diagram be drawn which connected the image points to their corresponding object points (see figure 2-5). From this diagram it

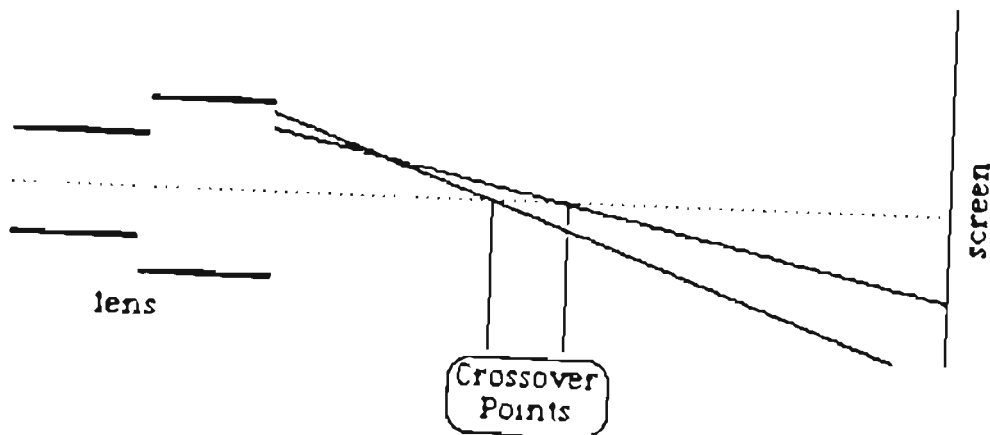


Figure 2-5. Cross-Over Method

would then be possible to plot the change in the location of the focal points versus the radial distance of the rays.

The calculation of the spherical aberration used for this project was based on a more thorough analysis of the phenomena as was discussed by Gertrude F. Rempfer<sup>6</sup>. The basis of her argument was that since the principal surfaces of a lens are in general not planar, the calculation of the spherical aberration must take into account the change in focal length as well as the change in the focal distance. The difference between the two is that the focal distance is measured from a fixed reference plane, while the focal length is measured relative to the principal surface.

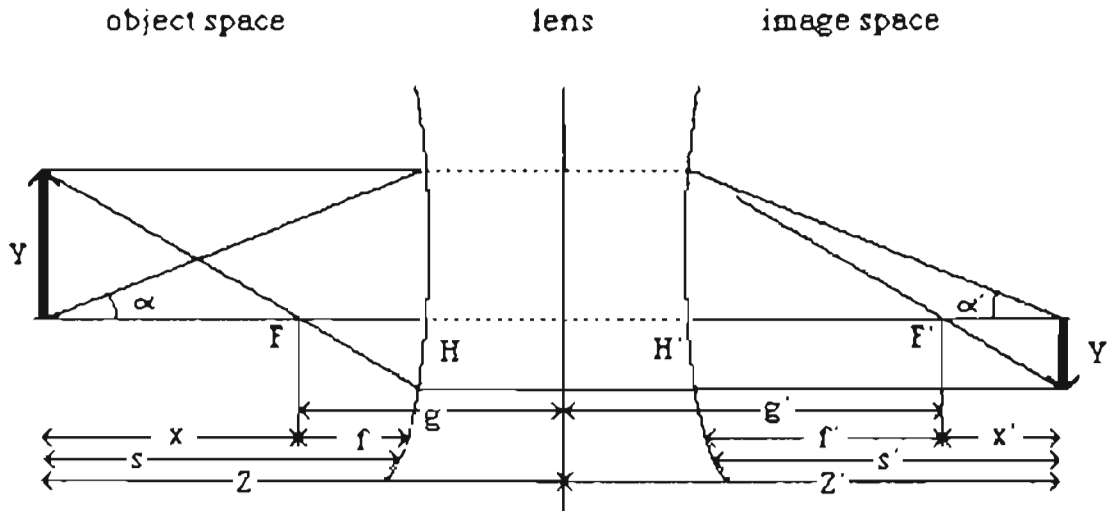
Figure 2-6 contains basic optical equations and distances as a compilation of previously covered material for reference purposes. Figure 2-7 on the following page contains the lens and beam information which is directly pertinent to the discussion of the spherical aberration calculation. The sign convention is the same as was earlier stated, that is, distances to both the right and left of the reference plane will be taken to be positive. Also, primed variables refer to image-side values, and variables with an "o" subscript refer to the paraxial value for that variable. In figure 2-7 a ray from a virtual point source at  $z$  passes through the lens, forms a demagnified image at  $z'$ , and then lands on a fluorescent screen which is  $(b+d)$  from the reference plane. The front grid is a distance  $(a)$  from the source while the rear grid is a distance  $(b)$  from the reference plane. The front and rear grid magnifications are respectively given by

$$M = E/e \quad (2-30)$$

$$M' = E/e' \quad (2-31)$$

By using small angle approximations of  $\tan \alpha'$  and  $\tan \alpha$ , the image distance  $z'$  may be written

$$z' = b - c = b - d/(M' - 1), \quad (2-32)$$



### Relations

$$xx' = ff' \quad (\text{Newtonian Lens}) \quad f'/f = (V'/V)^{1/2}$$

$$m = |Y'/Y| = x'/f' = f/x \quad (\text{Linear Magnification})$$

$$m_\alpha = \alpha'/\alpha = 1/m(V'/V)^{1/2} \quad (\text{Angular Magnification})$$

$$x'/x = m^2(V'/V)^{1/2}$$

$$C'_s = C_s m^4 (V'/V)^{3/2}$$

$$S = (1 + 1/m)f$$

$$S' = (1 + m)f'$$

Figure 2-6. Basic Optical Relations

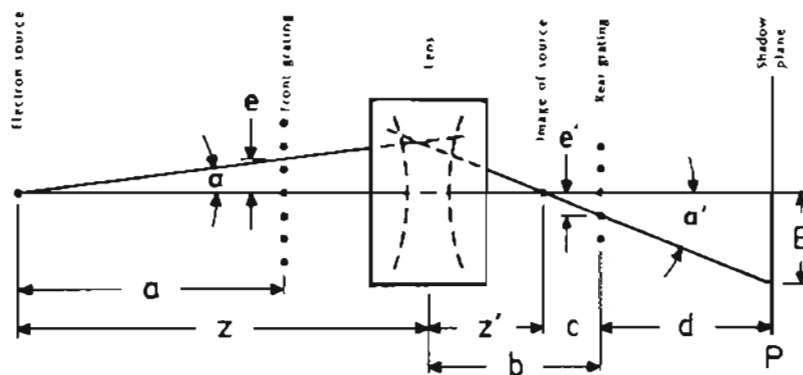


Figure 2-7. Nomenclature for the Calculation of the Spherical Aberration

and the lateral magnification  $m$  becomes

$$m \equiv \alpha/\alpha' = (M'/M)/(c/a). \quad (2-33)$$

The spherical aberration of the lens will tend to distort the grid shadows on the fluorescent screen. The malformation of the shadows looks like either pin-cushion or barrel distortion. However, this shadow distortion is in fact caused by the spherical aberration induced variations in  $z'$  and  $m$  versus the height of incidence of the rays at the lens. The amount of malformation of the shadow of the front grating can therefore be written to second order in terms of the height  $e$  at which the ray intersects the front grid

$$M = M_0(1 + \beta n^2), \quad (2-34)$$

where  $M_0$  is the paraxial shadow magnification and  $\beta$  is a dimensionless distortion coefficient, and  $n=e/e_1$  with  $e_1$  the unit height above the axis. Similarly the rear grid magnification is expressed as

$$(M' - 1)^{-1} = (M'_0 - 1)^{-1}(1 + \beta' n^2). \quad (2-35)$$

Note that the rear grid magnification  $M'$  depends on the object-side ray height  $n$ . It therefore becomes necessary to determine that value of  $n$  which corresponds to the  $n'$  at which the image-side data are taken. This conversion is undertaken by plotting  $E$  versus  $n$  and  $n'$  and reading the value of  $n$  which corresponds to  $n'$  for a given  $E$  value. Plots of  $M$  versus  $n^2$  and  $(M' - 1)^{-1}$  versus  $n^2$  are used to determine the distortion coefficients  $\beta$  and  $\beta'$ , and the paraxial magnifications  $M_0$  and  $M'_0$ . In the object-side plot,  $M_0$  is the axis-intercept and the slope of the best fitting line is taken to be  $M_0\beta$ . The image-side information is obtained similarly, recalling of course that the plot is in terms of  $(M' - 1)^{-1}$ . With the determination of the paraxial grid magnifications, the calculation of the paraxial image distance and magnification is then straight forward from equations 2-32 and 2-33.

From the relations for linear magnification in figure 2-6, noting that  $x$  ( $x'$ ) may be given as the difference between  $z$  and  $g$  ( $z'$  and  $g'$ ), and using the fact that the symmetry of the lens implies  $f-f'$  and  $g-g'$ , one has the relation

$$m = f/(z - g) = (z' - g')/f, \quad (2-36)$$

which may be reduced to

$$f = (z - z')/(1/m - m) \quad (2-37)$$

$$g = z' - fm. \quad (2-38)$$

Insertion of the paraxial values  $z'_0$  and  $m_0$  will give the paraxial values  $f_0$  and  $g_0$ .

To determine the changes in the focal distance and the focal lengths, let the difference operator act on a modified form of equation 2-36 to give

$$(\Delta z - \Delta g)(z' - g) + (\Delta z' - \Delta g)(z - g) = 2f\Delta f, \quad (2-39)$$

which upon substitutions from equation 2-36 may be reduced to

$$m^2(\Delta z - \Delta g) + \Delta z' - \Delta g = 2m\Delta f. \quad (2-40)$$

Assuming that the position of the source is fixed, implying that  $\Delta z = 0$ , equation 2-40 may be reduced to

$$\Delta z' = (1 + m^2)\Delta g + 2m\Delta f. \quad (2-41)$$

Professor Rempfer continues the derivation by noting that the variations of both  $f$  and  $g$  with ray height  $P$  can be expressed to second order by

$$\Delta f/f_0 = S_f P^2/f_0^2 = S_f(1 + 1/m_0)^2 \alpha^2 \quad (2-42)$$

$$\Delta g/f_0 = S_g P^2/f_0^2 = S_g(1 + 1/m_0)^2 \alpha^2, \quad (2-43)$$

where  $\alpha$  is the angle of the incident ray, and  $S_f$  and  $S_g$  are dimensionless spherical aberration coefficients for the focal length and focal distance, respectively. By considering the cases of  $z = \infty$  and  $z \neq \infty$ , which give zero and finite magnifications respectively, she continues by expressing  $S_f$  and  $S_g$  in terms of experimentally determined quantities

$$S_f = - [(1 + m_0^2)C_1 - m_0 C_2] / [(1 - m_0^2)((1 + 1/m_0)\alpha_1)^2] \quad (2-44)$$

$$S_g = -(C_2 - 2m_0 C_1) / \{(1 - m_0^2)(1 + 1/m_0)\alpha_1\}^2, \quad (2-45)$$

where the constants are given by  $C_1 = \beta - \beta'/M'_0$ ,  $C_2 = c_0 \beta'/f_0$ , and  $\alpha_1 = e_1/a$  is taken to be the angle subtended at the source by a single front grating spacing. With substitutions from equations 2-42 and 2-43, equation 2-41 then reduces to,

$$\Delta z' = [(1 + m_0^2)S_g + 2m_0 S_f](1 + m_0)^2 f_0 \alpha'^2. \quad (2-46)$$

If the spherical aberration is defined in terms of the image resolution limit<sup>7</sup>

$$r'_s = C'_s \alpha'^3 = \Delta z' \alpha' / 4 \quad (2-47)$$

one then obtains a relation for the image side spherical aberration as

$$C'_s = -\Delta z' / (2\alpha')^2 \quad (2-48)$$

in which  $\Delta z'$  is taken from equation 2-46. The full form of the object-side spherical aberration is then

$$C_s = -[(1 + 1/m^2)S_g + 2S_f/m](1 + 1/m)^2 f / 4, \quad (2-49)$$

where the minus sign is due to a difference in sign conventions. Therefore, in the limiting case of  $m = \infty$ , the object-side aberration becomes

$$C_s(\infty) = C'_s(0) = -S_g f_0 / 4. \quad (2-50)$$

A simpler, less rigorous technique would simply entail Spangenberg's and Field's technique of plotting the variation of the crossover point of the image-side rays versus radial distance. Professor Rempfer's technique on the other hand gives a complete theoretical explanation of the process, and is therefore more interesting and more informative.

References

1. O. Klemperer, Electron Physics, (Butterworths, London, 1972) p.4
2. J. Arol Simpson, "Design of Retarding Field Energy Analyzers", Rev. Sci. Instr., 32, 1961, p.1289
3. L.W. Swanson, private communication.
4. Karl Spangenberg and Lester M. Field, "Some Simplified Methods of Determining the Optical Characteristics of Electron Lenses", Proc. I.R.E., March 1942, pp. 138-144
5. I. G. Maloff and D. W. Epstein, Electron Optics in Television, (McGraw-Hill, New York, 1938) pp.81-89
6. Gertrude F. Rempfer, "Unipotential electrostatic lenses: Paraxial properties and aberrations of focal length and focal point", J. Appl. Phys. 57(7), 1 April 1985, pp.2385-2401
7. O. Klemperer, M.E. Barnett, Electron Optics, (Cambridge University Press, Cambridge, 1971) pp.174-175

### Chapter III

#### Experimental Arrangement

Measurement of the pertinent properties of the beam modulating lens necessitated two separate experimental arrangements. The first phase utilized photographic data of the measurement grid images to determine the magnification of the lens at various voltage configurations. With this information, along with the necessary cardinal lengths which were measured in a similar fashion, it was possible to calculate the spherical aberration coefficient of the lens from a completely experimental basis. The second phase of measurement entailed the determination of the voltage change on the central electrode needed to block, or cut-off the electron beam. These experiments were pertinent since it was necessary to determine the energy resolution of the lens. As with the first phase of experimentation, several experimental arrangements were used before a satisfactory one was discovered. The following will describe both the successful and the unsuccessful techniques in the belief that knowing what not to do is often as important as knowing the technique used. Note that all the potentials quoted were negative, and were referenced to ground.

The cathode used was a cold (room temperature) tungsten <310> field emitter, which effectively provided a point source of illumination. It was held at a potential between 1500 and 2300 volts to deliver a beam current between 1 and 30  $\mu$ A. The  $\beta$ -ring or anode was therefore kept at

zero potential along with the first and fifth elements of the lens. The two intermediate or focusing electrodes were set at identical potentials within the range of 0 to 1800 volts for a given run, usually at a potential between 80% and 90% of that on the central electrode. The central electrode voltage was the one of main interest, since it would determine the beam cut-off capabilities of the lens. It was operated within the range of 1500 - 2000 volts depending on whether photographic data or beam cut-off data were being measured.

The lens was always operated in an electrically symmetric fashion, centered on the central electrode with the outermost electrodes always at ground. This greatly reduced the number of possible voltage configurations. For example, given  $N$  voltage ratios possible in the symmetric arrangement used, running the lens asymmetrically with non-zero potentials on the outer electrodes could provide up to  $N^4$  possible voltage configurations. Although there could theoretically be an optimal operating configuration in that larger pool, it was deemed extremely unlikely that asymmetrical operation would improve the characteristics of the lens. This conclusion was based on the fact that the lens was designed to be run symmetrically, and on the understanding of Simpson's filter lens which is run in a symmetric mode.

Both phases of this experiment necessitated the use of high voltage power supplies to operate the lens and the cathode. Three such devices were used, each of which was verified to have output fluctuations of less than two volts at 1000 volts of output. This was the limit of resolution of the test apparatus which included a Tektronix 475 oscilloscope and a Tektronix high-voltage oscilloscope probe. The power supplies used were a

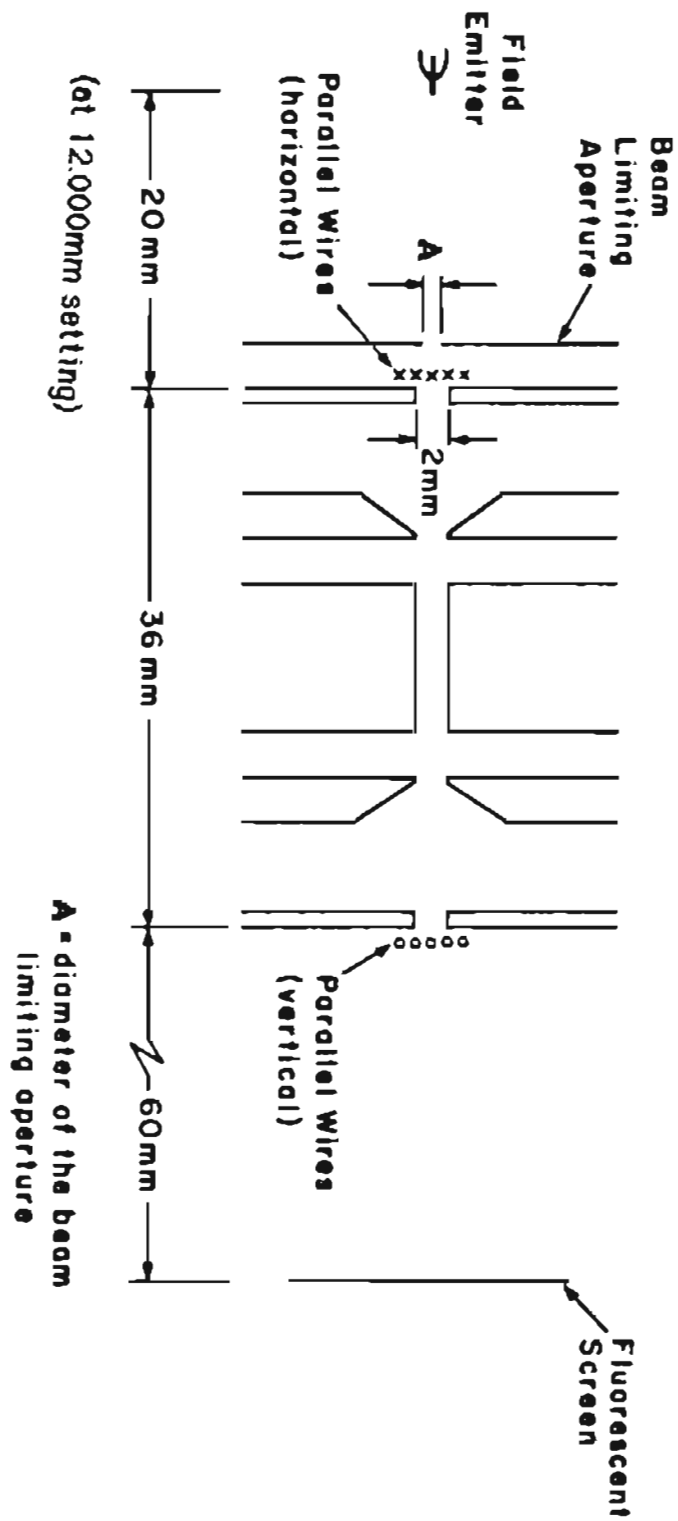


Figure 3-1. Experimental Arrangement for the Measurement of the Spherical Aberration

Fluke model 4108 to drive the emitter, a Power Designs model HV-1543 connected to the intermediate or focusing electrodes, and either a Bertan Associates model 315, or model 205N on the central electrode, depending on the experimental phase.

The theoretical basis for the experimental arrangement to determine cardinal lengths and the spherical aberration coefficient of the lens was discussed earlier as the technique developed by Spangenberg and Field<sup>1</sup> (see chapter II). Figure 3-1 shows the physical arrangement and important dimensions of the lens, the measurement grids, and the fluorescent screen. The diameter of the beam limiting aperture was 1000  $\mu\text{m}$ , so that several measurement grids could be seen. The cathode was mounted on a three dimensional (plus rotation) stage<sup>3</sup> allowing alignment of the emitter in the z-axis to within 1  $\mu\text{m}$ . Opposite the emitter and the stage was a high vacuum window through which the back of the fluorescent screen was viewed and photographed.

Several photographic arrangements were tried before an acceptable method was discovered. The first method used a Polaroid microscope camera, photographing the screen image through a microscope. It was hoped that a higher degree of photographic magnification would be attained through the microscope. This method was abandoned however because of poor focusing ability and because the image lost so much intensity through the microscope that exposure times of several minutes could not resolve the image.

The second method attempted was based on a 35mm camera equipped with a macro lens attachment. The film used in this attempt was a Polaroid<sup>2</sup> 35mm type which allowed immediate, non-darkroom

development. This film however proved to have a reflectance so much higher than standard 35mm films that once again, exposure times of several minutes were unable to resolve any image. The conclusion from these results is that Polaroid process films are poorly suited to photographing relatively dim fluorescent screen images.

The final method used standard color print film, ASA 100, in the 35mm camera with the macro lens attachment. The choice of the ASA 100 film was based on a compromise between exposure speed and high contrast capability. This arrangement allowed for fast and convenient commercial developing, and was perfectly adequate for measurement purposes.

The photographic negatives were enlarged and printed in a black and white format. The enlargements were made using a Polycontrast #1 filter set at to exposure time of 10 seconds with an f-stop setting of 3.5. The paper used was Polycontrast II RC Rapid Paper, a high contrast type to emphasize the relatively dim images of the grid wires.

There were two resulting photographic data sets. In the first set the emitter was positioned at 18.190mm on the z-axis, while in the second set the emitter was at 12.000mm. The tip of the emitter was approximately 20 mm (0.793 inches) from the front grid at the 12.000mm setting. With the change in emitter to lens distance between the two cases being 6.190mm, the percentage change in the emitter to lens distance is approximately 15%. Such a difference in the operating distances is nonnegligible, and therefore useful in the determination of the spherical aberration coefficient of the lens.

The importance of the size of voltage swing needed to cut-off the

beam is based on the fact that the lens is intended to run at high frequencies. As such, the lower the voltage change necessary to block the beam, the lower the voltage which has to be switched at high frequencies. The target for this lens design was that it be able to cut-off an electron beam with a five volt change on the central electrode.

The experimental arrangement used in the first coarse measurements of the cut-off properties is the same as that used in the first phase of testing. It was taken in a completely manual fashion in which for a given focus voltage, the central electrode voltage was increased until the image on the fluorescent screen went blank. This was simply done to quickly check that the lens did in fact block the beam. Again, as it always was, the emitter was mounted on a 3-dimensional (plus rotation) stage.

During these tests the screen image would flicker a great deal. In fact, the diameter of the image would occasionally change by a factor of approximately two, very quickly. The behavior seemed to indicate that some part of the test apparatus was charging and discharging. To alleviate the problem, the lens was surrounded by a grounded, conductive shield, and the fluorescent screen was better grounded to its mount by painting carbon paste onto the contact area. It was hoped that the shield would eliminate most problems due to the surface charging of the glass rods on which the lens was mounted, and that it would shield the beam from the sea of scattered electrons floating about the chamber. These precautions eliminated the problem.

Following the above tests, several modifications were made to determine the cut-off potential more quantitatively. A Faraday cup replaced the phosphor screen as the cut-off measurement device. The

Faraday cup was connected to a Keithley 600A electrometer which measured the current, with grounded shielding protecting all exposed electrical parts of the Faraday cup both inside and outside the chamber. Also, the limiting aperture was replaced so that the electron beam entering the lens better approximated the paraxial case. The aperture used in the cut-off experiments was 150 micrometers (6 mils) in diameter. Under the operating conditions used, this gave an acceptance half angle of about 3.3 milliradians from the emitter to the limiting aperture.

Since the initial observations showed a great deal of noise on the Faraday cup current reading, an arrangement was implemented to average the current readings over time. This was done with a Transera brand A/D converter used in conjunction with a Tektronix 4051 microcomputer. With this arrangement, 1500 current readings were taken and averaged for each focus voltage setting.

Although this arrangement gave semi-quantitative results, it was still an inefficient and error prone technique. First of all, the long sampling times of several minutes needed to obtain 1500 readings aggravated the problem of emitter contamination over time. Secondly, and more importantly, the extreme noise measured from the Faraday cup was actually symptomatic of other experimental problems which needed to be rectified. These problems were resolved by 1) running the tests at a lower chamber pressure to increase the "clean time" of the emitter; 2) completely automating the testing technique to shorten the running time of the emitter; and 3) plotting the analog results with a X-Y recorder to obtain a continuous record of the current.

All of the experimental design alterations were accomplished by

driving the central electrode with a filter lens power supply unit. This unit is mainly a floating ramp generator within a range of  $\pm 20$  volts, floated on top of a Bertan Associates model 205N high voltage power supply. The upper and lower limits of the ramp can be set, as well as the rate and direction of the ramp. The floating ramp is fed into the central electrode of the lens, while the ramp alone drives the x-axis and a signal relative to the Faraday cup current drives the Y-axis of an X-Y recorder (see figure 3-2).

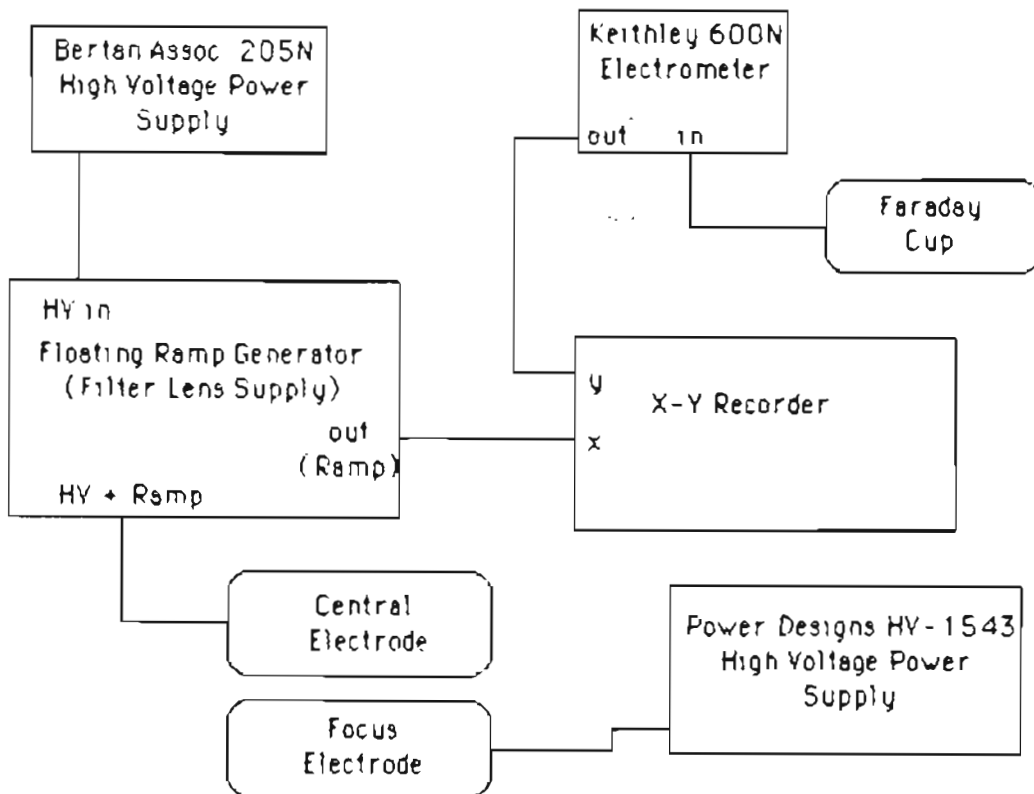


Figure 3-2. Diagram of electronics used for I-V plot of beam current versus Faraday cup current.

Since the rate of the ramp could be set, sweeps took less than a

minute each. The resulting plots were relatively noise free because of the complementary effects of pressures in the low  $10^{-9}$  or high  $10^{-10}$  torr range, and short run times. Collecting the I-V data with this apparatus gave clean, repeatable, and conclusive results.

### References

1. Karl Spangenberg and Lester M. Field, "Some Simplified Methods of Determining the Optical Characteristics of Electron Lenses", Proc. I.R.E., March, 138-144, 1928
2. Polaroid Polagraph HC 35mm autoproces black and white high contrast transparency film.
3. Huntington Laboratories Model PM600-XYZTRC three dimensional stage with rotary motion and a coaxial linear motion feedthrough. Has 6 mini-Conflat feedthroughs and is mounted on a 6 inch Conflat flange. Baking above 150 C requires removal of the micro-manipulators.

possible to plot a distinctive map of both the front and rear sets of grids. The asymmetries in the grid placement enabled a detailed determination of the ray paths through the lens. From the sample photograph below and the actual grid arrangements in Figure 4-1, it is evident that the wires in front of the the lens cast an inverted shadow on the screen (the horizontal wires) while the wires after the lens formed an uninverted shadow, implying that the image plane lay between the lens and the rear grid. In addition, since the rear grid was flush with the lens, this

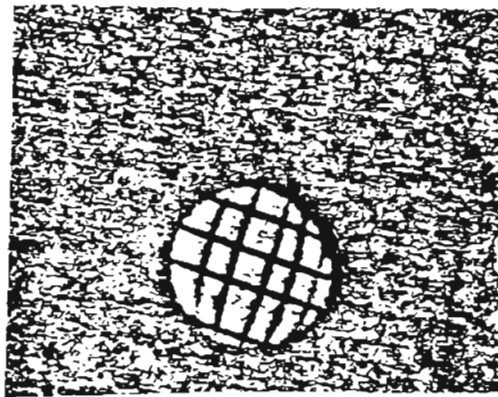
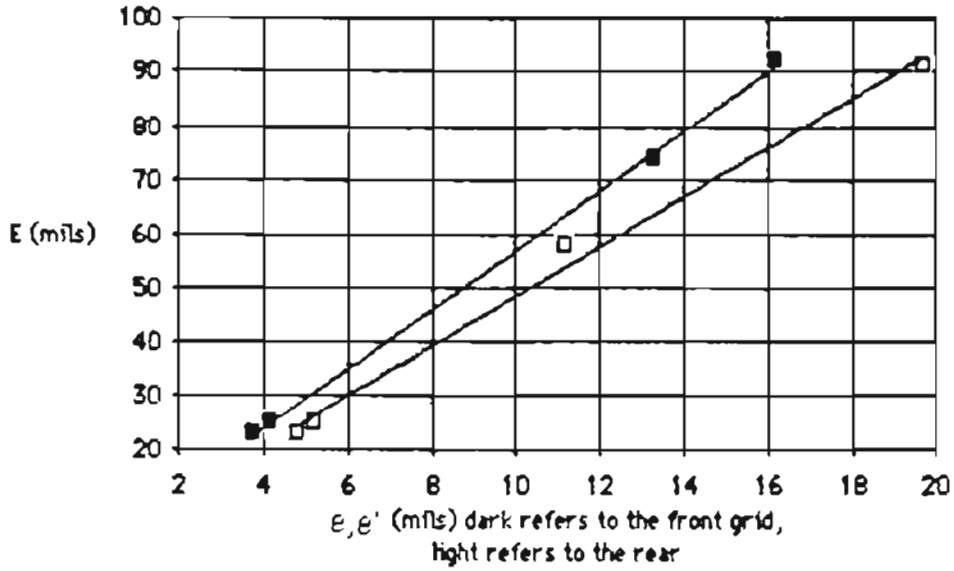


Figure 4-2. Screen Image Sample

implied that the rays crossed the lens axis within the lens, as they were predicted to by the computer calculations performed earlier.

The experimental parameters pertinent to the calculation of the spherical aberration are shown in figure 2-7. The values for the modulator lens experiment were:  $a=0.793$ " which was the distance between the electron source and the front grid,  $z=1.815$ " was the distance between the source and the reference plane (taken to be the center of the lens),  $b=3.169$ " was the distance between the the reference plane and the rear grid, and  $d=2.365$ " was the distance between the rear grid and the

Shadow Radius vs Grid Radius for photo 111



Shadow Radius vs Grid Radius for photo 151

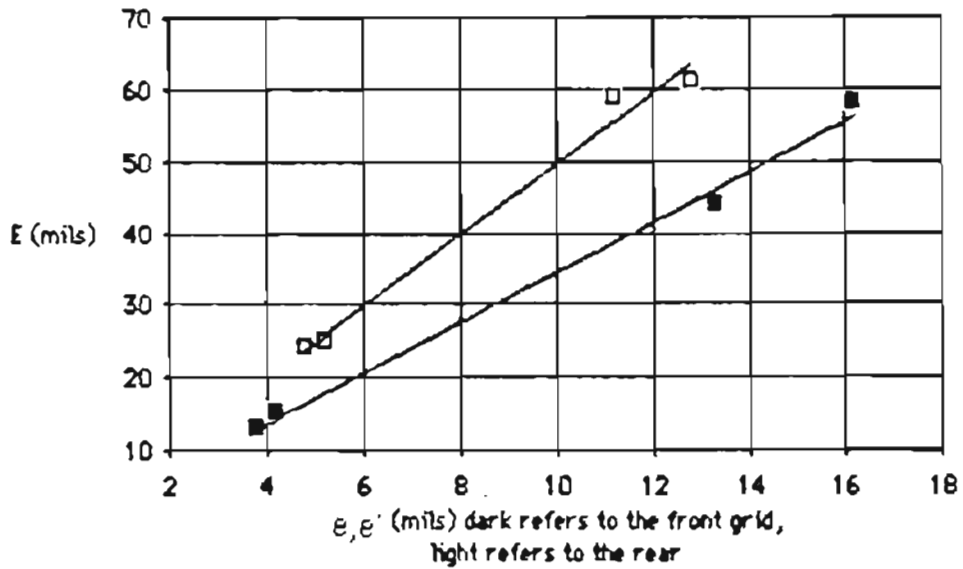
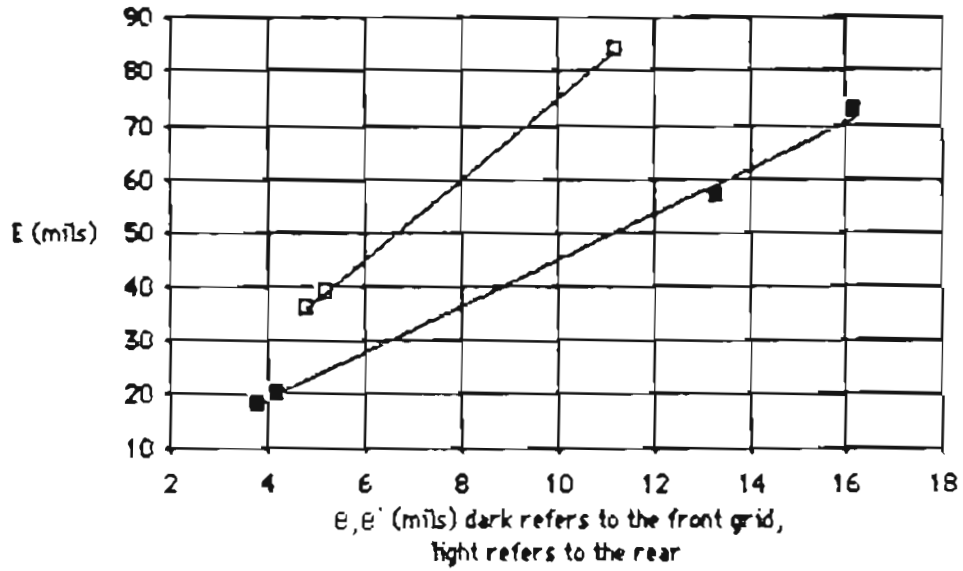


Figure 4-3(a). Shadow Radii versus Grid Radii for Photographs 111 and 151

Shadow Radius vs Grid Radius for photo 161



Shadow Radius vs Grid Radius for photo 171

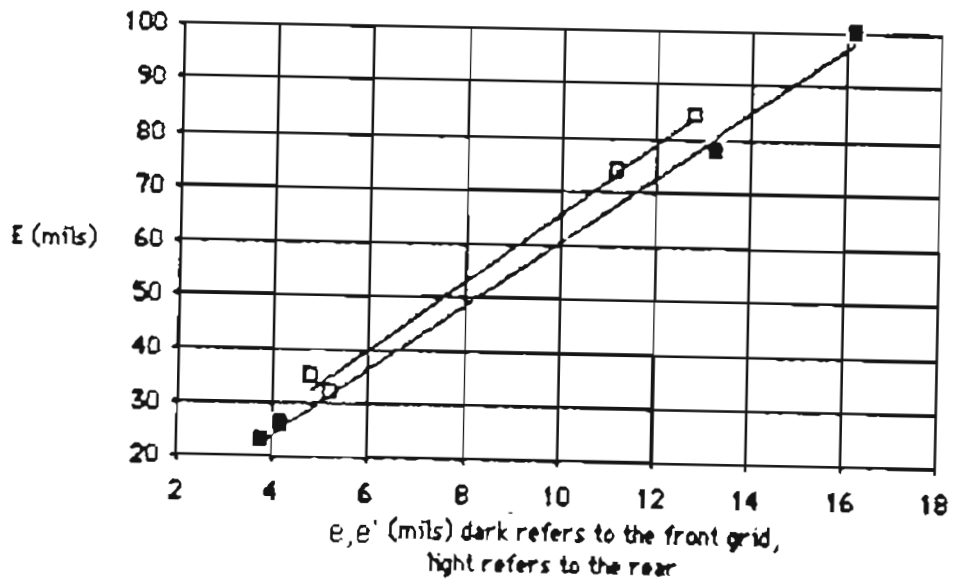


Figure 4-3(b). Shadow Radii versus Grid Radii for Photographs 161 and 171

fluorescent screen.

In accordance with the theoretical derivation of the spherical aberration calculation in chapter 2, the first measurements to be made were the shadow radii versus the grid radii for both the front and rear grids. The results of these measurements, along with best fitting lines are shown in figures 4-3 and 4-4. For each of the four data photographs used, one may refer to these two figures to find the front grid radius ( $n$ ) which corresponds to the rear grid radius ( $n'$ ) for a given value of  $E$ .

Since the grid magnifications are given by

$$M = E/e \quad (4-1)$$

$$M' = E/e', \quad (4-2)$$

the measurements taken for the plots in figures 4-3 and 4-4 can also be used to plot the grid magnifications. Recalling that the spherical aberration was taken to be a manifestation of second order perturbations in the grid magnifications of the form

$$M = M_0(1 + \beta e^2) \quad (4-3)$$

$$(M' - 1)^{-1} = (M'_0 - 1)^{-1}(1 + \beta' e^2), \quad (4-4)$$

plots of  $M$  and  $(M' - 1)^{-1}$  versus  $e^2$  can be used to determine the paraxial grid magnifications  $M_0$  and  $M'_0$ , as well as the magnification distortion coefficients  $\beta$  and  $\beta'$ . Figures 4-5 contains the plots of  $M$  versus  $e^2$  for the four data photographs, and figure 4-6 contains the corresponding information for the rear grids. The results of these plots are listed in table 4-1.

With all the above results in hand, one is now adequately equipped

Figure 4-3(c). Front Grid Magnifications versus Ray Radii Squared

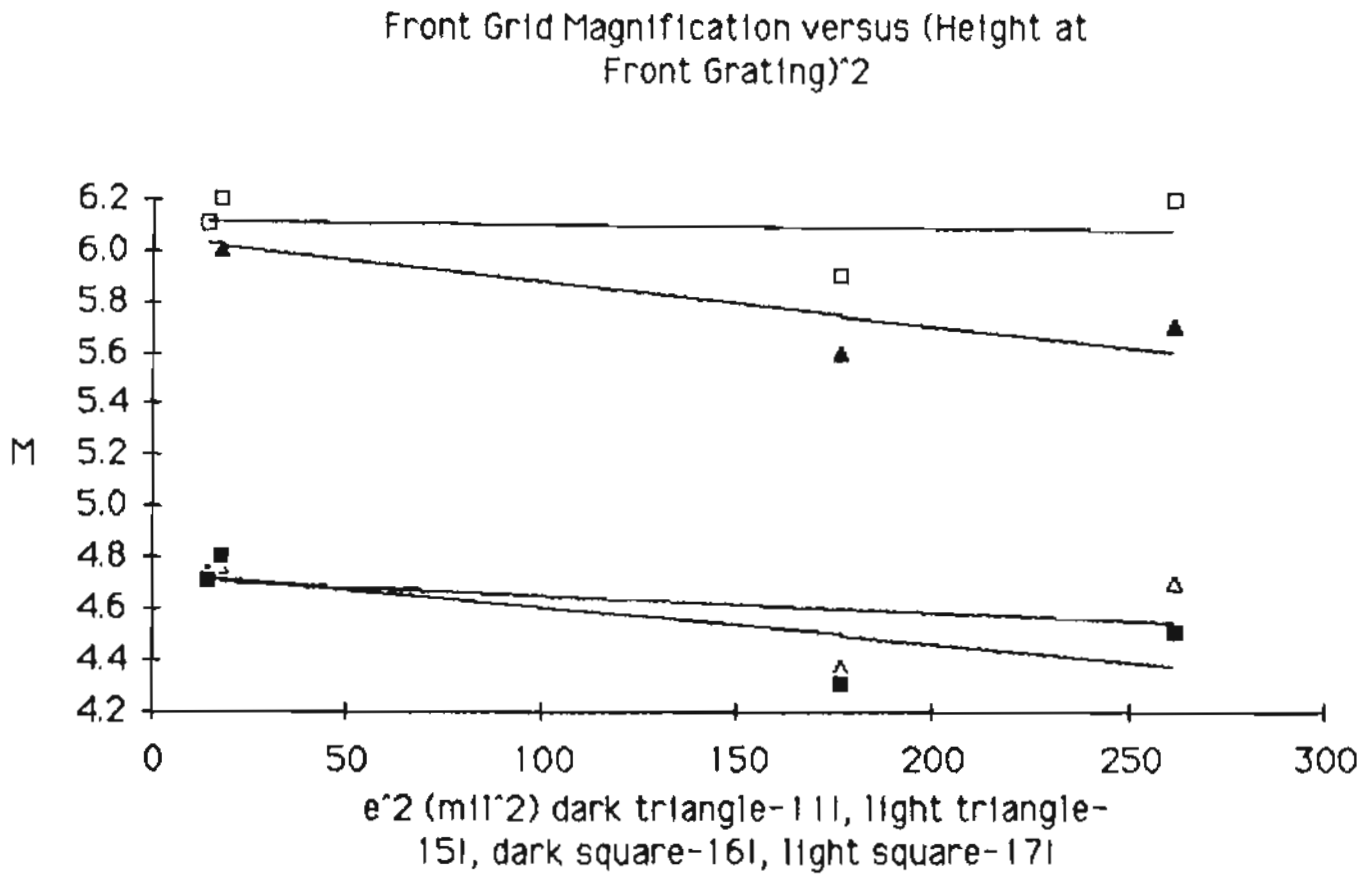
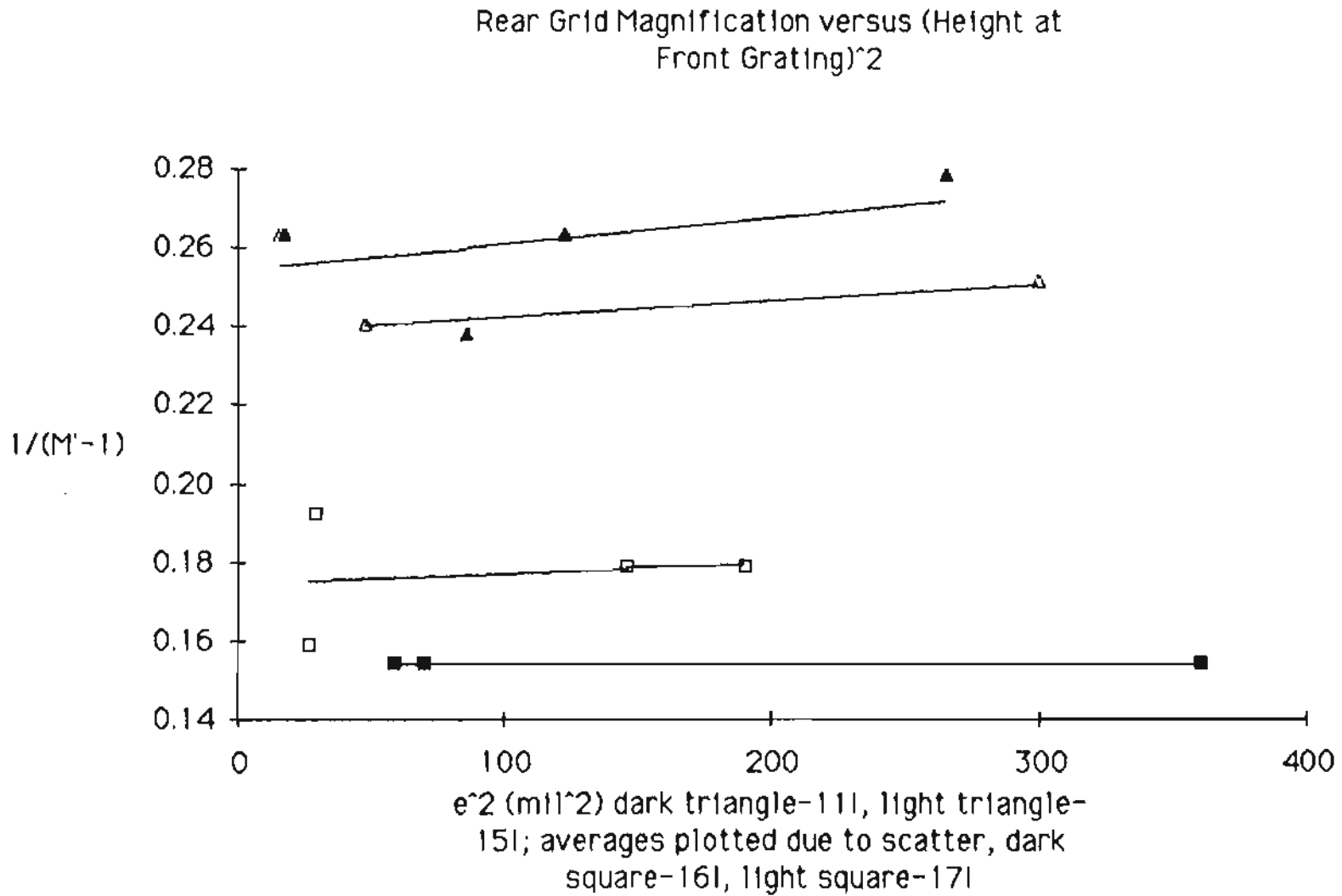


Figure 4-3(d). Rear Grid Magnifications versus Ray Radii Squared



to calculate  $S_f$  and  $S_g$ , the dimensionless spherical aberration coefficients for the focal length and the focal distance, respectively

$$S_f = -[(1+m_o^2)C_1 - m_o C_2] / [(1-m_o^2)((1+1/m_o)\alpha_1)^2] \quad (4-5)$$

$$S_g = -[C_2 - 2m_o C_1] / [(1-m_o^2)((1+1/m_o)\alpha_1)^2], \quad (4-6)$$

where  $C_1$ ,  $C_2$ , and  $\alpha_1$  are described in chapter 2. The calculation of any spherical aberration term is now possible, where specifically  $C_s(\infty)$  becomes

$$C_s(\infty) = -S_g f_o / 4. \quad (4-7)$$

Table 4-1. Paraxial Grid Magnifications and Magnification Distortion Coefficients

Photo	$M_o$	$M'_o$	$\beta$ (mil <sup>2</sup> )	$\beta'$ (mil <sup>2</sup> )
111	6.05	4.92	$-2.88 \times 10^{-4}$	$2.56 \times 10^{-4}$
151	4.75	5.17	$-1.44 \times 10^{-4}$	$2.20 \times 10^{-4}$
161	4.75	7.49	$-2.97 \times 10^{-4}$	0.0
171	6.10	6.71	$-2.66 \times 10^{-5}$	$1.75 \times 10^{-4}$

With the ability to now calculate all the spherical aberration, focal length, and focal distance information, the immediately pertinent results will be listed in table 4-2. The results to be listed will be the operating

voltages of the lens, the paraxial shadow magnification  $m_o$ , the paraxial focal length  $f_o$ , the aberration coefficients  $S_f$  and  $S_g$ , and the infinite case object-side spherical aberration  $C_s(\infty)$ . The spherical aberration value listed is the one of interest for the immediate concerns of the project. With the  $S_f$  and  $S_g$  values listed, spherical aberration coefficients at other magnifications can be calculated. The data used for these calculations are listed in detail at the end of the chapter.

Table 4-2. Spherical Aberration Results for the Modulator Lens

Photo Emitter	Central Potential (-volts)	Focus Potential (-volts)	$m_o$ (mm)	$f_o$	$S_f$	$S_g$ (mm)	$C_s(\infty)$	
111	2000	1850	1500	0.619	41	74	-76.7	789
15I	2000	1825	1750	0.779	80	82	-102	2040
16I	2000	1825	1650	0.725	54	106	-101	1353
17I	2000	1825	1450	0.574	31	44.2	-49.1	339

The original intention of the experiment was to measure the spherical aberration at a central electrode voltage nearly equal to the beam cut-off voltage. This experimental format would have determined the spherical aberration under the normal operating conditions of the lens.

However, the grid images became useless at potentials much less than beam cut-off voltage. For example, with the focus voltage equal to 1700 volts and the emitter voltage equal to 2000 volts, the grid image was extremely distorted at a central electrode voltage of 1932 volts, and at  $V_{\text{central}} = 1963$  volts the image was focused to a point. Therefore, the spherical aberration measurement was made with the central electrode potential much lower than originally intended. The reason for this is that under the normal operating conditions, the filter lens is not truly acting like a lens, in the usual sense. When operated near cut-off, the filter lens is supposed to behave like two immersion lenses back-to-back, with a cross-over produced at the center of the central electrode. A parallel beam entering the lens from the object side should be decelerated to a very low energy at the cross-over, and then be accelerated out on the image side as a parallel beam once again. This implies no lens action overall and that a more sensitive technique will be required to determine the optical properties of the system near cut-off. Since later results determined that the lens had other fundamental problems, the inability to measure  $C_s$  under normal operating conditions became a moot point.

The beam cut-off characteristics of the lens were measured at either of two focus voltages for each emitter potential. The emitter voltages used were 1400 volts and 1600 volts, and the first set was taken with the emitter at 1400 volts. The focal voltage which optimizes the cut-off properties of the lens is expected to be approximately  $V_{\text{focus}} \approx 0.95V_{\text{emitter}}$ . The focus voltages to be tested were therefore centered on this value.

The following figures plot the Faraday cup current versus the

central electrode voltage over a range of focus voltages. The first set of plots had a beam limiting aperture of  $1000\mu\text{m}$  with  $V_{\text{emitter}} = 1400$  volts and then  $V_{\text{emitter}} = 1600$  volts. The second set used a  $150\mu\text{m}$  aperture and  $V_{\text{emitter}} = 1600$  volts. The data which was taken with a  $1000\mu\text{m}$  diameter aperture corresponded to a half angle of 15.2 milliradians. This aperture was used for lack of availability of a smaller one at the time, resulting in an excessively large half angle. The data obtained using a  $150\mu\text{m}$  aperture corresponded to a half angle of 3.3 mr, which is within the preferred limit of 5mr in electron lens operation.

Table 4-3 lists the measurement and operational details from the I-V data graphs.  $V_{\text{maxI}}$  is the voltage at which the Faraday cup current leveled out, and was therefore taken to be the maximum current for that run.  $V_{\text{blankI}}$  is the voltage at which the current reached its minimum value.  $V_{\text{cut-off}}$  is the difference between  $V_{\text{maxI}}$  and  $V_{\text{blankedI}}$ , and is the voltage change necessary to block the beam.  $I_{\text{max}}$  was the maximum current value reached by the Faraday cup.

By plotting the information in Table 4-3, it is evident that there is no clear relation between the focus potential and the voltage swing needed to block the beam ( $V_{\text{cut-off}}$ ). However, interesting results may be noticed in plots of  $V_{\text{blankedI}}$  versus  $V_{\text{focus}}$  and  $I_{\text{max}}$  versus  $V_{\text{focus}}$  (see Figures 4-12 through 4-17. Note that in cases where there are two values for a data point, the average of those values is plotted.). Except for the first data point in the  $150\mu\text{m}$  case,  $V_{\text{blanked}}$  is an increasing function of the focus

Table 4-3. Results of Beam Cut-off Experiments

Figure	$V_{\text{emitter}}$ (volts)	$V_{\text{focus}}$ (volts)	$V_{\text{maxI}}$ (volts)	$V_{\text{blankedI}}$ (volts)	$V_{\text{cut-off}}$ (volts)	$I_{\text{max}}$ ( $10^{-9}$ amps)
4-4a	1400	1300	1383.5	1392	8.5	4.0
4-4b	1400	1320	1381	1392	11	8.5
4-5a	1400	1350	1385	$\approx$ 1396	11	5.0
4-5b	1400	1330	1381	1393.5	12.5	8.0
4-6a	1600	1500	1581	1593	12	9.5
4-6b	1600	1530	$\approx$ 1585	1596	11	12
4-7	1600	1560	1584	1597.5	13.5	6.0
4-8a	1600	1500	1581	1592.4	11.4	7.5
4-8b	1600	1510	1583	1593.5	10.5	7.5
4-8c	1600	1520	1584	1593.8	11.8	6.0
4-9a	1600	1530	1583	1595.8	12.8	7.2
4-9b	1600	1540	$\approx$ 1580	1596	16	9
4-10a*	1600	1520	1580.25	1595	14.75	0.65
4-10b*	1600	1500	1581	1596	15	0.85
4-11a*	1600	1560	1582	1598	14	0.48
4-11b*	1600	1540	1581	1596	17	0.79

\* This plot was taken with a limiting aperture of  $150 \mu\text{m}$ . All others used a  $1000 \mu\text{m}$  aperture.

potential. This relation implies that a greater blanking potential is needed to block a beam which is exposed to a higher focus voltage. One possible explanation for this relation is that greater focusing of the beam (i.e. a higher focus potential) decreases the beam diameter in which case the blanking potential must be increased to "tighten" the innermost annular surface of the blanking equipotential. Except for the initial point in Figure

4-14, this relation is consistent throughout the data. In fact, comparison of Figure 4-13 ( $1000\mu\text{m}$ ,  $V_{\text{emitter}} = 1600$  volts) with Figure 4-14 ( $150\mu\text{m}$ ,  $V_{\text{emitter}} = 1600$  volts) is consistent with this hypothesis in that the  $1000\mu\text{m}$  case has blanking potentials which are typically lower than the  $150\mu\text{m}$  case. The two plots then appear to converge when the focus potential is relatively large. Although this relation could not be safely extrapolated to focus voltages higher than those measured, it does seem to explain the focus voltage dependence on the blanking potential.

The plots of focus potential versus  $I_{\text{max}}$  in Figures 4-15 through 4-17 are also quite interesting. Although it could be argued that the important relation is  $V_{\text{focus}}$  versus  $V_{\text{cut-off}}$ , it can be seen in Table 4-3 that such a relation is extremely scattered and unintelligible. By plotting  $V_{\text{focus}}$  versus  $I_{\text{max}}$ , one is able to discern a consistent relation in each set of data in which  $I_{\text{max}}$  reaches a maximum value. The maxima reached can be read from Figures 4-15 through 4-17. It is clear that a convincing determination of this relation would necessitate a larger body of data, for example to determine whether or not the maxima in Figures 4-16 and 4-17 are the same. Nevertheless, there is a consistent relation outlined in the data plotted from which the optimal operation of the lens may be determined, that is, the value of  $V_{\text{focus}}$  which maximizes  $I_{\text{max}}$ .

One would expect that for a constant beam current and a constant limiting aperture size that  $I_{\text{max}}$  should be constant. It is however clear that such is not the case since there is consistently some lens configuration which maximizes  $I_{\text{max}}$ . It is therefore clear that in those lens

configurations other than the one giving  $I_{\max}$  that some fraction of the beam entering the lens does not arrive at the Faraday cup. In fact, there is no reason to believe that some fraction of the beam in the  $I_{\max}$  case is not also being "lost" within the lens. Such losses can occur in either of two ways. The electrons are either being deflected into one of the lens electrodes, or they are being deflected clear out of the lens assembly into the surrounding shield, with the former being much more likely.

Further experimentation could be used to determine where these "lost" electrons go. Since the values for  $I_{\max}$  fall off from the maximum  $I_{\max}$  for both increasing and decreasing values of  $V_{\text{focus}}$ , it seems possible that the beam is being overfocused and underfocused, respectively. The experiment would entail measuring the current on the central electrode and each of the focusing elements while the focus voltage is varied. An increase in the current on an electrode accompanied by a decrease in  $I_{\max}$  would isolate the point at which the electrons are lost.

Figure 4-4 Faraday Cup Current versus Central Electrode Voltage

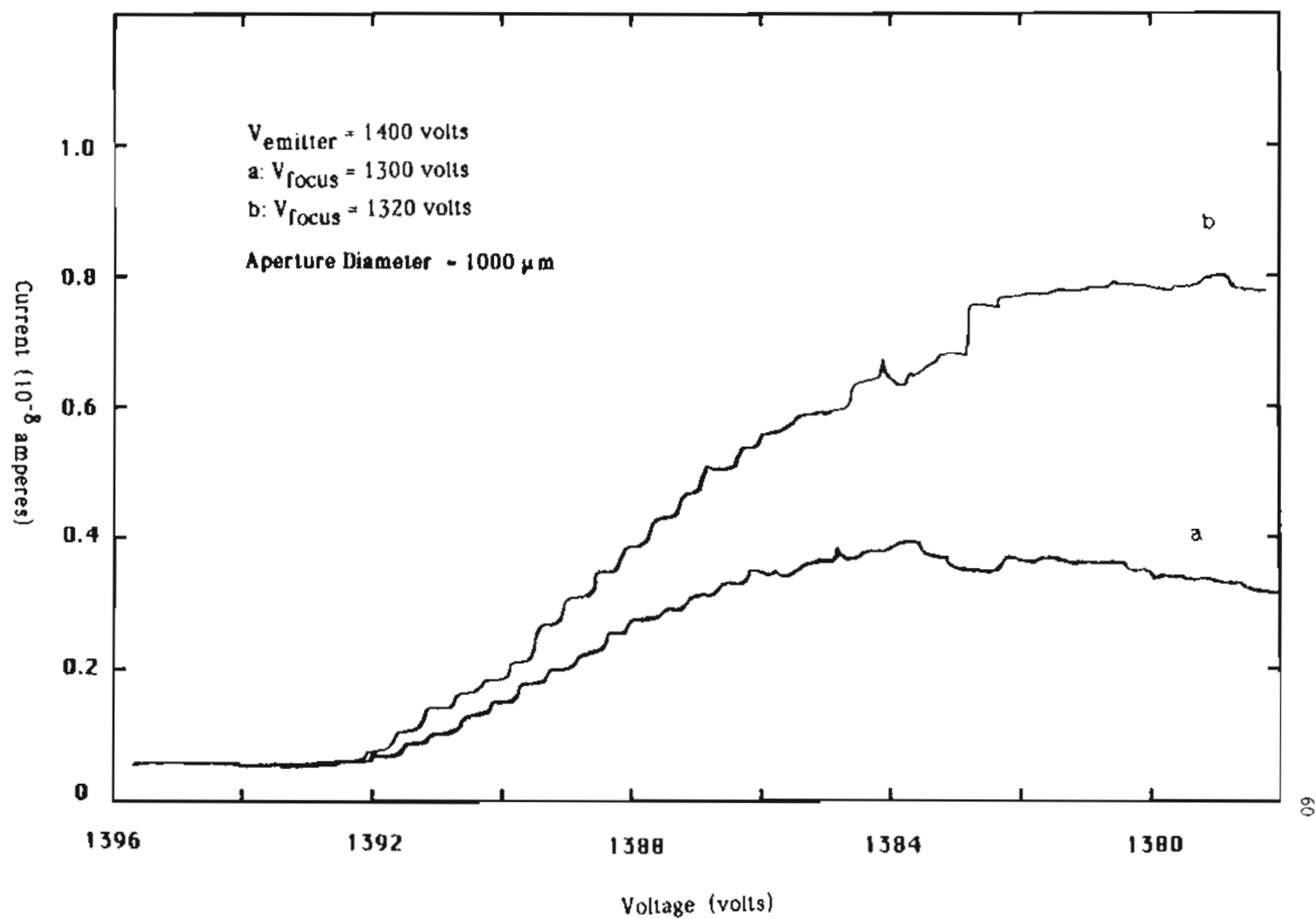


Figure 4-5 Faraday Cup Current versus Central Electrode Voltage

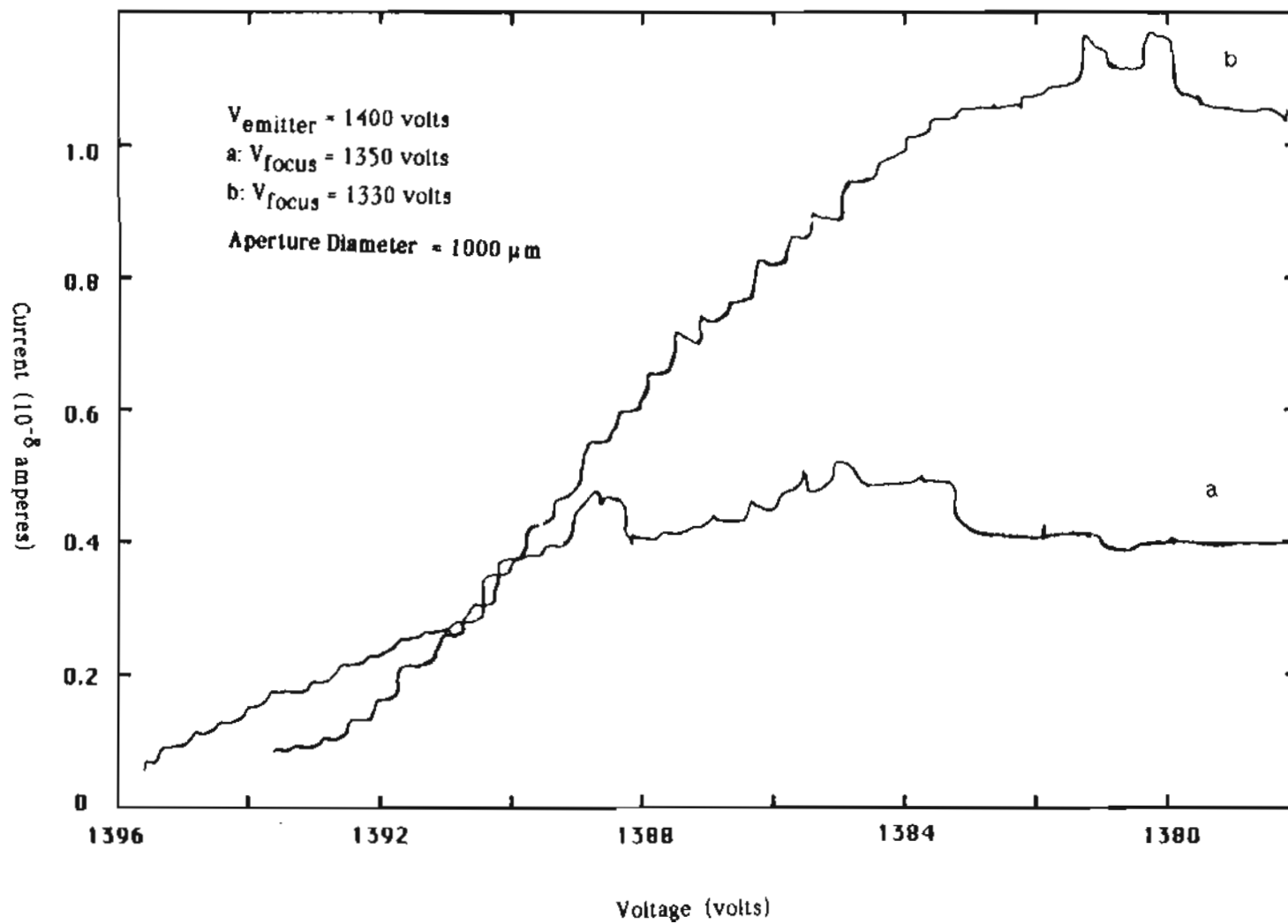


Figure 4-6 Faraday Cup Current versus Central Electrode Voltage

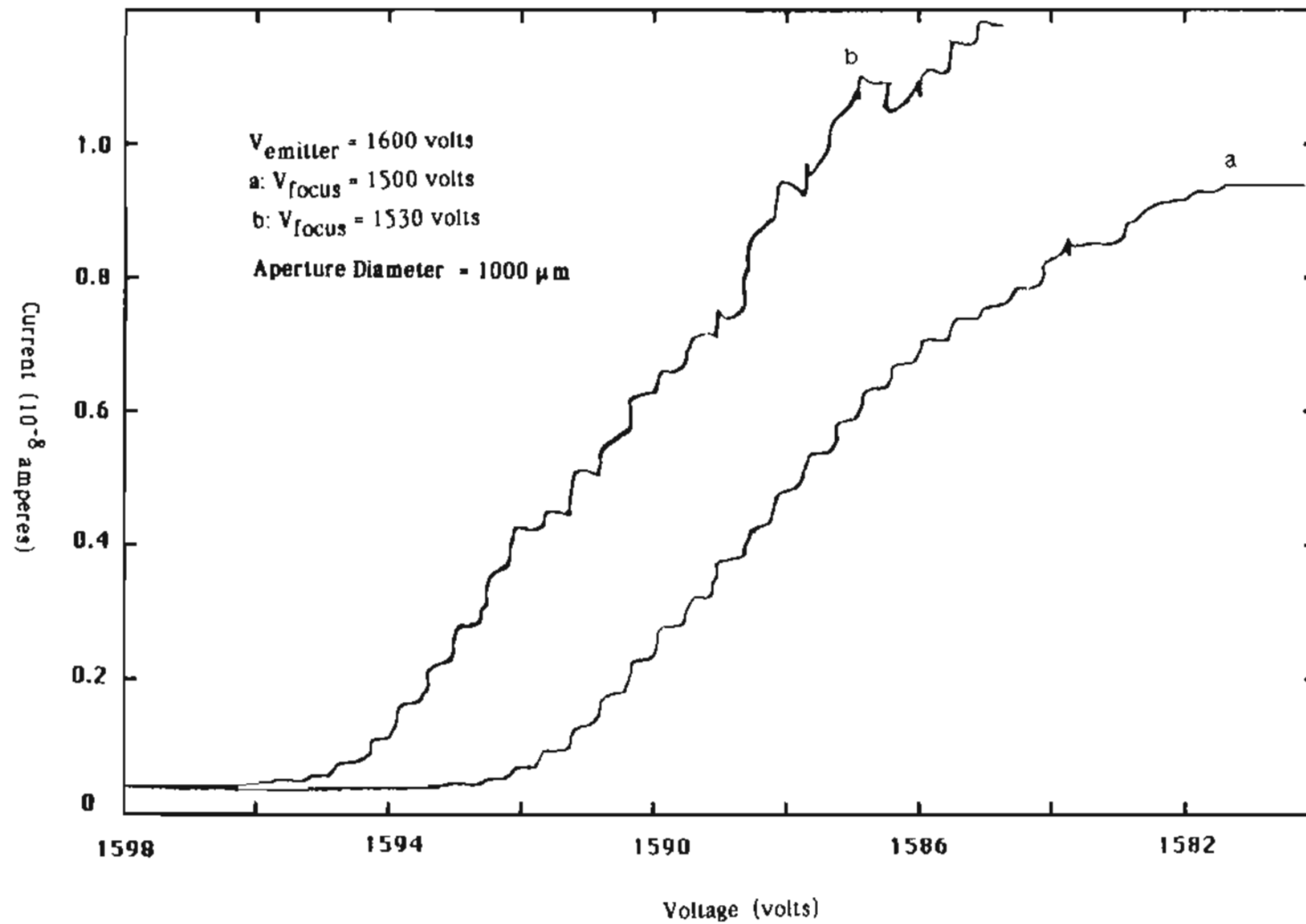


Figure 4-7 Faraday Cup Current versus Central Electrode Voltage

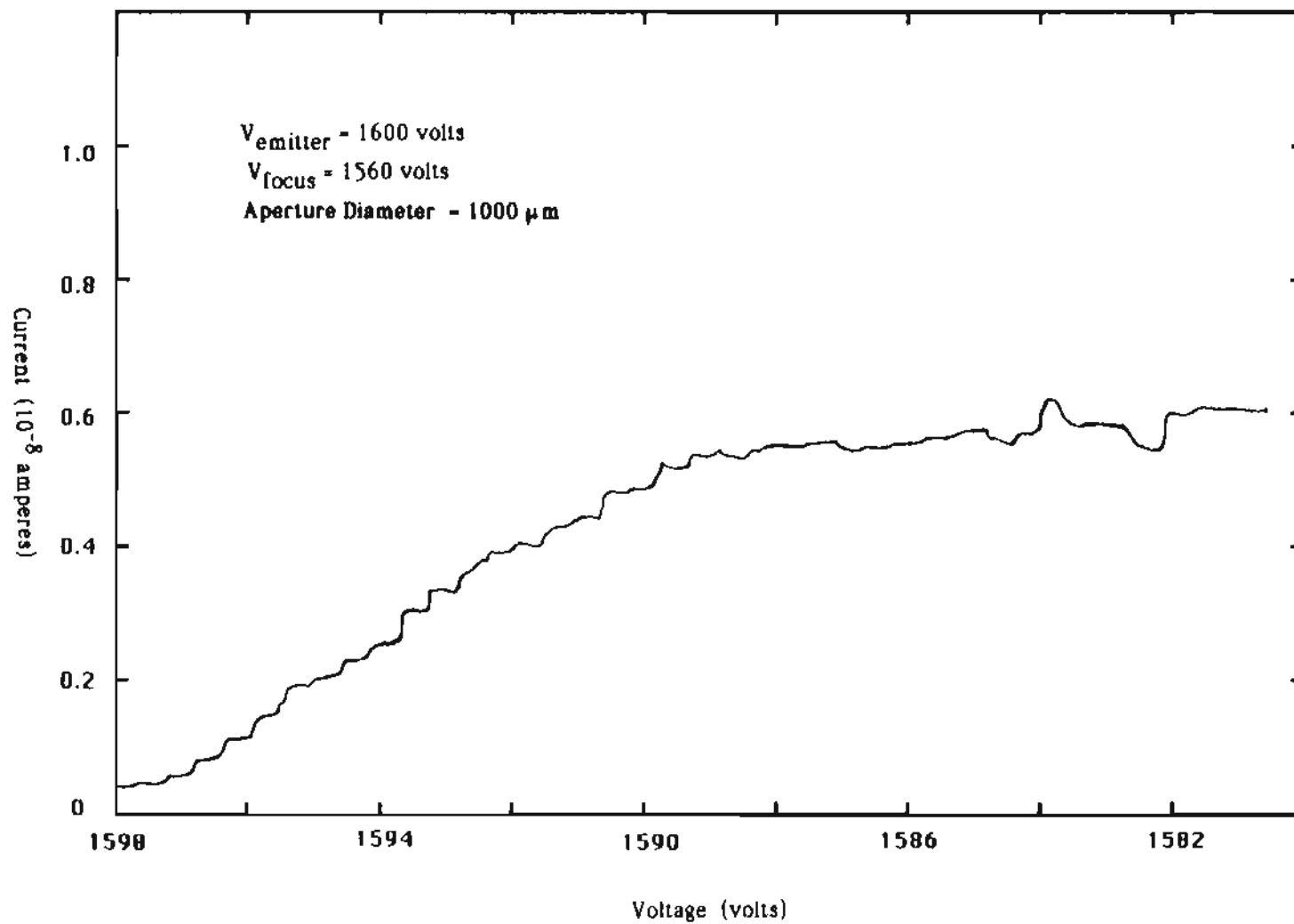


Figure 4-8 Faraday Cup Current versus Central Electrode Voltage

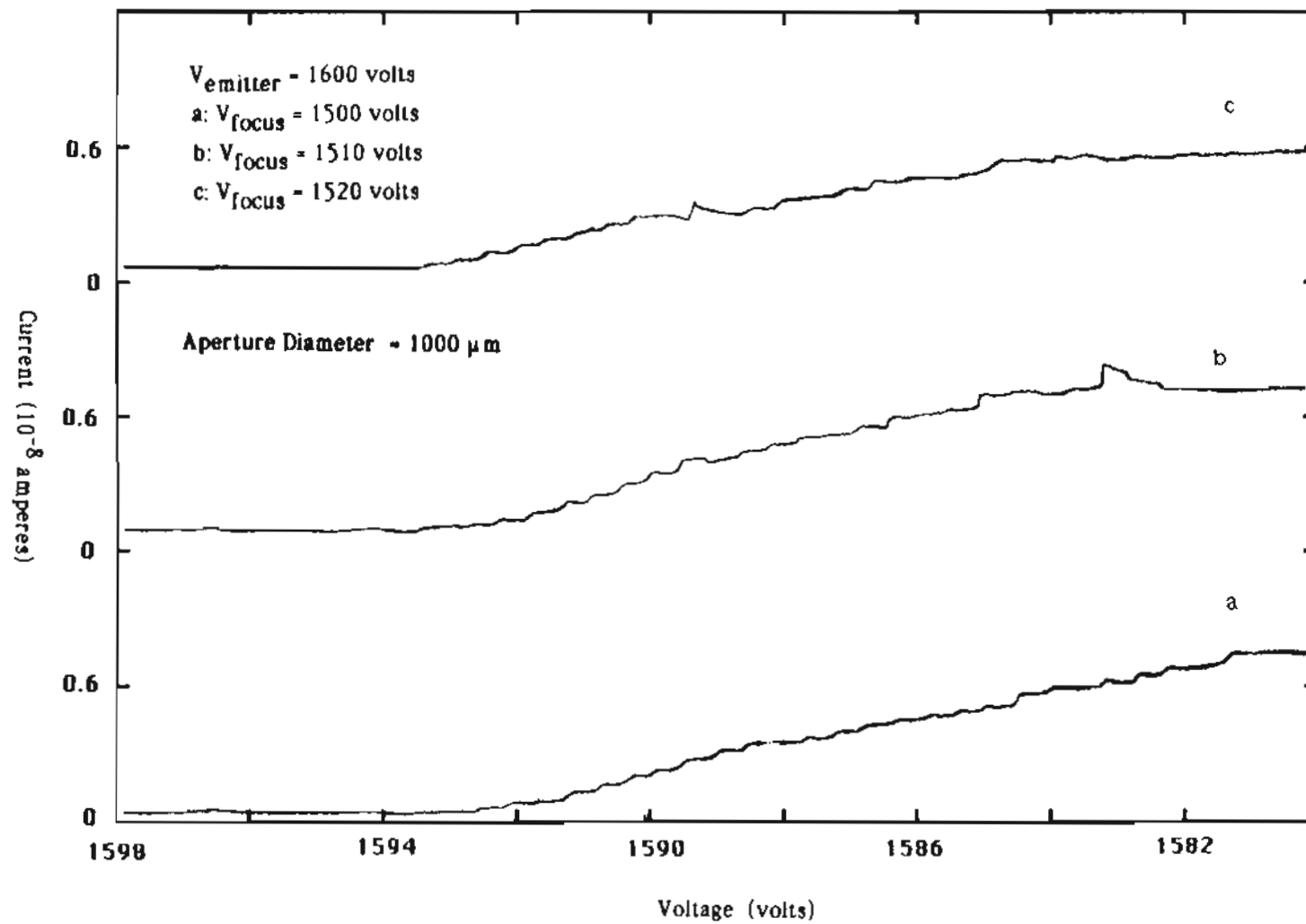


Figure 4-9 Faraday Cup Current versus Central Electrode Voltage

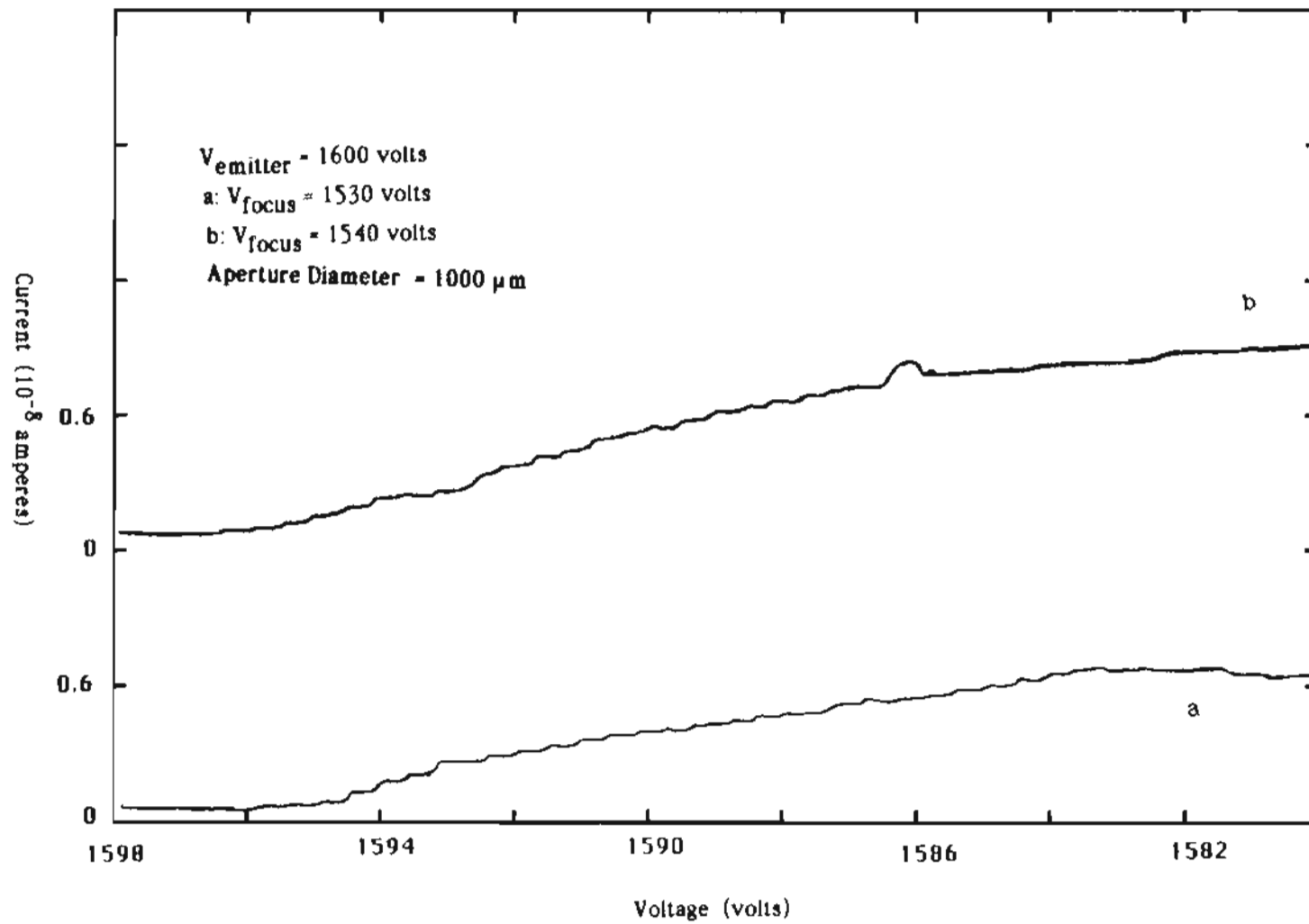


Figure 4-10 Faraday Cup Current versus Central Electrode Voltage

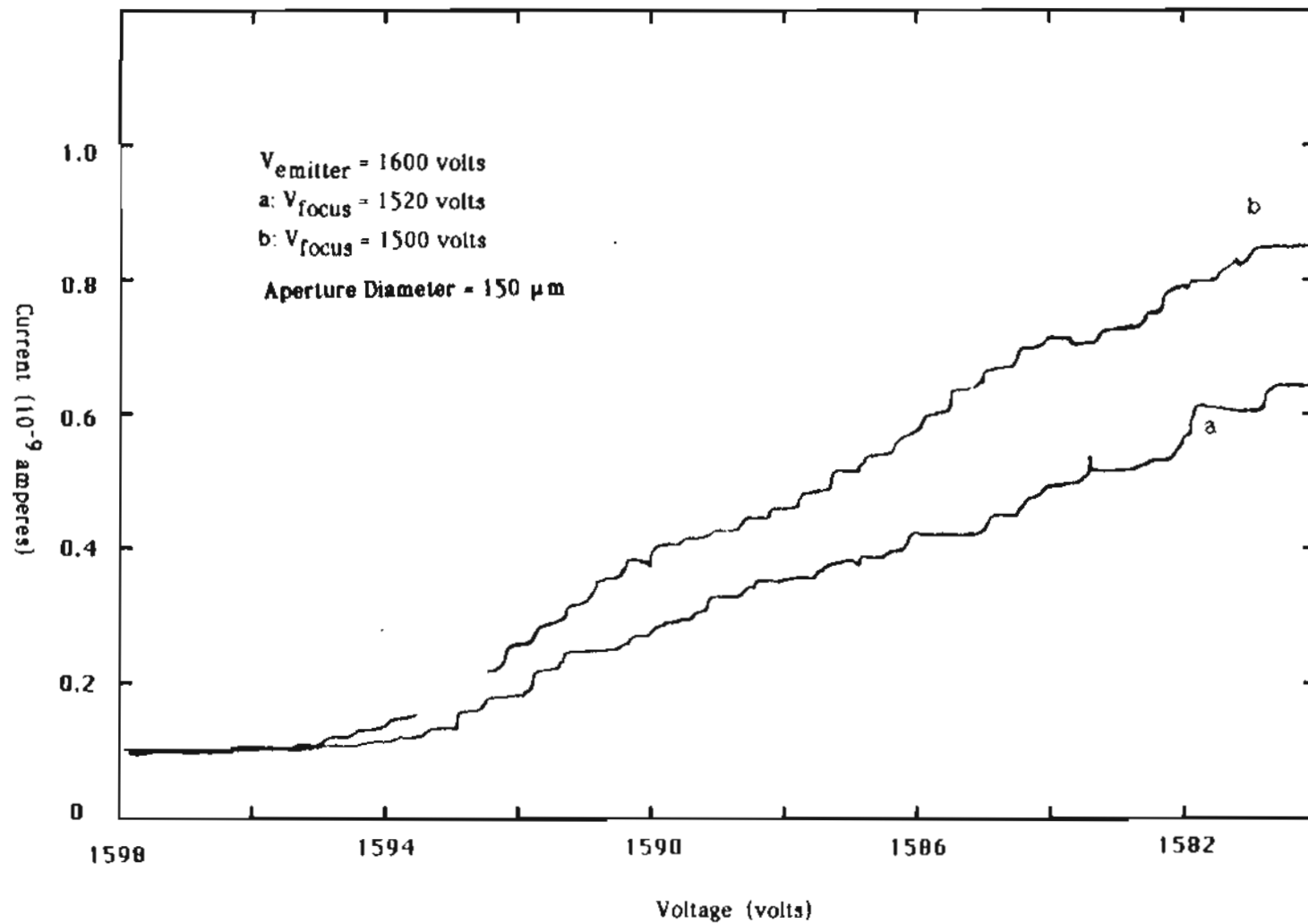


Figure 4-11 Faraday Cup Current versus Central Electrode Voltage

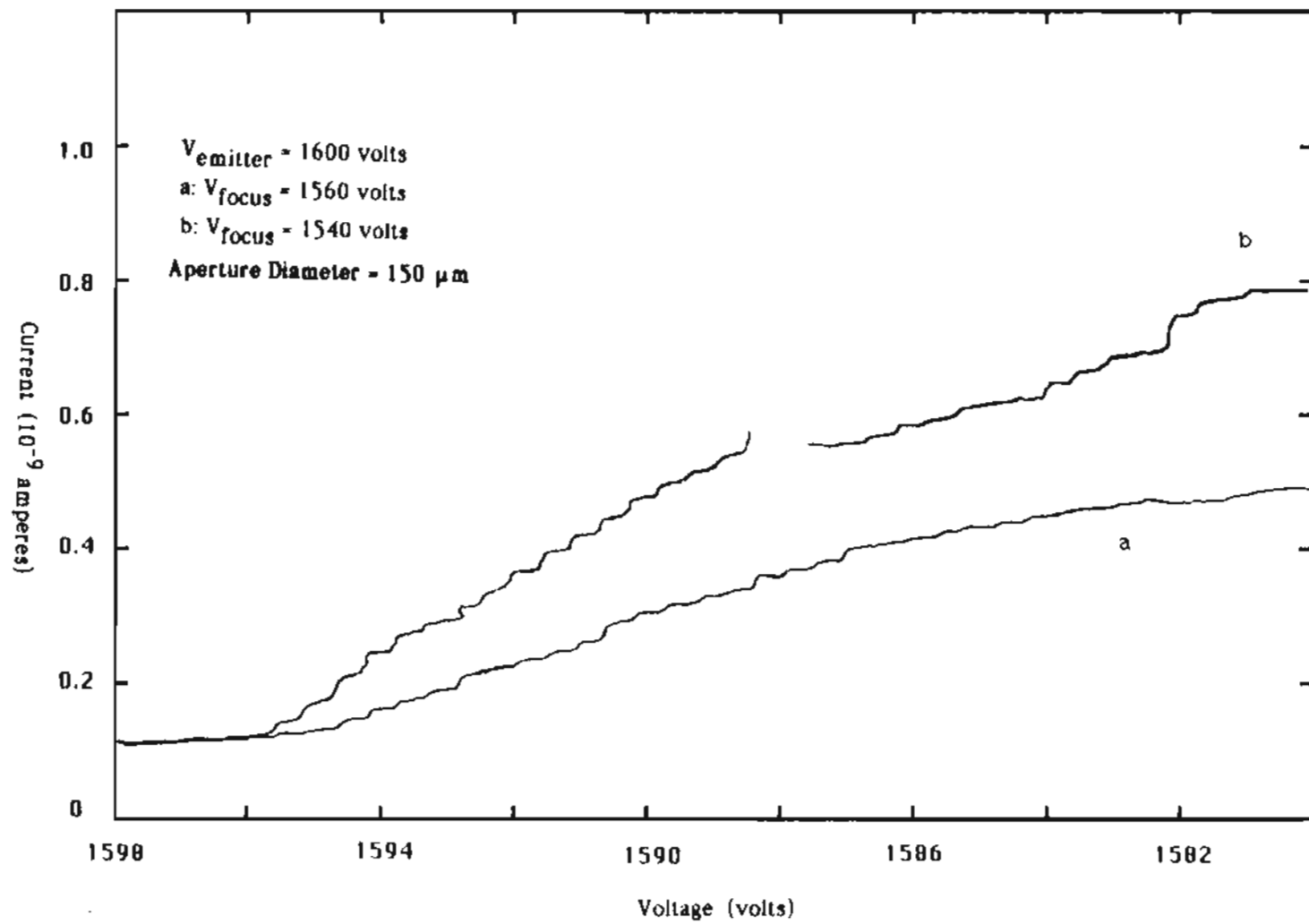


Figure 4-12. Blanked Voltage versus Focus Voltage

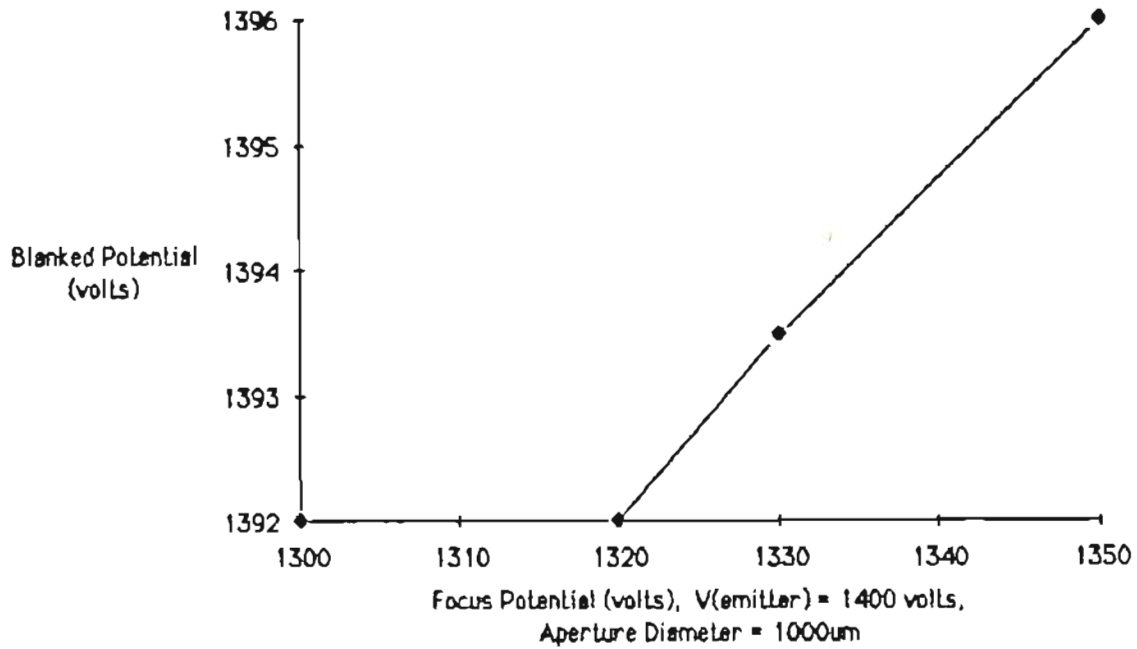


Figure 4-13. Blanked Voltage versus Focus Voltage

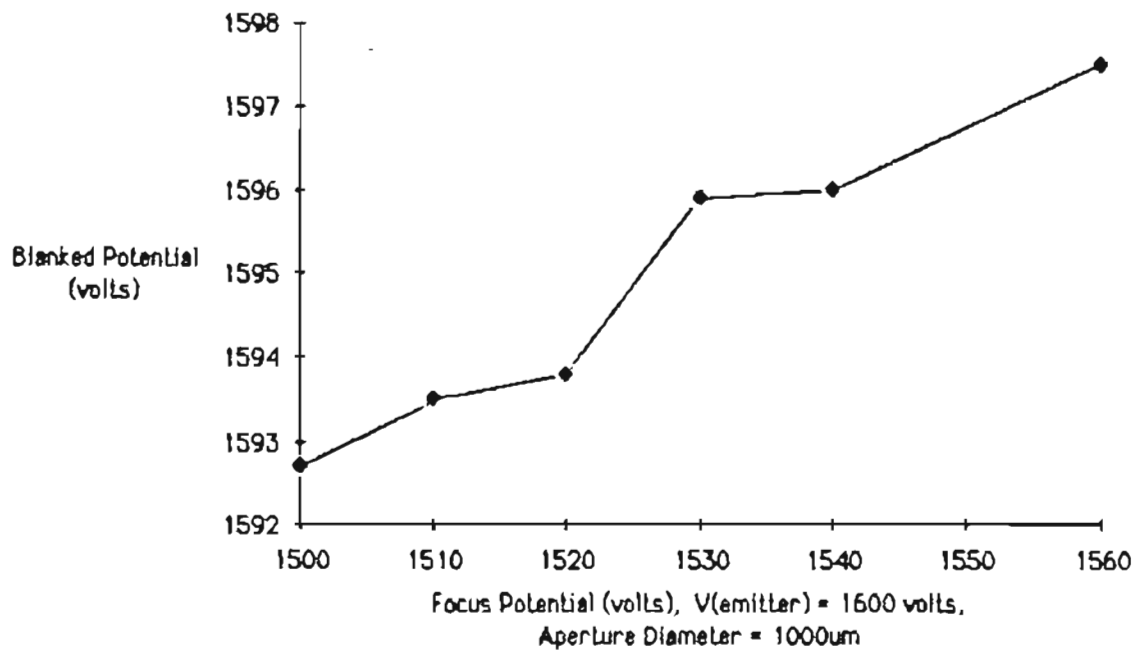


Figure 4-14. Blanked Voltage versus Focus Voltage

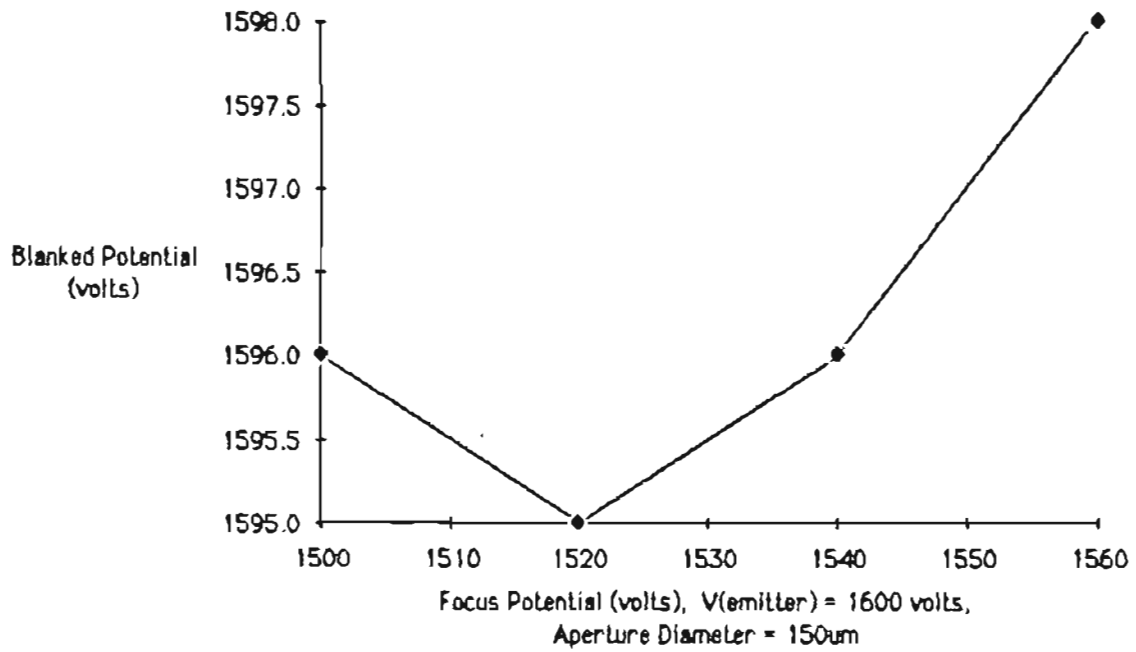


Figure 4-15. Maximum Current versus Focus Voltage

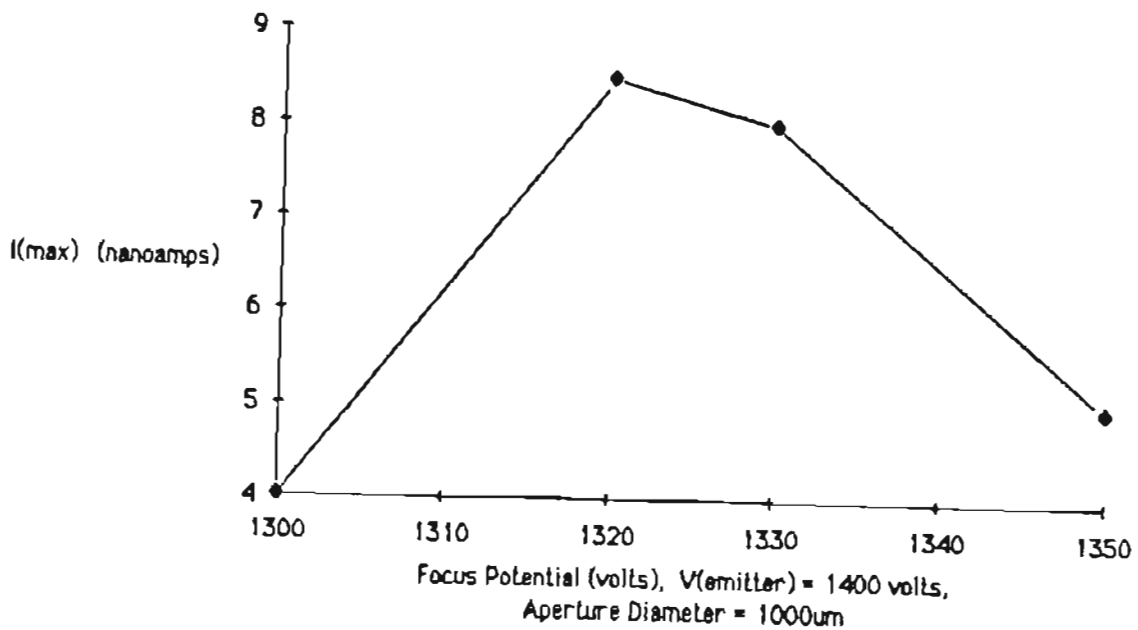


Figure 4-16. Maximum Current versus Focus Voltage

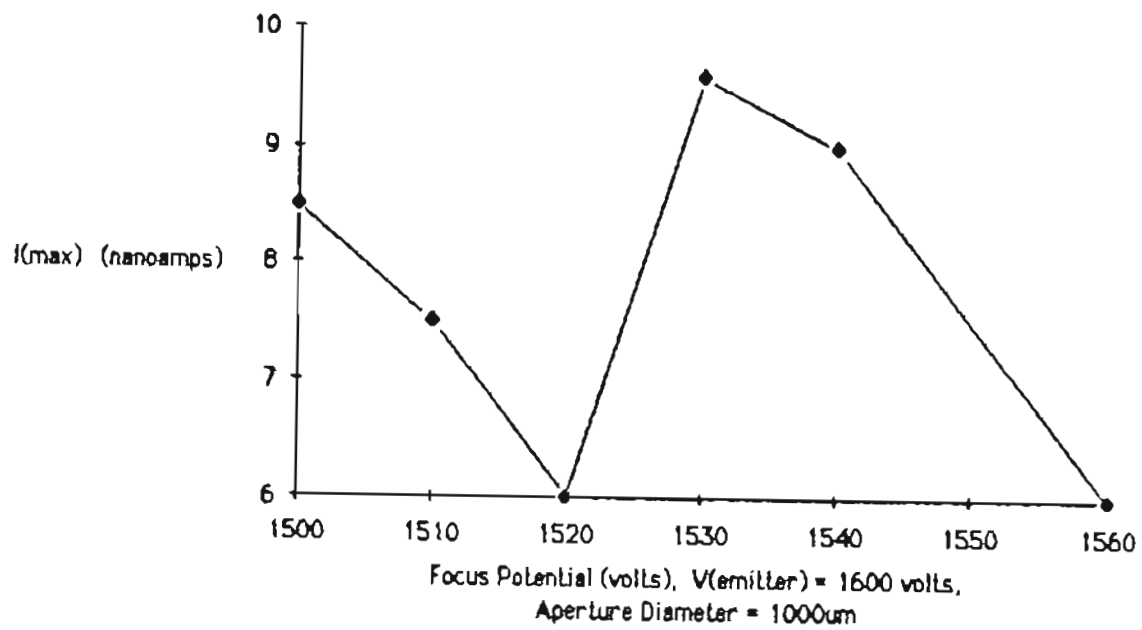


Figure 4-17. Maximum Current versus Focus Voltage

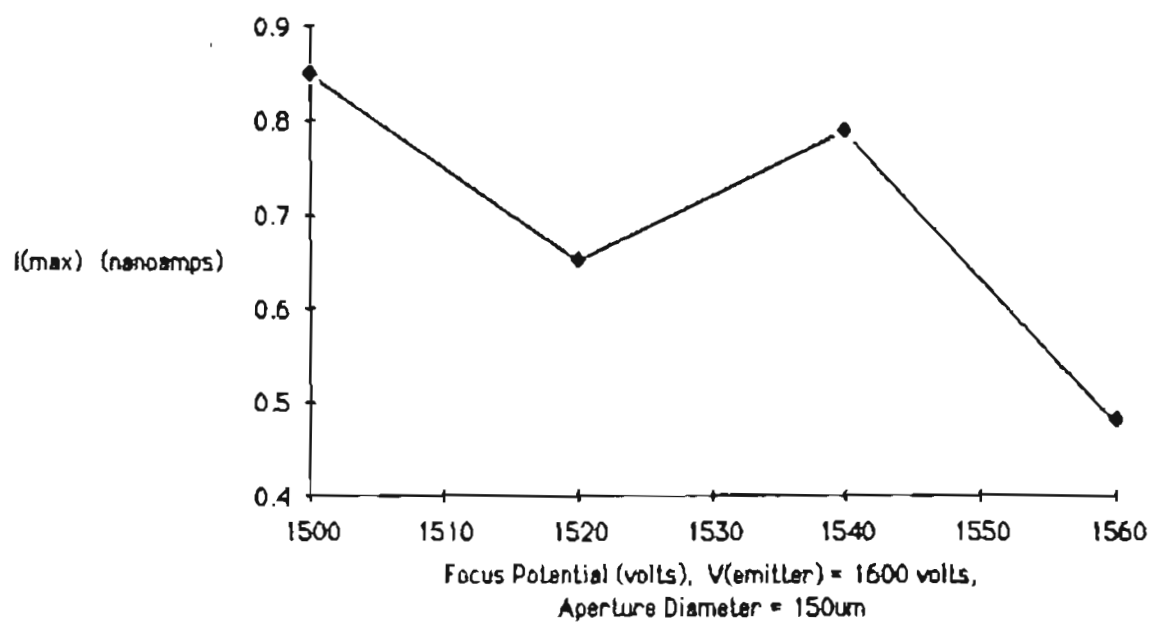


Table 4-4. Shadow Measurement Data

Photo	N	E 1 (mil)	E 2 (mil)	E 3 (mil)	E 4 (mil)	E 5 (mil)	E 6 (mil)	E 7 (mil)	E 8 (mil)	E 9 (mil)
111	0.93	74	23	25	92	62	23	25	58	91
151	0.94	44	13	15	58	61	24	25	59	
161	1.16	57	18	20	73		36	39	84	
171	0.99	78	23	26	100	84	35	32	74	

Grid Radii	e1 (mil)	e2 (mil)	e3 (mil)	e4 (mil)	e5 (mil)	e6 (mil)	e7 (mil)	e8 (mil)	e9 (mil)
	13.3	3.8	4.2	16.2	12.8	4.8	5.2	11.2	19.7

Photo	M1	M2	M3	M4	M5	M6	M7	M8	M9
111	5.6	6.1	6.0	5.7	4.8	4.8	4.8	5.2	4.6
151	3.3	3.4	3.6	3.6	4.8	5.0	4.8	5.3	
161	4.3	4.7	4.8	4.5		7.5	7.5	7.5	
171	5.9	6.1	6.2	6.2	6.6	7.3	6.2	6.6	

Explanation of Terms: N = enlargement normalization factor; in addition to this term, the measurements of each photo are divided by 16 to account for photographic magnification  
E(i) = the normalized shadow measurements  
e(i) = the grid separations  
M(i) = E(i)/e(i)

Table 4-5. Summary of Spherical Aberration Results

Result	111	151	161	171
$M_o$	6.05	4.75	4.75	6.10
$M'_o$	4.92	5.17	7.49	6.71
$c_o$ (in.)	0.603	0.567	0.364	0.413
$z'_o$ (in.)	0.201	0.237	0.440	0.319
$m_o$	0.619	0.779	0.725	0.574
$1/m_o$	1.62	1.28	1.38	1.74
$1/m_o - m_o$	0.996	0.501	0.655	1.17
$z - z'_o$ (in.)	1.61	1.58	1.38	1.42
$f_o$ (in.)	1.62	3.15	2.11	1.21
$g_o$ (in.)	-0.802	-2.25	-1.09	-0.304
$\beta$ (mil <sup>2</sup> )	$-2.88 \times 10^{-4}$	$-1.44 \times 10^{-4}$	$-2.97 \times 10^{-4}$	$-2.66 \times 10^{-4}$
$\beta'$ (mil <sup>2</sup> )	$2.56 \times 10^{-4}$	$2.20 \times 10^{-3}$	0.0	$1.75 \times 10^{-4}$
$C_1$ (mil <sup>2</sup> )	$-3.40 \times 10^{-4}$	$-1.87 \times 10^{-4}$	$-2.97 \times 10^{-4}$	$-2.92 \times 10^{-4}$
$C_2$ (mil <sup>2</sup> )	$0.953 \times 10^{-4}$	$0.396 \times 10^{-4}$	0.0	$0.597 \times 10^{-4}$
$S_f$	74	82	106	44.2
$S_g$	-76.7	-102	-101	-49.1
$C_s(\infty)$ (in.)	31	80	53	13.4
$C_s(\infty)$ (mm)	789	2040	1353	339

Constants

$z = 1.815''$

$a = 0.792''$

$b = 0.804''$

$d = 2.365''$

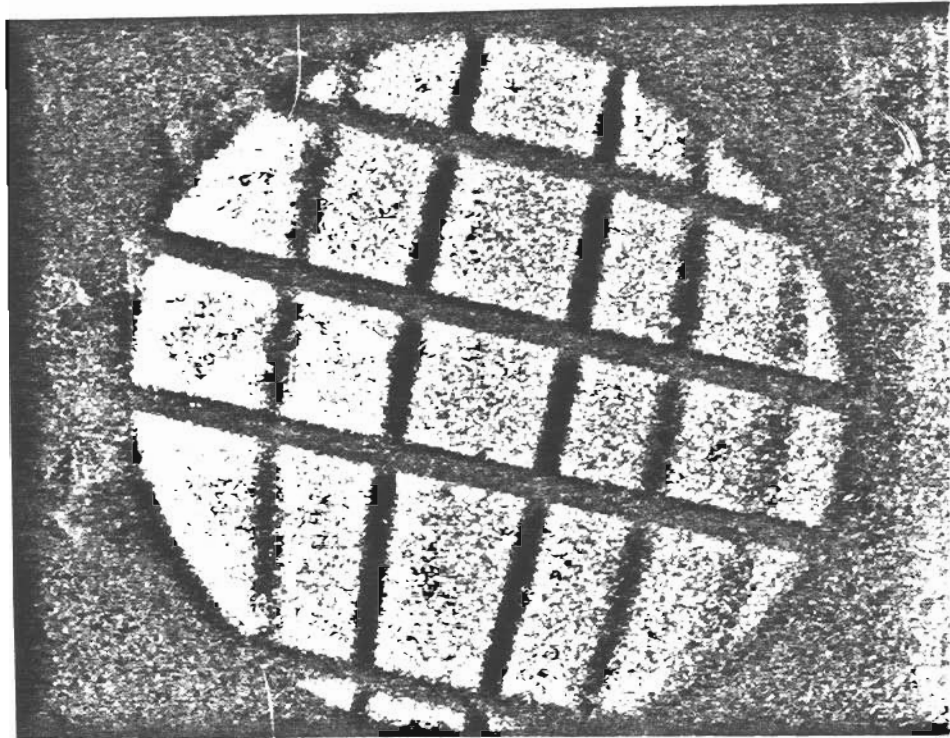


Photo 11I

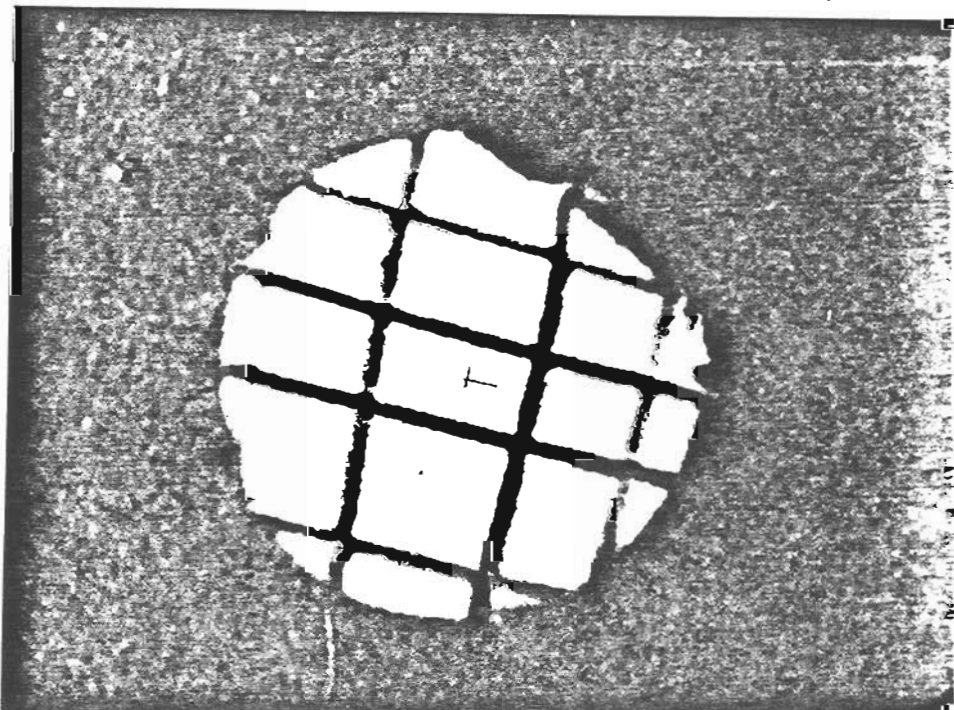


Photo 15I

Figure 4-18. Data Enlargements of Photographs 11I and 15I

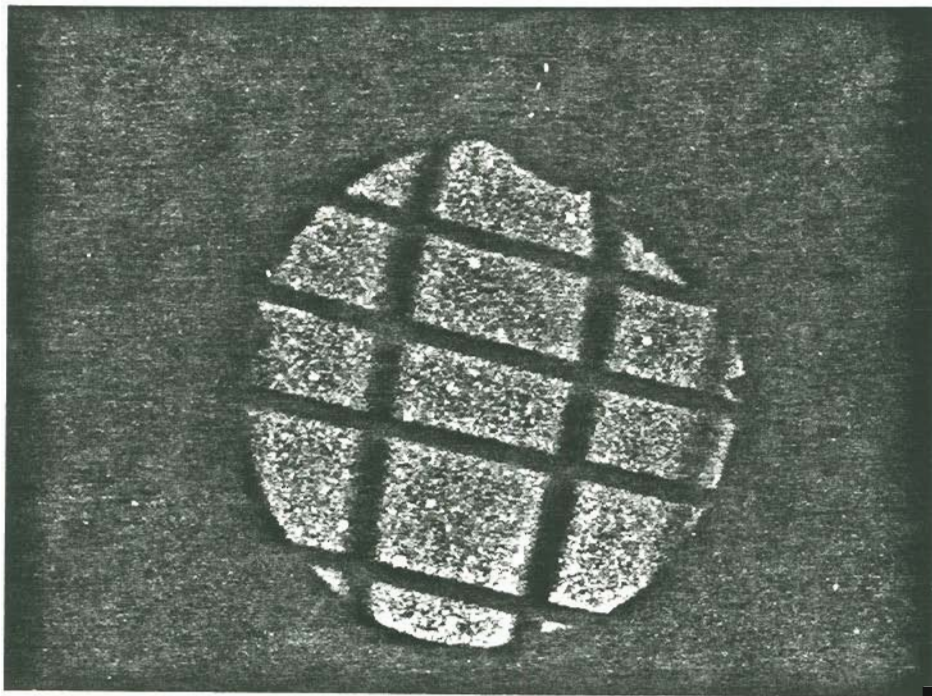


Photo 16I

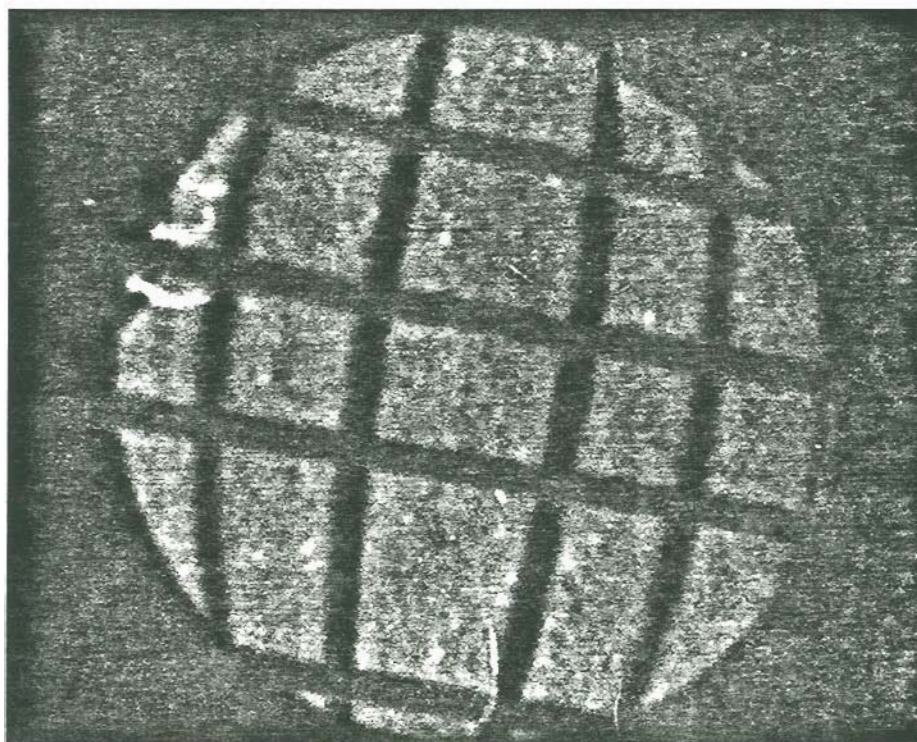


Photo 17I

Figure 4-19. Data Enlargements of Photographs 16I and 17I

## Chapter V

### Conclusions

The beam modulating lens was designed to give high frequency, low spherical aberration modulation of an electron beam. Preliminary computer calculations gave approximate results on these parameters, but needed to be clarified with experimental data.

The data on the beam cut-off properties of the lens were better documented and more conclusive than the  $C_s$  data. The results from these tests showed very conclusively that the present design of the modulator lens could block an electron beam with a voltage swing of no less than 8.5 volts ( $V_{\text{emitter}}=1400$  volts,  $V_{\text{focus}}=1300$  volts) in the  $1000\mu\text{m}$  aperture case, and commonly needed a swing of approximately 14 volts ( $V_{\text{emitter}}=1600$  volts,  $V_{\text{focus}}=1560$  volts) in the  $150\mu\text{m}$  aperture case. Since the limiting value of this parameter was 5 volts for acceptable operation, the present form of the modulator lens is not adequate for high speed operation, and it must therefore be redesigned.

Since the beam cut-off data so conclusively showed that the modulator lens was not adequate for its planned application, the inability to measure the spherical aberration with the lens operated near beam cut-off became a moot point. The  $C_s$  measurements were taken under those operating conditions which were the closest to the normal operating parameters while also lending themselves to our particular experimental technique. Therefore, while the spherical aberration results do not apply to

the modulation behavior of the lens, the determination of  $C_s$  did prove to be an interesting electron optical exercise.

Although the spherical aberration data could be much more detailed, it does enable one to estimate the object side spherical aberration for the infinite magnification case. For a beam potential of 2300 volts, the results were as low as 339 mm for  $V_{\text{focus}}=1450$  volts and  $V_{\text{central}}=1825$  volts, and as high as 2040 mm for  $V_{\text{focus}}=1750$  volts and  $V_{\text{central}}=1825$  volts. The lower result is the best of the four tabulated, and also had the smallest degree of scatter of the  $C_s$  value. This value for the spherical aberration is much lower than would be expected of a filter lens, although it was not obtained in the cut-off operating region.

Modifications to the beam modulator lens have been considered in light of the beam cut-off results. The expected modification would be to reduce the thickness the central electrode since this is the main element so far as the cut-off properties of the lens are concerned. Again, computer calculations would be used to optimize the modified configuration. Furthermore, modification to the experimental determination of  $C_s$  would entail placement of a 150 mesh SEM grid in front of the lens and removal of the rear grid altogether. Since points in front of the lens are the only ones suitable to  $C_s$  measurement, such an arrangement would produce 10 - 20 data points per photograph which should enable a much more accurate determination of  $C_s$ .

## Appendix A

### Electron Emission

Emission can occur through one of two general mechanisms. The first mechanism involves imparting adequate kinetic energy on a charged particle to drive it off of the emitting surface. Two examples of this type of emission are thermionic emission and photoemission. The second general mechanism for charged particle emission is to draw charged particles off of an emitting surface in the presence of powerful electric fields. This type of charged particle emission is called field emission. Of course, combinations of these mechanisms exist, for example in the form of thermionic field emitters. The discussion to follow however, will emphasize field and thermionic emission. Thermionic emission will be discussed to give a conceptual framework from which to understand field emission.

All materials maintain their chemical identity by keeping their constituent particles from leaking away. This is actually true, to some degree, of molecules down to the atomic level. For the sake of simplicity however, the discussion will be narrowed to solids, solid-vacuum interfaces, electrons, and electron emission.

A solid keeps its electrons because of a wall of potential energy between itself and the vacuum beyond. For an electron to escape in a classical way, the sum of its original potential energy and some amount of absorbed kinetic energy must be greater than the potential energy of the

wall. Two sources of this kinetic energy are heat and light, in which case the emission of electrons from a surface is called thermionic emission and photoemission, respectively.

These two types of emission are consistent with the classical notion of emission in that the particle must have more energy than the barrier in order to get over it. It must be emphasized that the barrier is energetic, not physical, and that it only makes sense in the context of an energy diagram. As an example, consider the energy diagram for thermionic emission in Figure A-1.

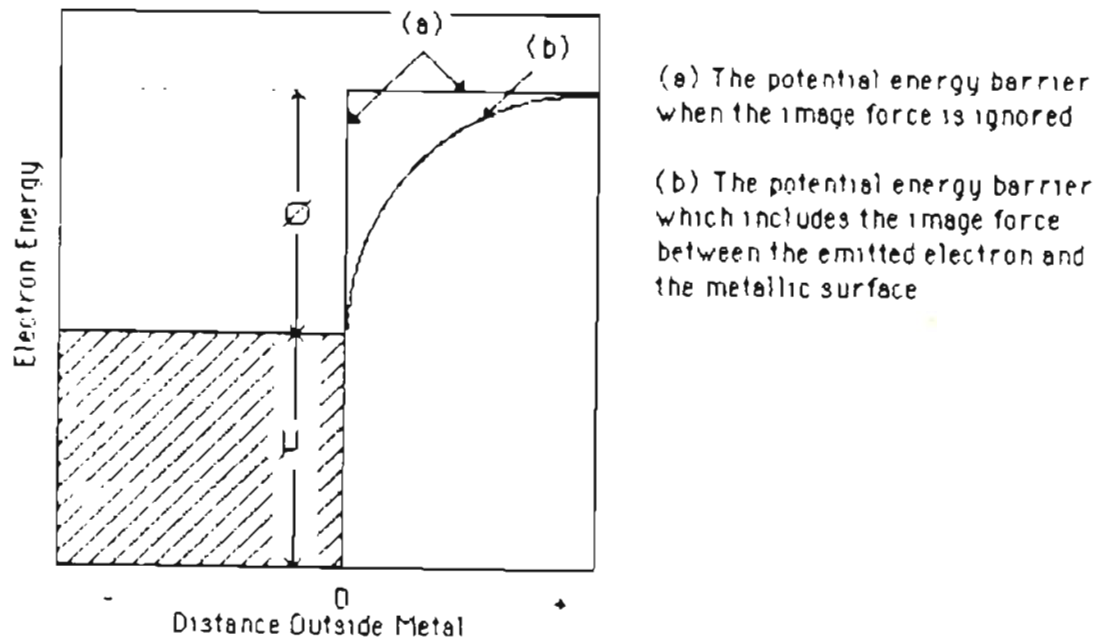


Figure A-1. Thermionic Emission

Field emission on the other hand violates this classical notion. In field emission the barrier is deformed by an applied electric field to such a degree that the electron can tunnel through the barrier in a quantum mechanical fashion. This behavior is in utter violation of the tenets of classical physics, and can only be understood from its quantum mechanical origins.

With the discussion limited to metals and metal surfaces, the free-electron model<sup>1,2</sup> of solids becomes applicable. Based on the Fermi-Dirac statistical distribution,

$$f(\epsilon) = \{e^{(\epsilon-\mu)/kT} + 1\}^{-1} \quad (\text{A-1})$$

this model considers the most weakly bound valence electrons to be free to roam about the volume of a solid without being locked to one particular atom or molecule. The above equation gives the probability that an orbital at energy  $\epsilon$  will be occupied in an ideal electron gas at thermal equilibrium. The value  $\mu$  is the temperature dependent chemical potential which, at  $T$  equal to absolute zero, is equal to the Fermi energy. The Fermi energy is also considered to be the energy of the topmost filled orbital at absolute zero. The constant  $k$  in the expression is the Boltzmann constant. The forces between these conduction electrons and the ion cores are neglected.

Under relaxed or equilibrium conditions the electrons within the molecules have energies corresponding to the atomic energy levels of the particular material. Within each level there may be up to two electrons (with opposite spin), this limit being the result of the Pauli Exclusion Principle<sup>3</sup>. Exact studies of the energy level structure of many materials have shown that these atomic energy levels tend to fall together in clusters on energy diagrams. These clusters, referred to as bands, have become the standard in discussions about electronic energy levels.

The common electrical materials each have an explanation of their electrical properties based on their band structure. This atomic or solid-state theory of electrical properties is consistent with the observation that the electrical properties of materials are one of the cyclic properties on

the periodic table. The common electrical materials are insulators, conductors, and semiconductors. Although conductors (metals) are the main concern of this discourse, a brief review of the band structure of the other materials will increase the understanding of the electrical properties of interest.

An insulator is characterized by the property that all the energy bands are completely filled by electrons. With no electron vacancies there is no way for electrons to move about, and therefore no way to carry current. Note however that electron vacancies do not refer to spatial voids, but rather to unoccupied energy levels which could potentially be filled by an electron.

Avoiding all the perturbations and varieties of semiconductors, the band structure of only intrinsic semiconductors will be described. Noting that there are gaps between the energy bands of all materials, it should be clear that such gaps are energy regions forbidden to the electrons. These forbidden gaps, as they are sometimes called, are a part of the band structure of every material. However, it occasionally happens that the gap between a completely empty band and a filled band is small. In such a case electrons can be excited (either thermally or optically) into the empty band where they are free to conduct. Materials with this property are called semiconductors.

A conductor characteristically has one or more bands which are only partially filled. As such, the electrons within those partially full bands can be accelerated by small fields to move charge, and hence to carry current.

When discussing the conductive properties of materials it is common and justifiable to consider only the top portion of the top band.

Intuitively this makes sense since all bands and levels below this area are filled, making them non-conductive. Therefore, the following discussions about metals (conductors) will only consider the top energy band.

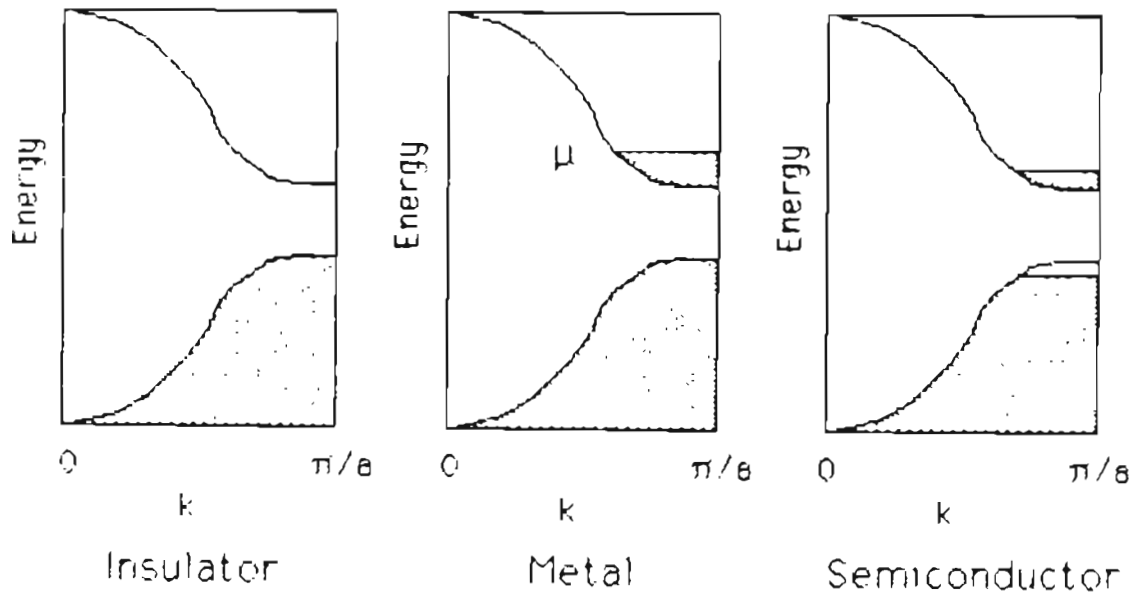


Figure A-2. Energy Diagrams of Insulators, Conductors, and Semiconductors. Shaded areas designate filled energy levels.

The highest filled energy level within the top band is called the Fermi level, and is denoted  $\mu$ . In metals it is always several volts above the bottom of the band.

A large part of the barrier keeping the electrons within a molecule is called the work function (denoted  $\phi$ ). The two previous diagrams give schematic views of the relationship between the Fermi level, and the work function. Since the work function for metals is between 2-5 volts, it is clear that thermionic emission and photoemission require electrons to absorb at least 2-5 volts to be emitted. For thermionic emission this requires that

temperatures up to 1500°K be attained, while the threshold for photoemission lies in the visible or near ultraviolet regions.

To examine the theoretical details behind one-dimensional thermionic emission, consider an electron outside a metal. Using the electrodynamical technique of image potentials, it can be shown that the electron sees an image potential  $V = -e^2/4x$ , where  $x$  denotes the distance between the electron and the surface of the metal. This results in a force on the electron  $F = -dV/dx = -e^2/(2x)^2$ . With the metal surface at  $x=0$ , the energy diagram across the surface takes on the form in figure A-1(b).

The potential energies at the top of the diagram are given by

$$V = -W \quad x \leq 0 \quad (\text{A-2})$$

$$V = -e^2/(4x + e^2/w) \quad x > 0 \quad (\text{A-3})$$

noting that all molecular potentials are referenced below zero, and that the  $e^2/w$  term is a factor to satisfy the boundary condition at  $x = 0$ . It is clear from equation (A-3) that  $V \rightarrow 0$  in the limit as  $x \rightarrow \infty$ , implying that the potential barrier between the metal surface and vacuum is infinitely wide due to the image potential. Therefore thermal excitation alone will not be able to induce electron emission, some electric field is needed to deform the potential barrier so that its width becomes finite.

Taking the simplest case of a constant electric field,  $F$ , the potential beyond the surface due to the field is given by  $V = -eFx$ . Equation (A-3) becomes

$$V = -e^2/(4x + e^2/w) - eFx \quad x > 0. \quad (\text{A-4})$$

This relation shows that in the limit as  $x \rightarrow \infty$ , that now  $V \rightarrow -\infty$ , implying that the barrier is in fact finite in width from the point of view of an electron at the Fermi level. If the field is of moderate strength, no appreciable tunneling will occur.

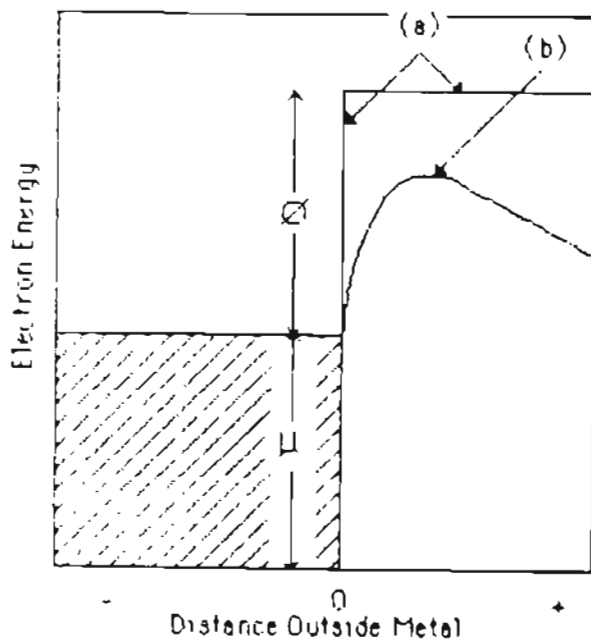
With such a simple algebraic relation, it is possible to calculate the location and maximum height of the potential barrier. A local extremum is given by the condition

$$dV/dx = 0 = 4e^2/(4x + e^2/w)^2 - eF \quad (\text{A-5})$$

which, since  $d^2V/dx^2 < 0$ , is the maximum value of  $V(x)$ . Solving for  $x$  gives  $x_{\text{max}} = (e/4F)^{1/2} - e^2/4w$ , which when inserted into equation (A-4) gives

$$V_{\text{max}} = (e^3F/4w) - (e^3F)^{1/2}. \quad (\text{A-6})$$

Using typical values for  $e$ ,  $F$ , and  $w$  it becomes apparent that the first term in the expression is less than 1% of the second. Therefore,  $V_{\text{max}}$  can be approximated by the second term, which is called the "Schottky barrier potential".



- (a) The potential energy barrier when the image force is ignored  
 (b) The modified form of the image force barrier when an external electric field is applied

Figure A-3. Surface Potential Barrier in Presence of Electric Field

As was stated earlier, the condition for electron emission is that the particle must have an energy greater than that of the potential barrier. Figure (A-3) shows that electrons within the metal see the height of the barrier as (using the approximated  $V_{\max}$ )  $B = w - (e^3 F)^{1/2}$ , where  $w = e\phi + \mu_0$ . From these relationships, and the Fermi-Dirac energy distribution of the electrons, the flux of the electrons can be approximated by

$$F \approx \frac{2kT}{h^3} \exp\left[-\frac{(e\phi - e^{3/2} F^{1/2})}{kT}\right] \times \iint \exp\left[-\frac{(p_y^2 + p_z^2)}{2mkT}\right] dp_y dp_z \quad (\text{A-7})$$

where the  $p_i$ 's are the momenta in the  $i$ -directions, and the integrals are over the range  $\pm\infty$ . This expression can be evaluated and, by multiplication with the electronic charge  $e$ , gives the current density for a thermionic emitter in ( $\text{A}/\text{cm}^2$ ) to be

$$J_0 = 4\pi em(kT)^2/h^3 \exp\left[-\frac{(e\phi - e^{3/2} F^{1/2})}{kT}\right]. \quad (\text{A-8})$$

The very strong temperature dependence of the thermionic current density is quite clear in the form of the  $T^2$ . Typical current densities for a tungsten thermionic emitter are on the order of 1 to 10  $\text{A}/\text{cm}^2$ .

Field emission is defined as the emission of charged particles from the surface of a condensed phase into another phase (usually vacuum) under the action of powerful electrostatic fields (0.3 - 0.6  $\text{V}/\text{\AA}$ ). Since the device used was made of tungsten, the discussion will be limited to the case of emission from solid metal surfaces into a vacuum. The discussion will invoke the tools of quantum mechanics to give a theoretical basis for the phenomenon. Unlike the fields used in thermionic emission, the electric fields in field emission are intended to deform the potential barrier so that tunneling does occur. Figure A-4 indicates the deformation

of the barrier in field emission.

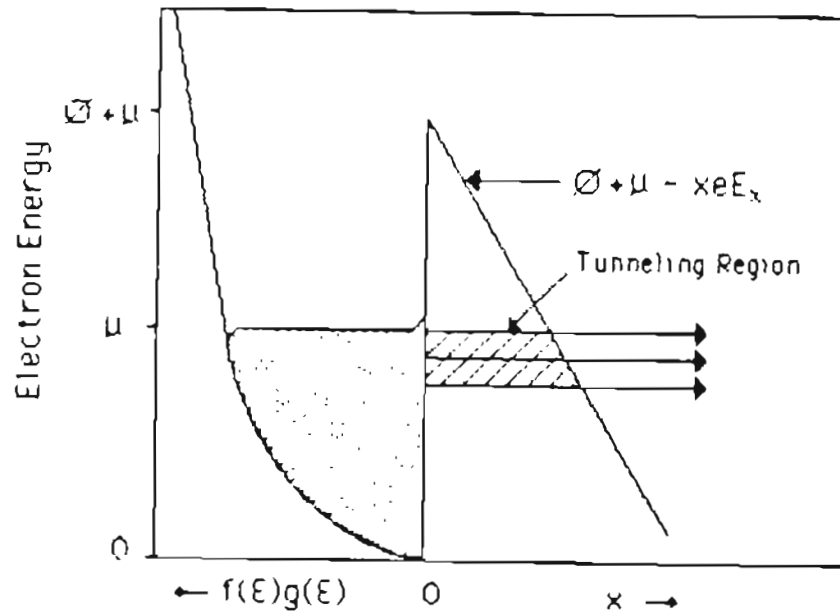


Figure A-4. Field Emission Energy Diagram

Under common operating conditions, the electron undergoing field emission has a tunneling distance of approximately 15Å.

The theory which describes the operation of field emitters was developed in 1928 by Fowler and Nordheim (reference 4). The result was the commonly used Fowler-Nordheim equation which relates the field emission current to the applied field and the work function of the emitting material. Fowler and Nordheim first reduced the problem to the one-dimensional case at 0°K, from which they calculated the transmission coefficient of electrons passing through the potential barrier (with an energy  $E_x$  normal to the surface) to be

$$D(E,V) = 4[E_x(\phi + \mu - E_x)]^{1/2} \div (\phi + \mu) \times \quad (A-9)$$

$$\exp\left\{-4/3\left(2m/H^2\right)^{1/2}(\phi + \mu - E_x)^{3/2}/Fe\right\}.$$

The calculation was done by treating quantum mechanical tunneling with the WKB method. Using Fermi-Dirac statistics, it is possible to determine the distribution of electrons with velocities along the emission direction  $x$  (within the range  $v_x$  and  $v_x + dv_x$ ) by integrating over the energies  $\epsilon$

$$N(v_x) = 4\pi m^2/h^3 \int_0^\infty [1 + \exp((E_x + \epsilon - \mu)/kT)]^{-1} d\epsilon. \quad (A-10)$$

The differentials of the kinetic energy and the velocity are related by  $dE_x = mv_x dv_x$ . It is therefore possible to integrate the product of  $D(E_x)$  and  $N(v_x)$  over the normal energies  $E_x$  to obtain the energy distribution normal to the surface,

$$I(E_x) = 16\pi m \Delta [E_x(\phi + \Delta)]^{1/2} \exp[-b(\phi + \Delta)^{3/2}/F] \div (\phi + \Delta)h^3.$$

(A-11)

This is the result in the range  $E_x < \mu$ , which corresponds to the pure field emission case. The factor  $b$  is a constant, and  $\Delta = \mu - E_x$ . The graphs below of  $I(E_x)$  versus  $E_x$  show how the distribution broadens and the maximum shifts as the field is increased. This results from lower energy electrons being emitted as the field is increased.

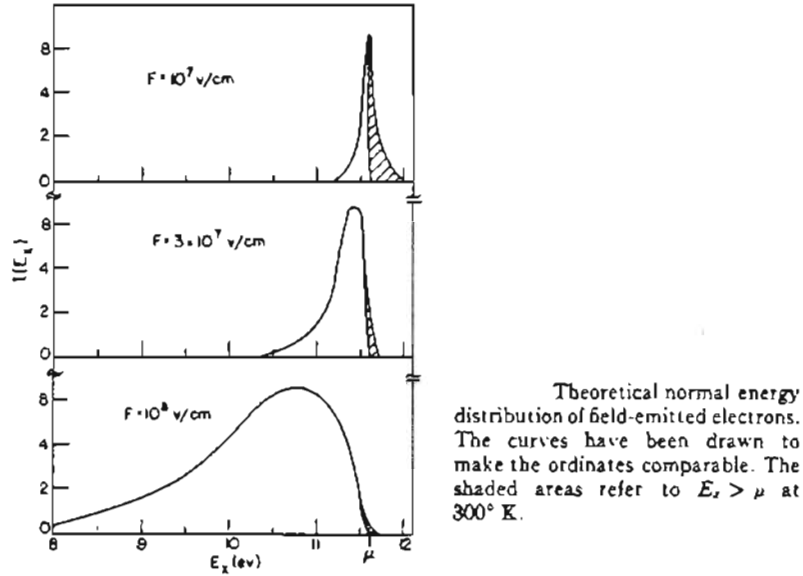


Figure A-5. Theoretical normal energy distribution of field emitted electrons<sup>5</sup>. The shaded areas refer to  $E_x > \mu$ .

The total current density is calculated by integrating<sup>6</sup> the normal energy distribution  $I(E_x)$  over  $E_x$

$$J = [16\pi me(\phi\mu)^{1/2} \exp(-b\phi^{3/2}/F) + h^3(\phi + \mu)] \times \int_{-\infty}^{\mu} \exp(3/2b\phi^{1/2}\Delta/F) \Delta dE_x. \quad (\text{A-12})$$

This integral is of the form  $\int ye^{cy} dy$ , and results in the equation

$$J = 64\pi me(\phi\mu)^{1/2} F^2 \exp(-b\phi^{3/2}/F) + 3h^3(\phi + \mu)b^2. \quad (\text{A-13})$$

Inserting the constants and evaluating the expression gives

$$J = 6.2 \times 10^6 \mu^{1/2} F^2 \exp(-6.8 \times 10^7 \phi^{3/2}/F) + \phi^{1/2}(\phi + \mu) \quad (\text{A-14})$$

which is the well-known Fowler-Nordheim equation for the current density of a cold (0°K) field emitter.

The Fowler-Nordheim equation relates the beam current versus the applied electric field in cases of high fields and low temperatures. A Fowler-Nordheim plot of  $\ln(J/F^2)$  versus  $1/F$  will have a slope proportional to  $\phi^{3/2}$ . Such a graph of experimental data allows the determination of the work function  $\phi$  when the relationship between  $I$  and  $J$ , and  $V$  and  $F$ , are known. Under typical operating conditions, the current densities of a field emitter are within the range 100 to 10,000 A/cm<sup>2</sup>.

References

1. J.S. Blakemore, Solid State Physics (W.B. Saunders Co., Philadelphia, 1974) p. 170
2. Charles Kittel, Introduction to Solid State Physics, (John Wiley & Sons, New York, 1976) p. 200
3. Eugen Merzbacher, Quantum Mechanics, (John Wiley and Sons, New York, 1961) p. 426
4. R.H. Fowler and L. Nordheim, "Electron Emission in Intense Electric Fields", Proc. Roy. Soc., A119, 173, 1928
5. Robert Gomer, Field Emission and Field Ionization, (Harvard University Press, Cambridge, 1961) p.14
6. Ibid., p.19

## Appendix B

### Vacuum Technology

The vacuum requirements for these experiments were determined by the use of a cold field emitter. Such emitters have a practical operating pressure threshold of approximately  $5 \times 10^{-9}$  torr. This value is due to the rule of thumb assumption that a surface will adsorb one monolayer per second at  $10^{-6}$  torr. At  $5 \times 10^{-9}$  torr pressure, 300 - 1000 seconds (about 5 - 15 minutes) are available to run an experiment before the emitter needs to be cleaned. Higher pressures give such a short amount of time between cleanings as to be virtually useless.

The vacuum system used was a standard stainless steel ultrahigh vacuum system capable of attaining pressures down to  $10^{-11}$  torr or lower. Without optimizing the pressure obtained, pressures were reached consistently in the low  $10^{-9}$  and occasionally in the high  $10^{-10}$  torr range.

Although such pressures are commonly used in experimental physics, a novice facing his first vacuum chamber has little hope of reaching such pressures. Since a large portion of time on this project was spent learning about vacuum techniques, it seemed logical to write-out this information for those beginners to follow. Therefore, the topics to be covered will be the methods and importance of cleaning and baking, the mechanisms and operation of thermocouple and ionization gauges, and the uses and operation of mechanical, sorption, sublimation, and ion pumps.

The main concern with the cleaning of surfaces to be used in high vacuum applications is to remove materials which have high vapor pressures, and which are difficult to pump. Such materials under vacuum conditions are able to vaporize or outgas at rates which may be equal to the available pumping speed, and as such would limit the attainable pressure so long as the substance is in the chamber. In the system that was used for these experiments, the main high vacuum pump was an ion pump. Such pumps for example are rather inefficient at pumping hydrocarbon materials, so it is very important that these materials in particular never enter the system.

The cleaning process used mainly entails degreasing each component. The degreasing process begins with thorough rinses with acetone to dissolve any hydrocarbons. Subsequent rinses use methanol to remove any remaining acetone and contaminants, and then water to remove the remaining residue. Drying the device should NOT be done with in-house compressed air. Such lines are usually driven by oil-sealed mechanical pumps, and as such could recontaminate a freshly cleaned surface with pump oil. The drying should be done with a dust-free disposable towel, or heating. It should be noted that this process may not necessarily be the best one to follow<sup>1</sup>, but it has proven to be acceptable and is sufficiently effective to warrant its use. The cleaning process and any subsequent handling of the device should be done while wearing clean gloves. A single fingerprint can leave enough of a residue to cause a non-trivial outgassing problem. Care should also be taken to keep the device dust-free between the time of cleaning and placement into the system. Dusting with a zero residue aerosol blower before placement into the system will fulfill this requirement.

If cleaning is done to reduce the surface causes of outgassing, baking is done to reduce both surface and subsurface causes of outgassing. Although a part may be baked before placing it into the vacuum system<sup>2,3</sup>, such precautions are only rarely necessary. On the other hand, each time the chamber is opened its interior walls are contaminated with atmospheric gases. Some of these gases desorb slowly, and would thus be pumped slowly. To speed the pumping, these surface gases are driven off the walls by baking the chamber.

Since the vast majority of surface area within our vacuum system was stainless steel, the discussion will be limited to the outgassing properties of this material. By far the most plentiful gas to outgas from stainless steel is water, which is followed by H<sub>2</sub>, CO<sub>2</sub>, CO, and Ar<sup>1,2</sup>. For all outgassing phenomena it has been found that the rate of outgassing is proportional to the temperature of the system (the baking temperature), and the duration of the bake. This relation has been found to be<sup>4,5</sup>

$$m = kt^2 \exp(B - A/T) \quad (B-1)$$

where  $m$  is the amount of gas evolved,  $t$  is the time,  $T$  is the absolute

Table B-1

The Theoretical Time to Reach an Outgassing  
Rate of  $10^{-13}$  W/m<sup>2</sup> in Stainless Steel<sup>1</sup>

$t$ (s)	$T$ (°C)
$10^6$ (11 days)	300
$8.6 \times 10^4$ (24 hours)	420
$1.1 \times 10^4$ (3 hours)	570
$3.6 \times 10^3$ (1 hour)	635

temperature, and  $k$ ,  $A$ , and  $B$  are constants. From this relation it is clear

that rapid outgassing is much more dependent on temperature than time (see table B-1). The preferred method for baking a system is to place an oven over it which is capable of temperatures in the 600 °C range. When this is not possible (due to either lack of availability of an oven or the inclusion of non-bakeable components) one may use either heating bands or, as a last resort heat tapes. Care should also be taken to heat (with a heat gun) any glass surfaces (such as windows or ionization gauge tubes) and any high surface area metal baffles which cannot be baked with the above methods.

The two pressure gauges used were chosen for their compatibility and their simplicity. The thermocouple gauge has an effective range between 760 torr - 1 mtorr, while the ionization gauge is effective in the range  $10^{-3}$ - $10^{-12}$  torr. With these gauges the operator has the capability to measure vacuum pressure over all ranges of interest. It should be noted however, that the accuracy of these gauges is generally no better than about  $\pm 10\%$ , but that this is an acceptable range of accuracy in most instances.

The thermocouple gauge is usually connected to the roughing manifold of the system because it is during this phase of the pumping that the pressure is within its range. The gauge does not measure the actual pressure, but rather the pressure dependent heat flow which is also dependent on the type of gas present (this is one source of the 10% error in the pressure reading). In principle a constant current is passed through the heater wire with a thermocouple, often copper - constantan, connected at the midpoint. As the pressure increases, heat flows to the walls of the thermocouple gauge, and the temperature of the heater wire decreases. The pressure is read from a d-c microammeter which is connected to the

thermocouple and calibrated in pressure units. A thermocouple gauge is extremely simple to use and is very useful in determining when to switch from rough pumping techniques to others.

Ionization gauge is actually a very loose term describing a class of quite distinct gauges whose unifying trait is their common principles of operation. The type of gauge to be described falls into the hot cathode category as a Bayard Alpert-gauge, which was designed by Bayard and Alpert in 1950<sup>6</sup>. Such a gauge, as with the thermocouple gauge above, does not measure the actual pressure. In this case the gauge measures the molecular density of a gas. The operation of the gauge is based on the ionization of gas molecules by collisions with electrons, and the subsequent collection of these ions. The collected ion current is proportional to the particle density which is proportional to the pressure.

The Bayard-Alpert gauge is run by an ionization gauge tube controller which maintains the necessary potentials and takes the necessary measurements to obtain a pressure reading. The pressure is calculated as

$$P = i_p / (S i_e) \quad (\text{B-2})$$

where  $i_p$  and  $i_e$  are the plate and emission currents, and  $S'$  is the sensitivity of the gauge tube. Each controller is calibrated for nitrogen, so the tubes sensitivity for other gases will vary depending on the ionization potentials of the other gases (see table B-2). However, there was not a great need for such accuracy in our experimental arrangement. In fact, from the table it is clear that the main atmospheric components ( $\text{N}_2$ ,  $\text{O}_2$ , and  $\text{H}_2\text{O}$ ) are within about 10% of the standard sensitivity, so that when pumping from atmosphere one would still be near the 10% error range that

is expected.

Table B-2  
Approximate Relative Sensitivity of  
Bayard-Alpert Gauge Tubes to  
Different Gases<sup>6</sup>

Gas	Relative Sensitivity
H <sub>2</sub>	0.42 - 0.53
He	0.18
O <sub>2</sub>	0.8-0.9
H <sub>2</sub> O	0.9
Ne	0.25
N <sub>2</sub>	1.00
CO	1.05-1.1
Ar	1.2
Hg	3.5
Acetone	5

The ion gauge used had a mechanism for degassing in which it was directly heated. The grid wire is heated by connecting it to a low-voltage, high-current source. The tube should receive an initial heating of at least 20 minutes to degas the glass tubing. After that, an occasional heating for about 15 seconds will be needed to clean the electrodes.

Like the pressure gauges described above, the four pumps used to run this vacuum system are also matched to complement each other's abilities. Check the table to obtain the basic operating parameters of each pump. Following will be brief outlines of some practical considerations for the use of each.

Table B-3

Basic Notes on the Operation of Four Vacuum Pumps			
pump	pressure range (torr)	pumping mechanism	saturation limited?
carbon vaned rotary pump	760 - 200	mechanical gas-transfer	no
cryosorption pump	$760 \cdot 10^{-3}$	gas capture	yes
titanium sublimation pump	$< 10^{-3}$	gas capture	yes
getter-ion pump	$< 5 \times 10^{-4}$	gas capture and ion pumping	yes

The first pump used differs from the most common mechanical pumps in that the rotary vanes seal with solid carbon vanes rather than with the more common oil. As such, this pump runs louder and hotter than the oil sealed pump, but there is much less of a chance of oil backstreaming into the system. Since the main ion pump is rather ineffective with hydrocarbons, the carbon vaned pump poses less of a risk of contamination. Although the cryosorption pumps are capable of pumping from atmospheric pressures, initial roughing with the mechanical pump helps to reduce the frequency at which the sorption pumps become

saturated.

The cryosorption, or more commonly sorption pumps, use an adsorbent cooled to liquid nitrogen (77°K) temperatures to pump gas molecules from the system. At this temperature most gases other than neon, hydrogen, and helium will be pumped until the molecular sieve saturates. If cooled to 15°K all gases would be pumped until saturation, with the partial pressure of hydrogen being about  $5 \times 10^{-8}$  torr<sup>7</sup>. The high surface area adsorbent (surface area of up to 600 square meters per gram) is also an attractive roughing pump because there is no possibility of hydrocarbons backstreaming into the system with this type of pump. The performance of these pumps can be, and in fact was, enhanced with the practice of staged roughing. This method entails using one sorption pump to go from the shut-off of the mechanical pump down to about 100 mtorr. That pump is then valved off and another is opened to pump from there down to  $5 \times 10^{-4}$  torr (the easy starting point for the ion pump). In using staged roughing it is important that the second sorption pump be sufficiently precooled before it is opened.

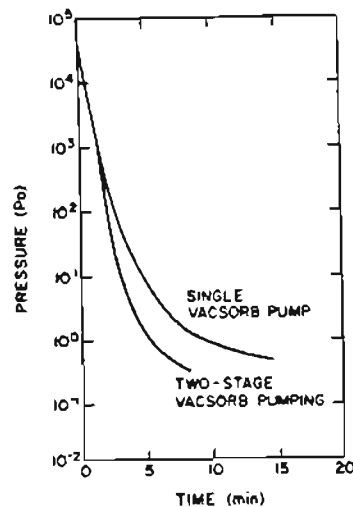


Figure B-1. Pumping Times for Systems of One or Two Sorption Pumps

Since water vapor seriously affects the performance of these pumps, it occasionally becomes necessary to bake the pump to drive off trapped water vapor. A bake of 5 hours with another pump drawing the vapor is usually sufficient. However, be certain to not use an oil sealed mechanical pump in this process due to the likelihood of contaminating the molecular sieve with pump oil.

If the sorption pumps are having a difficult time getting the pressure down to  $5 \times 10^{-4}$  torr for the ion pump, flashing or heating the

Table B-4

Initial Sticking Coefficient and Quantity Sorbed  
for Various Gases on Titanium<sup>8</sup>

Gas	Initial Sticking Coefficient		Quantity Sorbed <sup>a</sup> ( $\times 10^{15}$ molecules/cm <sup>2</sup> )	
	(300°K)	(78°K)	(300°K)	(78°K)
H <sub>2</sub>	0.06	0.4	8-230 <sup>b</sup>	7-70
D <sub>2</sub>	0.1	0.2	6-11 <sup>b</sup>	-
H <sub>2</sub> O	0.5	-	30	-
CO	0.7	0.95	5-23	50-160
N <sub>2</sub>	0.3	0.7	0.3-12	3-60
O <sub>2</sub>	0.8	1.0	24	-
CO <sub>2</sub>	0.5	-	4-24	-
He	0	0		
Ar	0	0		
CH <sub>4</sub>	0	0.05		

<sup>a</sup> For fresh film thickness of  $10^{15}$  Ti atoms/cm<sup>2</sup>.

<sup>b</sup> The quantity of hydrogen and deuterium sorbed at saturation may exceed the number of Ti atoms/cm<sup>2</sup> in the fresh film through diffusion into the underlying films at 300°K.

titanium sublimation pumps usually provides the added pumping needed to reach the starting point. The pumping mechanism for these pumps is the chemical reaction of gases with the surface of the active metal. Since the mechanism depends on chemical reaction, the inert gases such as helium, neon, and argon will not be pumped by a titanium sublimation pump (see table B-4).

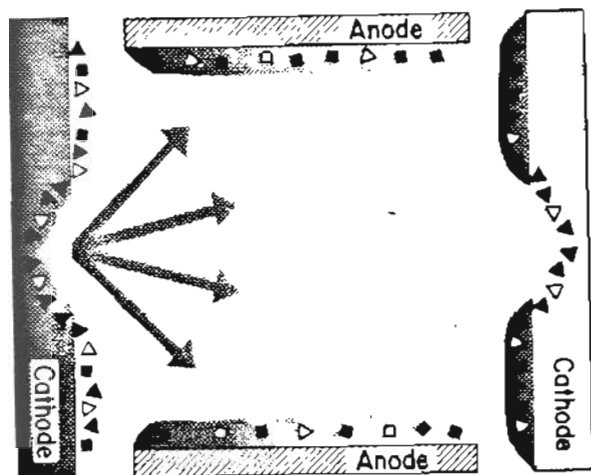
The active metal surface of the titanium sublimation pump is actually the entire chamber surface which is in the line of sight of the titanium filaments. Heating the titanium filaments with a current of 35-40A deposits a film of titanium on all of these surfaces. In some vacuum systems, the sublimators are located in a relatively narrow stretch of chamber. As such, heating them soon heats the surrounding chamber walls enough to cause more thermally induced outgassing than the pumps are pumping. Thus to use the titanium sublimation pumps to their maximum ability, it is in this instance necessary to water cool the chamber wall surrounding the filaments to prevent the heating of that surface.

The terminology surrounding ion pumps is confused and contradictory. References are made to sputter-ion, getter-ion, and simply ion pumps with contradictory definitions for each. To exemplify this situation, the ion pumps to be discussed are called sputter-ion pumps by P.A. Redhead, et. al. while the same pumps are called getter-ion pumps by O'Hanlon. Since the form and operation of this particular pump will be discussed, its type will be clear and it will be referred to simply as an ion pump.

The ion pump operates by a combination of two mechanisms. The first entails chemical reactions on active surfaces (as in the titanium sublimation pump above), the second entails ionization of gas molecules by

electron bombardment, followed by burial of the newly created ions in the pump wall. Most modern ion pumps are composed of modules which are made up of Penning<sup>9</sup> cells, external permanent magnets of about 0.1-0.2 Tesla strength, and cathode voltages of about 5kV at optimal operating conditions.

The electromagnetic fields in each Penning cell create a potential well which traps electrons between the two cathodes. The axial magnetic field sets the electrons into circular orbits which both prevent their reaching the anode, and which increase the probability that they will collide with and ionize a gas molecule



Schematic diagram showing sputter deposition and pumping in a Penning cell: ■ chemically active gases buried as neutral particles; ▲ chemically active gases ionized before burial; □ inert gases buried as neutral particles; △ inert gases ionized before burial.

Figure B-2. Schematic Diagram of a Penning Cell

As with the titanium sublimation pumps above, ion pumps tend to have different pumping rates for the various types of gases present. The active gases are in general easy to pump since they tend to form stable titanium compounds. The rates of pumping of the different gases can be obtained from the following table.

Table B-5

Pumping Speeds of Ion Pumps Relative to Nitrogen		
Gas	Diode pump	Triode pump
H <sub>2</sub>	2.7	2.1
CO <sub>2</sub>	1.0	1.0
H <sub>2</sub> O	1.0	1.0
O <sub>2</sub>	0.57	0.59
Light Hydrocarbons	0.9 - 1.6	0.9 - 1.0
He	0.1	0.3
Ne	0.04	
Ar	0.01	0.3

The difference between the diode and triode ion pumps is best explained through the use of a diagram. The main difference between the two pumps is the presence of a titanium sputter cathode in the triode pump.

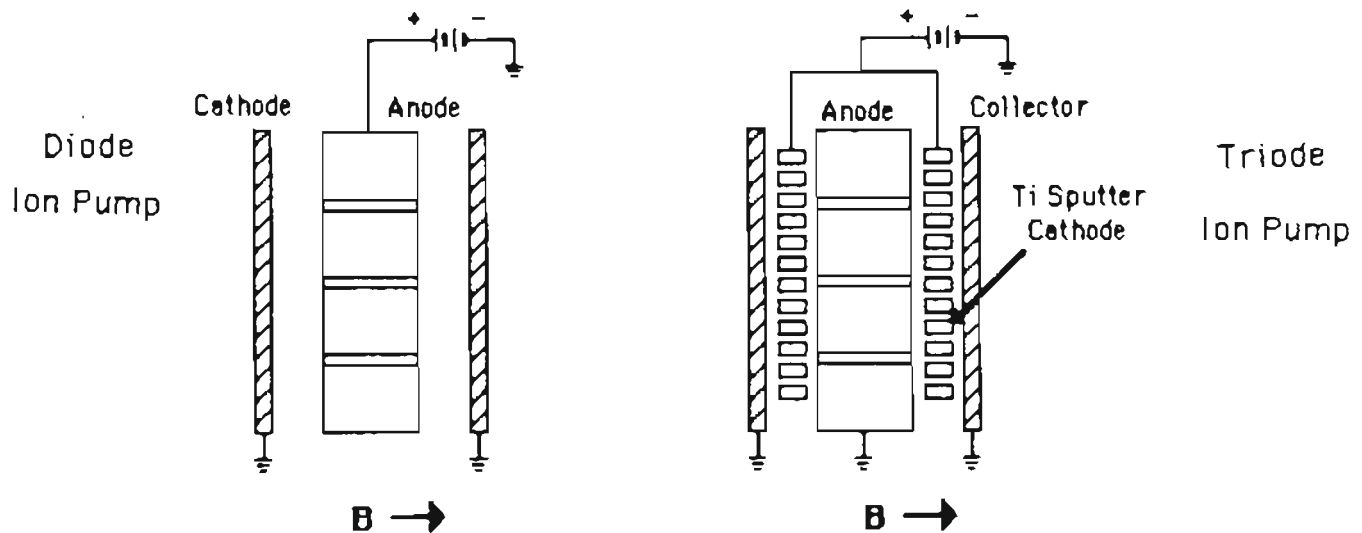


Figure B-3. Schematic Diagrams of Diode and Triode Ion Pumps

While the diode pump operates as was stated above, the triode pump has the honeycombed sputter cathodes placed between the anode and the

collector plates. Ions strike the sputter cathode at small angles sputtering titanium in the process. The sputtered titanium lands mostly on the collector where it binds with gas molecules. Although this type of pump is more complicated than the diode type, it is clear from the table above that the triode design is much more effective with noble gases. Hence the experimenter has the opportunity to tailor his ion pump mechanism to the type of gases to be pumped.

The operation of ion pumps is nearly fool-proof. The time when most caution is needed is when the pump first is being started. Since the operating current of the ion pump is directly proportional to the pressure, the relatively high pressure when the pump is turned on means that there is a relatively high current being drawn through the pump power supply. It is sometimes necessary under these conditions to disable the high current protection mechanism in the pump control unit in order to get the pump started. This should be done with a great deal of attention to the pump current. With the high current mechanism by-passed, it is possible to seriously damage the pump control unit with extended high current operation.

### References

1. John F. O'Hanlon, A User's Guide to Vacuum Technology, (John Wiley & Sons, New York, 1980) p.138
2. Ibid., p.141
3. P.A. Redhead, J.P. Hobson, E.V. Kornelson, The Physical Basis of Ultrahigh Vacuum, (Chapman and Hall Ltd., London, 1968) p.372
4. Ibid., p.374
5. Saul Dushman and J.M. Lafferty, Scientific Foundations of Vacuum Technique, (John Wiley & Sons, New York, 1962) p.586
6. O'Hanlon, p.63
7. Bill Brunner, "Basic Vacuum Technology", Unpublished Course Notes, Brunner's Vacuum Training, Livermore, California, 1984 p.41
8. O'Hanlon, p.211
9. Ibid., p.216
10. Redhead, et. al., p.407

Bibliography

J.S. Blakemore, Solid State Physics, (W.B. Saunders Co., Philadelphia, 1974)

Max Born and Emil Wolf, Principles of Optics, (Pergamon Press, New York, 1959)

Bill Brunner, "Basic Vacuum Technology", Unpublished Course Notes, Brunner's Vacuum Training, Livermore, California, 1984

Saul Dushman and J.M. Lafferty, Scientific Foundations of Vacuum Technique, (John Wiley & Sons, New York, 1962)

A.B. El-Kareh and J.C.J. El-Kareh, Electron Beams, Lenses, and Optics, (Academic Press, New York, 1970)

H. Goldstein, Classical Mechanics, (Addison-Wesley Press, Inc., Reading, Massachusetts, 1950)

Robert Gomer, Field Emission and Field Ionization, (Harvard University Press, Cambridge, 1961)

P. Grivet, Electron Optics, (Pergamon Press, New York, 1972)

P.W. Hawkes, Electron Optics and Electron Microscopy, (Taylor and Francis Ltd., London, 1972)

J.D. Jackson, Classical Electrodynamics, (John Wiley & Sons, New York, 1975)

F.A. Jenkins and H.E. White, Fundamentals of Optics, (McGray-Hill, 1957)

Charles Kittel, Introduction to Solid State Physics, (John Wiley & Sons, New York, 1976)

O. Klemperer, Electron Physics, (Butterworths, London, 1972)

O. Klemperer and M.E. Barnett, Electron Optics, (Cambridge

University Press, Cambridge, 1971)

Eugen Merzbacher, Quantum Mechanics, (John Wiley & Sons, New York, 1961)

Jon H. Orloff, "A Scanning Ion Microscope with a Field Ionization Source", Ph.D. Dissertation, Oregon Graduate Center, Beaverton, 1976

Jon H. Orloff, "Electron Optics", Unpublished Course Notes, Oregon Graduate Center, Beaverton, 1984

Robert M. Pirsig, Zen and the Art of Motorcycle Maintenance, (William Morrow & Company, Inc., New York, 1974)

P.A. Redhead, J.P. Hobson, E.V. Kornelsen, The Physical Basis of Ultrahigh Vacuum, (Chapman and Hall Ltd, London, 1968)

Gertrude F. Rempfer, "Unipotential Electrostatic Lenses: Paraxial Properties and Aberrations of Focal Length and Focal Point", J. Appl. Phys., 57 (7) 2385 - 2401, 1985

J. Arol Simpson, "Design of Retarding Field Energy Analyzers", Rev. Sci. Instr., 32, 1283-1293, 1961

Karl Spangenberg and Lester M. Field, "Some Simplified Methods Of Determining the Optical Characteristics of Electron Lenses", Proc. I.R.E., March, 138-144, 1942

David W. Tuggle, "Application of a Thermal Field Emission Source for Scanning Auger Microscopy", M.S. Thesis, Oregon Graduate Center, Beaverton, 1981

### Vita

The author was born in Klamath Falls, Oregon on February 15, 1961, and was some time thereafter carted off to Concord, California (a suburb of San Francisco), for his childhood and concurrent public school education. On a whim, sometime during the sophomore year of his high school experience, he took and passed the California State High School Proficiency Examination, which is something akin to the GED. Later that same year his family moved to Fairfield, California, and he had the choice between being a junior at an unfamiliar high school or a freshman at an unfamiliar community college. He chose the latter. After two years at Solano Community College, and several credits short of a degree, the author transferred to Reed College. During his senior year at Reed, he decided to enter the Reed College/Oregon Graduate Center joint program. He is presently working on a Ph.D. thesis project without having literally graduated from anything since Loma Vista Intermediate School (8th grade). He expects the powers that be will soon rectify the situation.